DEVELOPMENT OF SPATIO-TEMPORAL WAVELET POST PROCESSING TECHNIQUES FOR APPLICATION TO THERMAL HYDRAULIC EXPERIMENTS AND NUMERICAL SIMULATIONS

A Dissertation

by

NATHANIEL O. SALPETER

Submitted to the Office of Graduate Studies of
Texas A&M University
in partial fulfillment of the requirements for the degree of

DOCTOR OF PHILOSOPHY

May 2012

Major Subject: Mechanical Engineering

Development of Spatio-Temporal Wavelet Post Processing Techniques for Application to Thermal Hydraulic Experiments and Numerical Simulations

DEVELOPMENT OF SPATIO-TEMPORAL WAVELET POST PROCESSING TECHNIQUES FOR APPLICATION TO THERMAL HYDRAULIC EXPERIMENTS AND NUMERICAL SIMULATIONS

A Dissertation

by

NATHANIEL O. SALPETER

Submitted to the Office of Graduate Studies of
Texas A&M University
in partial fulfillment of the requirements for the degree of

DOCTOR OF PHILOSOPHY

Approved by:

Chair of Committee,	Yassin A. Hassan
Committee Members,	Kalyan Annamalai
	William Marlow
	Victor Ugaz
Head of Department,	Jerry Caton

May 2012

Major Subject: Mechanical Engineering

ABSTRACT

Development of Spatio-Temporal Wavelet Post Processing Techniques for Application to Thermal Hydraulic Experiments and Numerical Simulations. (May 2012)

Nathaniel O. Salpeter, B.S., University of Florida;

M.S., Texas A&M University

Chair of Advisory Committee: Dr. Yassin A. Hassan

This work focuses on both high fidelity experimental and numerical thermal hydraulic studies and advanced frequency decomposition methods. The major contribution of this work is a proposed method for spatio-temporal decomposition of frequencies present in the flow. This method provides an instantaneous visualization of coherent frequency 'structures' in the flow. The significance of this technique from an engineering standpoint is the ease of implementation and the importance of such a tool for design engineers. To validate this method, synthetic verification data, experimental data sets, and numerical results are used. The first experimental work involves flow through the side entry orifice (SEO) of a boiling water reactor (BWR) using non-intrusive particle tracking velocimetry (PTV) techniques. The second experiment is of a simulated double ended guillotine break in the prismatic block gas cooled reactor. Numerical simulations of jet flow mixing in the lower plenum of a prismatic block high temperature gas cooled reactor is used as a final data set for verification purposes as well

as demonstration of the applicability of the method for an actual computational fluid dynamics validation case.

DEDICATION

To my family and friends, thank you.

ACKNOWLEDGEMENTS

I would like to acknowledge the help of Carlos Estrada-Perez for his support with experimental measurements, Luigi Capone for his insight into discretization techniques, Michael Eckart for his help with the side entry orifice experiment, Jessica Hartley for her help with the air ingress scenario experiment, and Noushin Amini for the experimental data provided for the jet injection studies. I would like to acknowledge my committee members for their input and direction. Finally, I would like to acknowledge Dr. Hassan for his support of my research as well as of my own professional development.

NOMENCLATURE

Δ	Length Scale (m)
ε	Rate of dissipation of turbulence kinetic energy (v^2/m^3)
η,	Time scale ratio of turbulence to the mean strain, or Kolmogorov scale
κ	von Karman constant
μ,	Viscosity (Pa·s)
μ_t	Sub-grid scale turbulent viscosity
ρ	Density (kg/m^3)
ρ_L	Light fluid density (kg/m^3)
ρ_H	Heavy fluid density (kg/m^3)
σ	Standard deviation
Y_M,	Dilatation dissipation
φ	Concentration
τ	Wavelet basis function translation variable
$\psi_{a,\tau}$	Wavelet basis function
ω,	Specific dissipation rate
a	Wavelet basis function scaling coefficient
C_f	Wavelet correlation coefficients
C_{fsum}	Sum of wavelet correlation coefficient
CF	Experimental conversion factor for pixels to mm

d	Distance to nearest wall
D	Diffusivity
f	Frequency (Hz)
Fr	Froude number
J	Flux
K	Kinetic energy
K_{seo}	Pressure loss coefficient
P	Pressure (psi)
R	Radius from principle point (mm)
Re	Reynolds number (based on SEO diameter or nozzle inlet diameter)
s	Signal
S, $\overline{S_{ij}}$	Strain rate tensor
S_{ij}^{d}	Deformation tensor
T	Temperature (C)
T_{ij}	Turbulent stress tensor strain rate tensor.
t	Time (s)
Δt	Time between laser pulses (s)
u,v,w	Velocity components (m/s)
u_p,v_p	Un-calibrated experimental velocity components (pixel/time-step)
u_c,v_c	Calibrated experimental velocity components (m/s)
u_H	Heavy fluid velocity (m/s)
u_L	Light fluid velocity (m/s)

V	Voltage (Section 10.1), or Cell volume (Section 10.3)
W	Rotation rate tensor
x_c,y_c	Calibrated experimental locations (m)
x_0,y_0	Coordinate location of principle point (mm)
x_p,y_p	Cartesian coordinates (pixels)
Xop, Yop	Principle point location (pixels)
Ycorrection	Correction factor for y coordinate location
z	Z-direction component (mm)
z_o	Initial z plane location (mm)

TABLE OF CONTENTS

Page

Page

LIST OF FIGURES

Page

Page

Page

Page

Page

Page

LIST OF TABLES

Page

1. INTRODUCTION

Capturing the complexities of fluid flow and turbulence dates back to Leonardo Da Vinci[1], when he attempted to capture in sketches the unsteady nature of water flowing past obstacles. Although much has changed in terms of measurement technology in the five centuries since, observation still remains one of the most valuable forms of measurement for understanding the nature of a complex flow. Countless forms of measurement techniques and methods of interpreting the data have been proposed. These methods vary from interpretation of one-dimensional signal analysis such as the Fast Fourier Transform (FFT)[2] which provides a time averaged decomposition of the frequencies present in the flow, to techniques such as the Karhunen-Loève theorem, also referred to as proper orthogonal decomposition (POD)[3], which allows the decomposition of a flow field into its different energy modes.

The present work investigates a similar method known as 1D continuous wavelet decomposition, which relies on a correlation function for describing how well a signal is characterized by a specified function that is variable in its period and continuously translatable in time. This 1D wavelet analysis method which may be attributed to the compound work over nearly 75 years[4, 5], is a well established method that provides a frequency decomposition of a signal that is instantaneous over the length of the signal. While this method is sound on its own, the amount of useful information that may be extracted from a single signal is still fairly limited. A new semblance approach successfully applied to geophysical data[6] utilizes two signals that each have a 1D

This dissertation follows the style of Journal of Fluids Engineering.

wavelet transforms performed on them, and then the two resulting decompositions are correlated versus one another. The result is an instantaneous depiction of whether individual frequencies present in the two signals are correlated, anti-correlated, or undergo a time lag. This type of analysis is particularly useful for cases where only a few point measurements are taken (e.g. pressure transducer, laser Doppler anemometry, and hot-wire anemometry measurements) and the relationship between the signals is sought. Typical cross correlation between two signals provides information only on the time lag between the signals, irrespective of the frequency; however, the semblance analysis of the 1D wavelet transform allows this type of information to be extracted at individual frequencies. This is particularly valuable when wave propagation speed is not uniform across the spectrum.

The limitation in the traditional wavelet approach is the lack of spatial information. The development to date of two and three-dimensional wavelet transforms have been for the purpose of digital image compression[7]; however, in this process the temporal component of the wavelet basis function is dropped in favor of the spatial components. The present work seeks to recover the temporal nature of the wavelet transform, while still maintaining the spatial components. The implementation of this novel approach to an otherwise established method is detailed and verified in the present work and then applied to both numerical and experimental data sets. The subsequent chapters each contain background information pertaining to the particular experiments or simulation, as well as the results and conclusions about the applicability of the proposed method.

2. DESCRIPTION OF WAVELET METHODS

2.1 1D Continuous Wavelet Transform

The 1-dimensional wavelet transform is a loose derivative of the Fourier transform[2] in which sine and cosine waves are superimposed on one another to define another function. The principle behind 1D wavelet decomposition is to similarly use a continuous basis function (eqn.1) that may be altered in both its period and translation in time. By continuously varying this basis function by these two parameters at a particular moment in time, it is possible to represent the signal as a function of the period, as well as how well the function matches the signal. This representation is obtained through a correlation function (eqn.2).

The basic form of the wavelet correlation coefficient matrix is given by equation 1, where s(t) is the 1D signal, and $\psi_{a,\tau}$ (t) is the wavelet basis function. The correlation coefficient $C_f(f, \tau)$ is a function of a scale modifier, a, which can be transformed into a frequency f, and τ, which translates the wavelet basis function along the signal and may be interpreted as the translation in time, t. It should be noted that there is a need for engineering judgment involved in the choice of the particular wavelet basis function in order to resolve different pieces of information. The plot of the correlation coefficient is shown in figure 1 with the translation term, τ, converted to time, t, and the scale factor, a, converted to frequency, f.

$$\psi_{a,\tau}(t) = \frac{1}{\sqrt{a}}\psi\left(\frac{t-\tau}{a}\right) \quad (1)$$

$$C_f(f,\tau) = \int_{\mathbb{R}} s(t)\overline{\psi_{a,\tau}(t)}dt \quad (2)$$

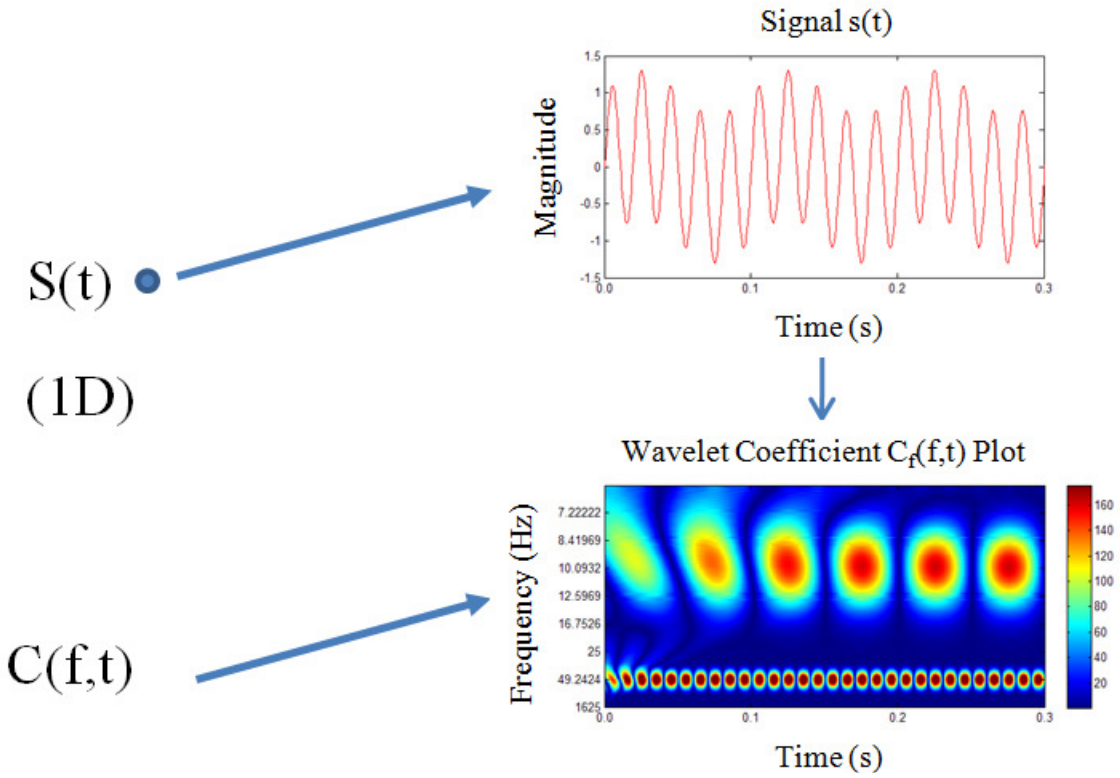

Figure 1 Plot of 1D Wavelet Correlation Coefficient, $C_f(f,\tau)$

2.2 1D Wavelet Semblance Method

The 1D wavelet semblance method[6] utilizes a cross correlation of the wavelet coefficient matrix of two separate signals. Each correlation coefficient matrix has a scalar value attributed to the level of correlation depending on the time and frequency. Multiplying one correlation coefficient matrix by the complex conjugate of the second correlation coefficient matrix, a matrix with both real and imaginary components is

obtained. This matrix may then be used to obtain the phase angle, Θ_p, by taking the arctangent of the ratio between the imaginary part and the real part for each position in the matrix. Lastly, the semblance plot is obtained by multiplying the absolute value of the cross-correlation matrix by the sign of $\cos(\Theta_p)$. The resulting semblance plot has the same scaling and axis as the original correlation coefficient contour plots, but the contour level now indicates whether the signals are correlated or anti-correlated by giving a value of 1 or -1.

In the verification case shown in figure 2, two signals described by equations 3 and 4 are decomposed with the 1D wavelet transform, and appropriately shown. The final plot in the series shows the semblance, or correlation between the signals.

$$S_1(t) = \cos\left(\frac{(t-125)}{40}\right) + \sin\left(\frac{t}{20}\right) \quad (3)$$

$$S_2(t) = \cos\left(\frac{t}{40}\right) + \sin\left(\frac{t}{20}\right) \quad (4)$$

While the frequency resolution is not great, simply by inspection of the semblance plot it becomes very clear that there is a low frequency present in the signals that have a phase shift that make the signals anti-correlated, and also a higher frequency signal in both that are very well correlated with one another. While this method appears to have some distinct advantages, it still lacks a spatial component. The ramification of this is that two signals may appear correlated or anti-correlated depending on the location of measurement. An example of this is if two pressure signals are obtained in a pipe where fluctuations in the flow travel with a given speed, the distance between the

transducers will effectively govern whether the signals are correlated or anti-correlated. While this seems quite obvious, it is worth noting in order to avoid misinterpretation of what the plot is indicating.

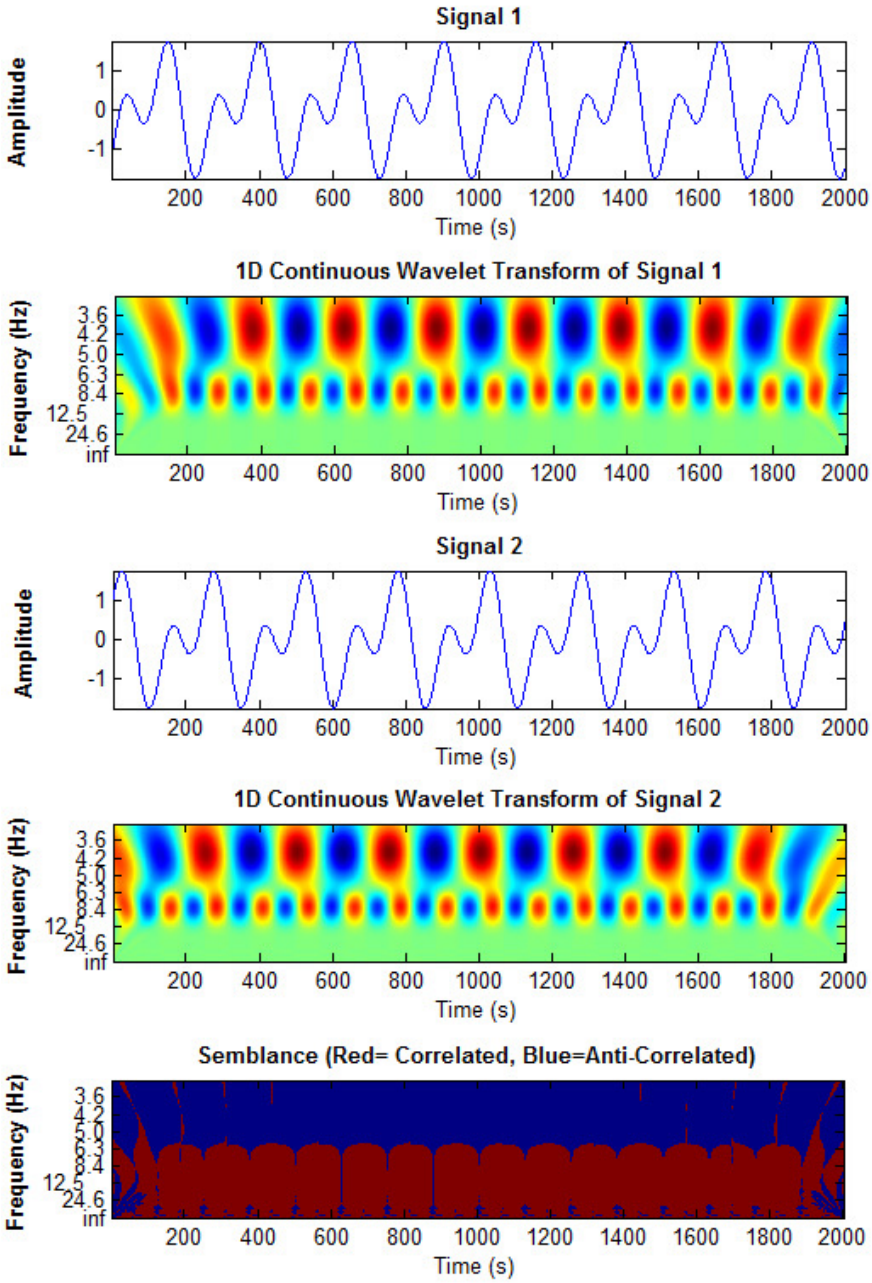

Figure 2 1D Wavelet Semblance plot of two signals containing correlated and anti-correlated components

2.3 Proposed 2D and 3D Spatio-Temporal Wavelet Method

While investigating the inherent problems that limit the semblance based analysis, it was determined that in order to more thoroughly understand how the signal is behaving and communicating between two points would be to track the signal through space and time. As previously mentioned, 2D and 3D wavelet approaches to date had been developed for the purpose of image compression in the spatial field alone, with temporal handling being a anti-aliasing type process that averages coefficients between time-steps, but does not actually perform a temporal decomposition. Drawing on the fact that each point in a field of time dependent data could be represented as a signal in time with a constant spatial coordinate, the idea to decompose each signal with the 1D wavelet transform and then reconstruct the spatial field of frequencies was developed.

In a more concrete form, the proposed 2D and 3D implementation of the wavelet method is to treat the signal at each point in the domain as a 1D signal in the form s(x,y,z,t), and perform the 1D wavelet analysis at each point. The resulting correlation coefficient set produced has the same form but with spatial components (x, y, and z) as well. Figure 3 illustrates going from single component decomposition to three components.

For a 1D signal, the correlation coefficient contour map is plotted as frequency versus time with the contour intensity based on the level of correlation. In order to effectively visualize the decomposed frequencies in a spatial frame, not all parameters may be looked at simultaneously. The most practical and useful way to visualize the

result is to fix the frequency that is to be visualized, and plot the contour of the instantaneous correlation coefficients for a specific frequency at a specific time at the appropriate spatial locations. By time stepping the contour plot, the spatial field of coefficients shows how the frequency propagates through the field and eventually dies out. In three dimensions, iso-surfaces may be used to display correlation coefficients in the same manner. The formulations for these approaches are given by equations 5 and 6 for two and three dimensions respectively.

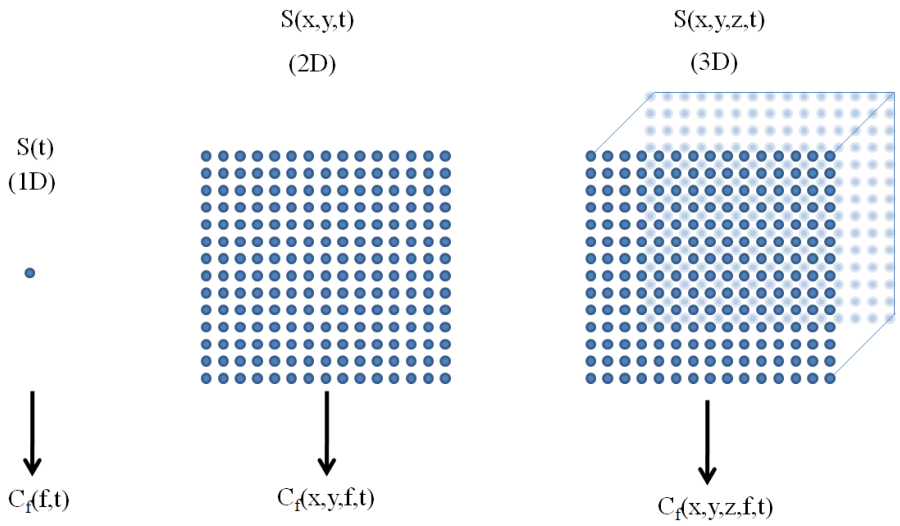

Figure 3 Schematic of translation from 1D to 3D spatial mapping of 1D wavelet transform

$$C_f(x,y,f,\tau) = \int_{\mathbb{R}} s(x,y,t)\overline{\psi_{a,\tau}(t)}dt \quad (5)$$

$$C_f(x,y,z,f,\tau) = \int_{\mathbb{R}} s(x,y,z,t)\overline{\psi_{a,\tau}(t)}dt \quad (6)$$

In addition to fixing one of the values, time averages and sums (equations 7 and 8) of the coefficients at a particular frequency over the 2D set of signals gives an indication of everywhere the signal was detected in the domain and the level of dominance at these locations. While this approach loses the benefit of the instantaneous decomposition, it may be used for an entire range of frequencies to determine those frequencies of interest to decompose using the instantaneous approach.

$$\overline{C_f(x,y,f)} = \frac{1}{\tau_{max}} \int_{\tau=0}^{\tau max} C_f(x,y,f,\tau) d\tau \quad (7)$$

$$C_{fsum}(x,y,f) = \int_{\tau=0}^{\tau max} C_f(x,y,f,\tau) d\tau \quad (8)$$

This novel application of an already well established method provides a valuable tool for engineers and scientists that are interested in propagation of frequencies within a flow. The obvious application would be for a design engineer who is interested in avoiding the generation of a frequency in the flow that matches the harmonic resonance of a particular structural component. With this method, the engineer may quickly determine where a frequency is generated so that corrective design measures may be taken. The simplicity of the implementation allows for the method to be used on data sets other than vector fields. The signals from raw camera pixel data extracted from a video may be used in the exact same manner.

The structure of the time series of data is constructed as illustrated in figure 4 and figure 5. The sample image shown in figure 4 is an enlarged 20 by 10 pixel image with the corresponding grayscale values for each pixel listed in the matrix. In order to

perform the proposed wavelet method on the time dependent signal of each pixel, a restructuring of the data is performed as shown in figure 5. The first array represents a single matrix that has been concatenated into a single column array. The same restructuring is done for each image in the time series and these columns are concatenated with one another to form a single two dimensional matrix where each row may be read directly as a signal.

The wavelet decompositions of each signals is computed; however, due to the computational expense of this process for large arrays of data, the program was parallelized across 24 cores. The performance for the instantaneous decomposition and output of results for an 800x600 pixel array of data with 1000 time steps is approximately 5 minutes for a single frequency. When normalizing the data across multiple frequencies, the time required increases by approximately 3 minutes per frequency considered. Each frequency decomposition method has advantages and drawbacks. The next section uses synthetic data to provide a well controlled verification case to test the applicability and find the limitations of the method.

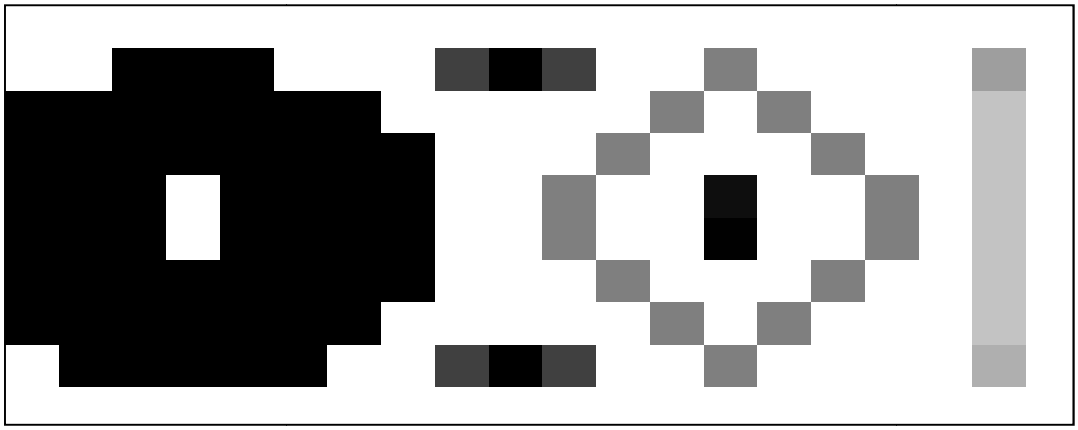

	i=1																			i=20
k=1	255	255	255	255	255	255	255	255	255	255	255	255	255	255	255	255	255	255	255	255
	255	255	0	0	0	255	255	255	64	0	64	255	255	127	255	255	255	255	158	255
	0	0	0	0	0	0	0	255	255	255	255	255	127	255	127	255	255	255	195	255
	0	0	0	0	0	0	0	0	255	255	255	127	255	255	255	127	255	255	195	255
	0	0	0	255	0	0	0	0	255	255	127	255	255	14	255	255	127	255	195	255
	0	0	0	255	0	0	0	0	255	255	127	255	255	1	255	255	127	255	195	255
	0	0	0	0	0	0	0	0	255	255	255	127	255	255	255	127	255	255	195	255
	0	0	0	0	0	0	0	255	255	255	255	255	127	255	127	255	255	255	195	255
	255	0	0	0	0	0	255	255	64	0	64	255	255	127	255	255	255	255	175	255
k=1 0	255	255	255	255	255	255	255	255	255	255	255	255	255	255	255	255	255	255	255	255

Figure 4 Example of matrix representation of grayscale image data

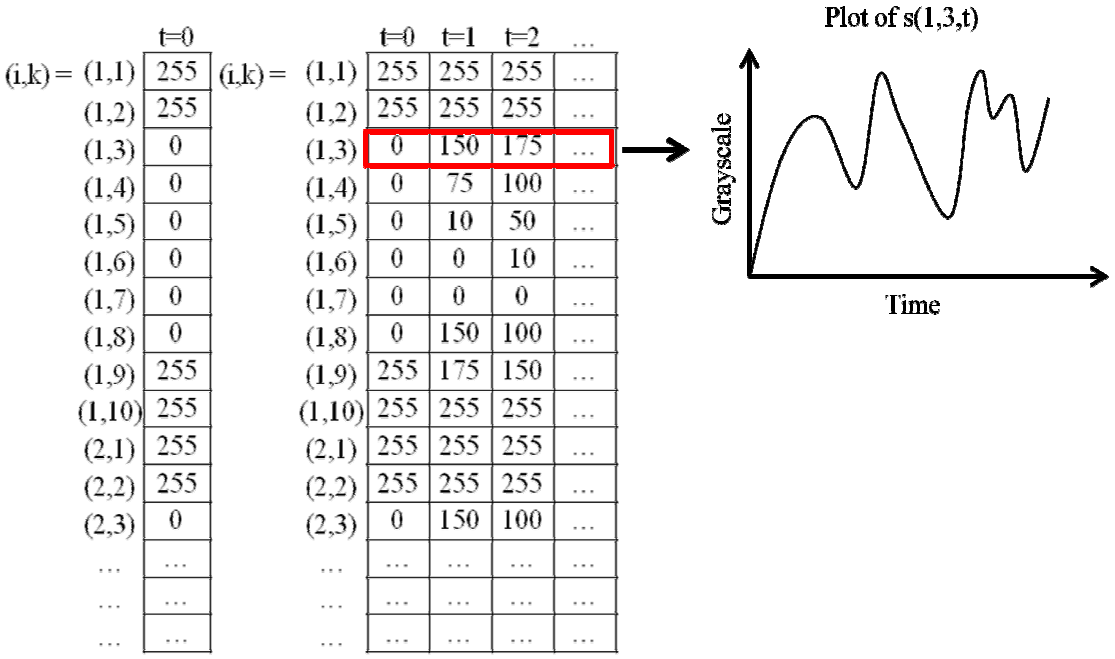

Figure 5 Example of concatenation of matrix into single column and concatenation of sequential time-step columns

2.4 Verification of the Spatio-Temporal 1D Wavelet Method

This section provides the verification tests of the spatio-temporal methods proposed. The method verification tests are conducted is by using a series of synthetic images of fan blades rotating at a specified rotation rates. The images were given a two pixel Gaussian blur to avoid unrealistically large discontinuities in the signals that are not intended to be handled by this method. In addition to the fan blades rotating, they also translate at different speeds to test that the routine maintained integrity even in the presence of a fleeting frequency. A sample image is shown in figure 6 and figure 7, with the appropriate rotation rates and effective frequencies indicated respectively. The

effective frequencies are based on the presence of four blades per fan. The instantaneous decomposition shown in figure 8 at the characteristic frequencies of the fans illustrates how the dominant frequencies are depicted. In the case of the 4 Hz decomposition, the 2 Hz fan is present due to the presence of both a start and end to each fan blade. As a result, the method detects the presence in these locations as well; however, the magnitude of the correlation coefficient for this frequency is reduced. Similar presence of other frequencies are shown in the 2 Hz, 0.8 Hz, and 6 Hz cases, but as before, the dominant frequency is clear in all four cases.

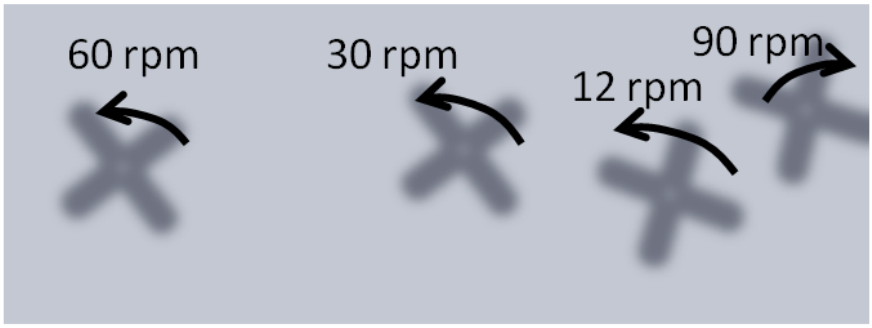

Figure 6 Rotation rates of synthetic images for wavelet verification

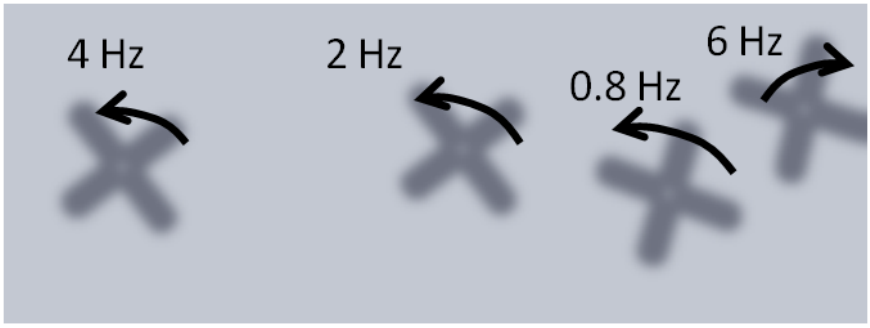

Figure 7 Effective frequencies generated for wavelet verification

To test that such multiplier effects are not present at higher frequencies, decomposition at 24.3 Hz was performed and the correlation coefficients were found to be negligible. It is important to note that all of the decompositions have been normalized against one another. In this manner, only the dominant frequencies are visualized. Had each frequency been normalized only against the maximum coefficient value over that particular frequency, the multiplier factors become overly abundant and visually misrepresent which frequencies are truly the most dominant over the entire range tested.

The time averages of the validation case at each of the frequencies as described by equation 5, is shown in figure 9. In this series of images, the primary location of each frequency is indicated, with the intensity corresponding to not only the intensity of the frequency, but also the presence over the length of the signal. As mentioned previously, the fan blades in the image were not only rotating, but were also being translated. In the case of the 4 Hz and 2 Hz, the amount of translation was a fraction of the overall diameter of the fans. In the case of the 0.8 Hz fan, the fan translated by one diameter to the left and reduced in diameter by 25%. In the average image, this becomes clear by the significant smearing and size reduction of the coefficient concentration. In the case of the 6 Hz fan blade that had a large translation during the signal span, the average value diminished, but is still distinguishable. As expected for the 24.3 Hz case, the average value was also negligible.

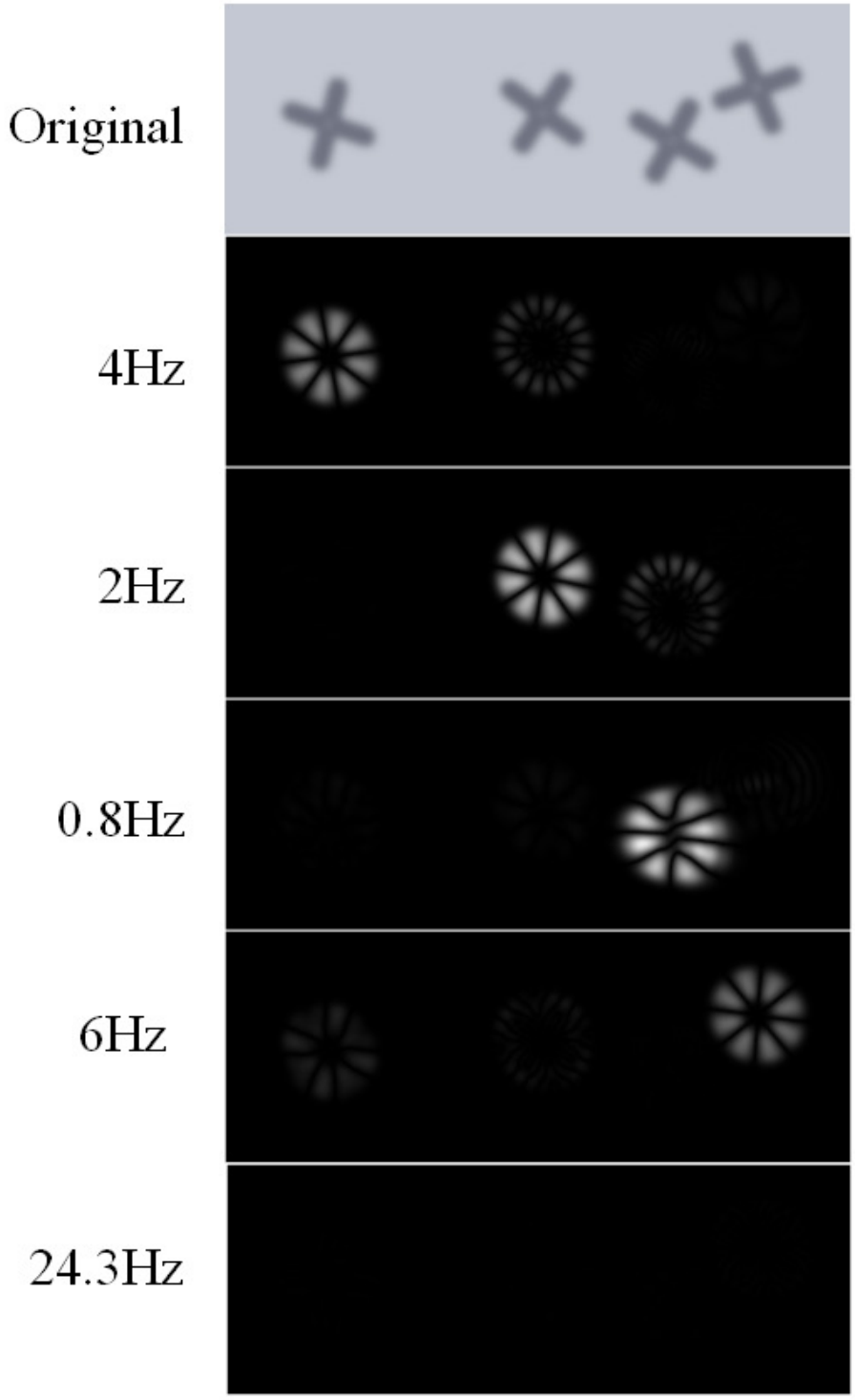

Figure 8 Instantaneous correlation coefficients of synthetic images at various frequencies

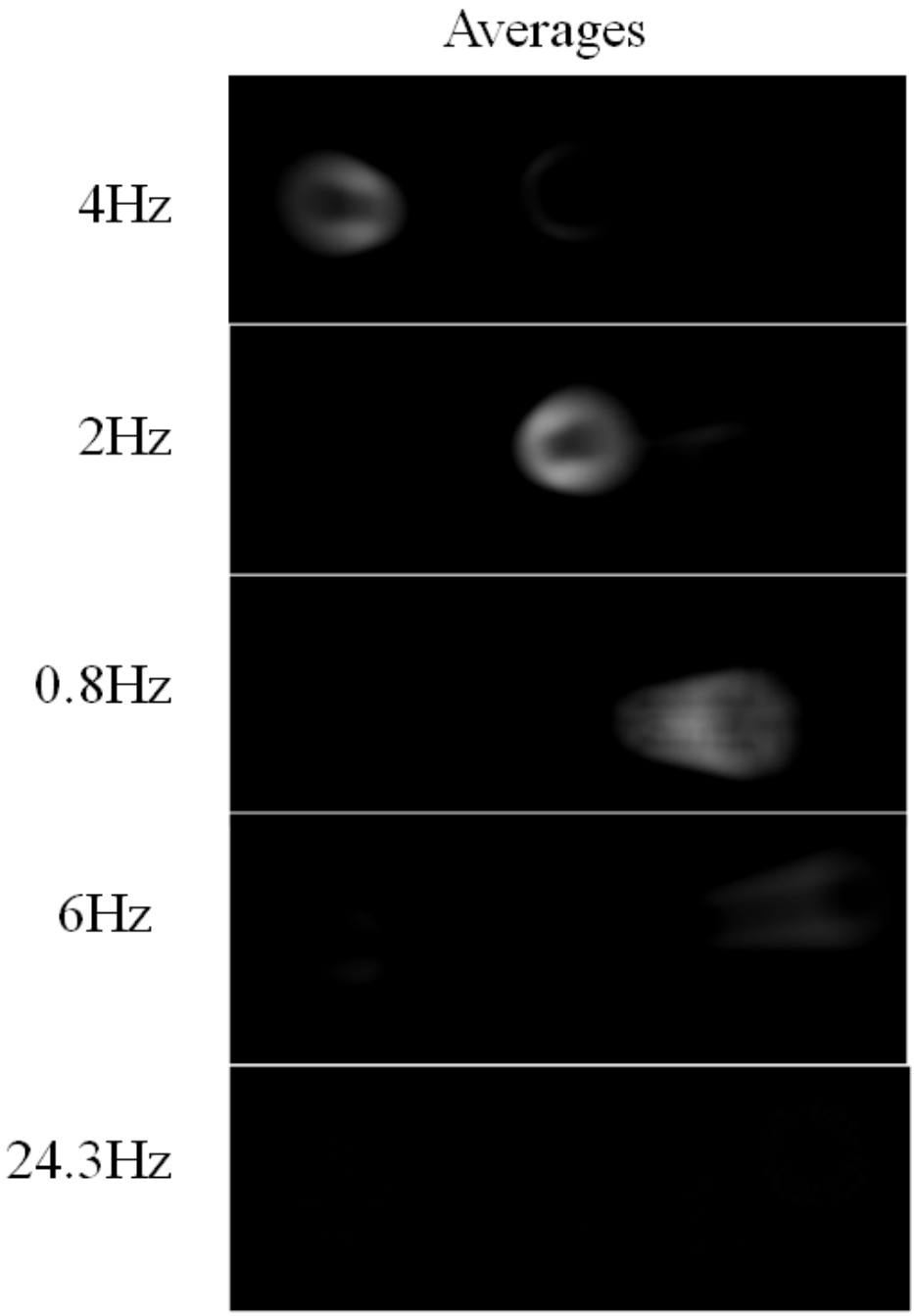

Figure 9 Time averages of correlation coefficient of synthetic images at various frequencies.

3. TEST CASES

3.1 Side Entry Orifice Experiment of GE BWR-6

Advances in the field of high fidelity thermal hydraulics simulations are promising for both design and licensing applications in the nuclear industry; however, with the increased precision of such simulations comes the need to validate them against experiments of equal or better quality. The current work details an experiment of flow just prior to the side entry orifice of a boiling water reactor (BWR). Such an orifice is located on a column and has both nuclear and other industrial applications where take-off orifices are needed. The experiment consists of axial flow along the outside a large diameter cylinder with a takeoff orifice within the cylinder. Flow through the orifice produces large standing vortices and complex flow patterns that cannot be solved analytically and simulations of such flows have not been validated thoroughly. For this reason, experiments in this area are essential in understanding the physics and producing reliable data sets for validation. This work details the facility design, difficulties of the current experiment, and the mitigation strategies employed to overcome them to produce a high quality validation dataset.

3.1.1 Introduction of GE BWR-6 Side Entry Orifice

One of the typical characteristics of boiling water reactors (BWR) is the use of self enclosed fuel assemblies in which coolant is channeled through each assembly, but is not free to interact with other neighboring assemblies. As coolant water flows up through the assembly, it eventually boils to produce high quality steam at the outlet for electricity generating steam turbines. Providing coolant to these channels through the bottom end of the structure means that the core plate serves the purpose of both supporting the fuel assemblies as well as providing a conduit for coolant to bypass the support plate and enter each individual assembly. In some early designs, this was done by a simple hole in the core plate that allowed water to flow directly upwards into the assemblies. In the case of the GE BWR-6, the support columns under each 2x2 fuel assembly block contain four right angled conduits that open through the face of the column and allow for flow to pass the core plate. These 'side entry orifices' instill higher pressure drops and much more complicated flow patterns than the straight through core plate bypass designs typical of BWRs. The need to understand the flow patterns surrounding these features and obtain very accurate pressure drop correlation information across this region is necessary for improving the fidelity of system codes employed for this reactor design. It is the goal of this work to satisfy these missing pieces of validation data as well as provide additional verification data to the wavelet methods described and developed.

Flow through the SEO has been predicted computationally, but limited experimental data is available to validate the dynamic structures thought to be forming in these regions. For many years, studies of vortex formation from orifices placed on the bottom of a vessel have been performed for application to industrial processes. The current study investigates the presence of a standing vortices formed at an orifice inlet with a normal vector perpendicular to the gravity vector. The resulting vortex cores form horizontally. In the present study, high fidelity experimental measurements are performed in order to better understand the steady vortices in orifice flows that have previously been performed as separate effect tests, but are presently investigated as a large scale test to provide validation data as well as pressure drop correlation data.

Standing vortex studies are typically performed under gravity or rotating table conditions where the vortex core remains highly stable. A study by Nahas *et al.* [8] investigated the generation of a vortex column under gravity conditions. They found that the tangential velocity of the vortex increased linearly with increasing circulation flow rate. In their study, the importance of the boundary layer on the presence and intensity of the vortex column is shown. By perturbing this layer with geometric features to increase the thickness, δ, the vortex may be attenuated. In the present study, rather than the orifice being located on a flat plane, it is instead located on the side of a column with an orifice/column diameter ratio of 0.235. As a result, the effect of the boundary layer on the vortex is reduced. In the present study, rather than the orifice being located on a flat plane, it is instead located on the side of a column with an orifice/column diameter ratio of 0.235. As a result, the effect of the boundary layer on

the vortex is reduced and the size and intensity of a vortex may even be increased due to the lack of a boundary layer to constrain the vortex formation.

An experimental study by Watanabe *et al*. [9] dealt with many columns representing the lower plenum of an Advanced Boiling Water Reactor (ABWR). Each column has four right angle orifices located circumferentially around the axis of each column. This earlier experimental study by Watanabe *et al.* is complimentary to the current study in that it provides global information across multiple columns, whereas the current study provides local flow information about a single orifice at higher Reynolds numbers than obtained in the previous study. The study was initiated as part of a program to validate such flows being simulated for various reasons, including boron injection modeling by Yan and Mallner [10].

In another study[11], the effect of the vortex on flow through an orifice is shown to decrease the discharge rate for pool type scenarios where the vortex formation is vertical. Although the Reynolds numbers are higher in the BWR, the presence of the vortex in the SEO may lead to a higher pressure drop across the orifice. In the GE BWR-6, the core support structure and assembly/SEO arrangement is depicted in figure 10 [12]. In this configuration, the direction of the flow is normal to the schematic, and traverses a solid plate by entering the side entry orifice before flowing into the bundles indicated in blue, orange, and red. The significance of the colors is to differentiate the different types of sub-channel arrangements present outside the SEOs. According to a US NRC published document[12], loss coefficients across the orifice with one adjacent

wall is 20% higher than that with no adjacent walls. Likewise, the orifice with two adjacent walls has a loss coefficient 40% higher than that without any adjacent walls.

While there has not been conclusive evidence, it may be possible that in addition to the effect of the reduced sub-channel size, the corner SEOs tend to have stronger and more well defined vortices due to limited communication with other large scale flow structures otherwise present in the larger sub-channels. This is purely hypothesis and would require an extensive testing program involving an even larger scale facility to examine such wall effects. For the present study, a single corner sub-channel with two adjacent walls is investigated, with a geometrically representative orifice and expansion region prior to the fuel assembly that is scaled directly 1 to 1 from the actual reactor design. The next section provides more detail of the facility.

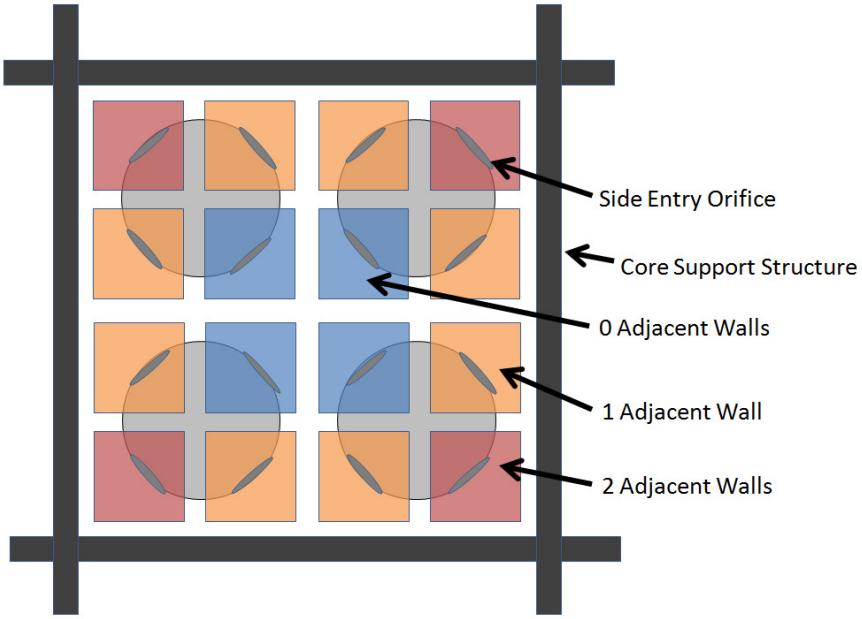

Figure 10 Schematic of BWR-6 side entry orifice orientation with respect to the core support structure.

3.1.2 Experimental Setup

The need to obtain CFD validation quality data in the region just outside the side entry orifice of the GE BWR-6 led to the design of a large scale test facility consisting of a single side entry orifice facing two adjacent walls, as well as an expansion region before a mock fuel assembly. Although the area of interest is across the orifice and not in the fuel assembly itself, the short bundle with tie plates is present in the experiment to accurately represent the pressure drop of the flow entering the assembly, which inevitably leads to certain upstream effects in the vicinity of the post-SEO pressure transducer.

The experimental facility, illustrated in figure 11 through figure 14, consists of a cylindrical column 24" tall and 10.625" diameter inside a 12"x12"x24" ± 0.005" rectangular solid channel. The acrylic walls of the channel are 0.91" thick to provide rigid walls while maintaining optical access for flow visualization measurements. Water flows only along a 90 degree section between the cylinder and channel walls as indicated by red in figure 12. This flow channel is 6" along each flat wall, and a quarter cylinder along the other main wall. Acrylic flow barriers (0.69"x0.25"x24"), shown in the same figure, were used to section off the flow channel to prevent bypass flow from the other three quarters. While flow was not passing through these other channels and inner cylinder, they were also filled to prevent stress cracking or bowing in the flow channel. Prior to the upper impingement plate of the channel, a single circular counter-sunk orifice with a 2.5" diameter is oriented towards the corner of the channel and provides

the only conduit for flow to exit the test section. The orifice center is situated 4.90" ± 0.005" from the upper impingement plate. The orifice is approximately 0.60" ± 0.002" deep before making a 90° turn upwards. A circular to square expansion is located 8" above the orifice center and converts the take-off orifice geometry to a square channel 4.94"x4.94" ± 0.005". All geometries were with the exception of the expansion which was simplified just slightly for manufacturing purposes, were built to the same geometric scale and shape provided for this reactor design.

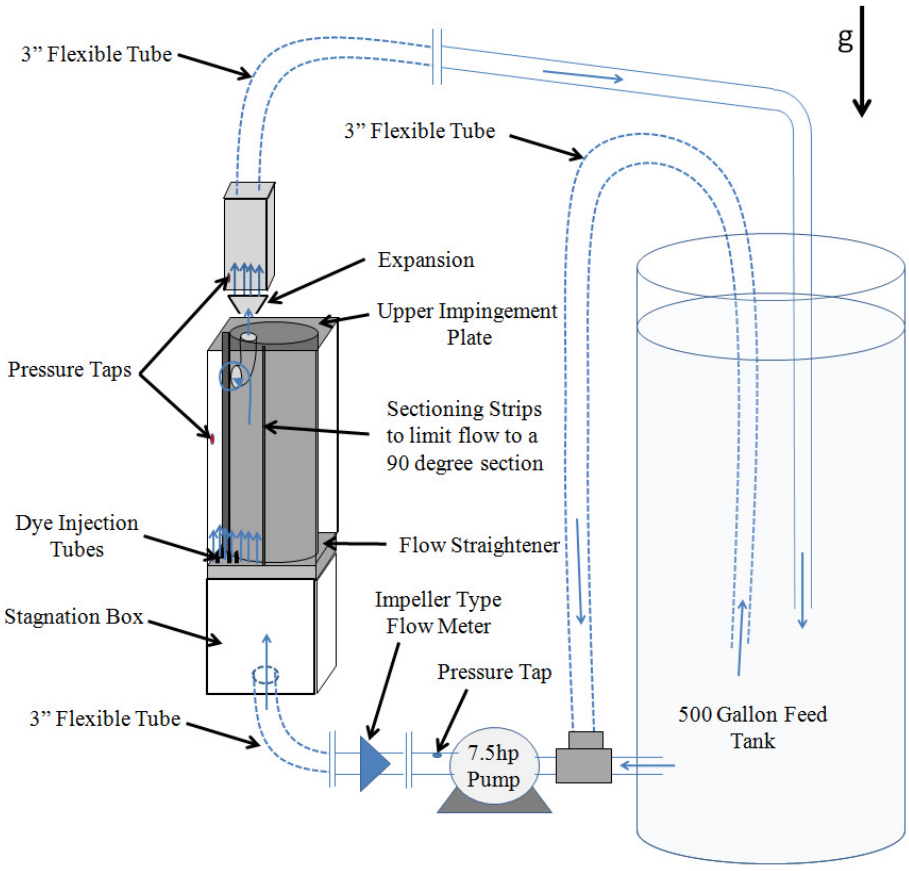

Figure 11 Schematic of Texas A&M University SEO experimental facility

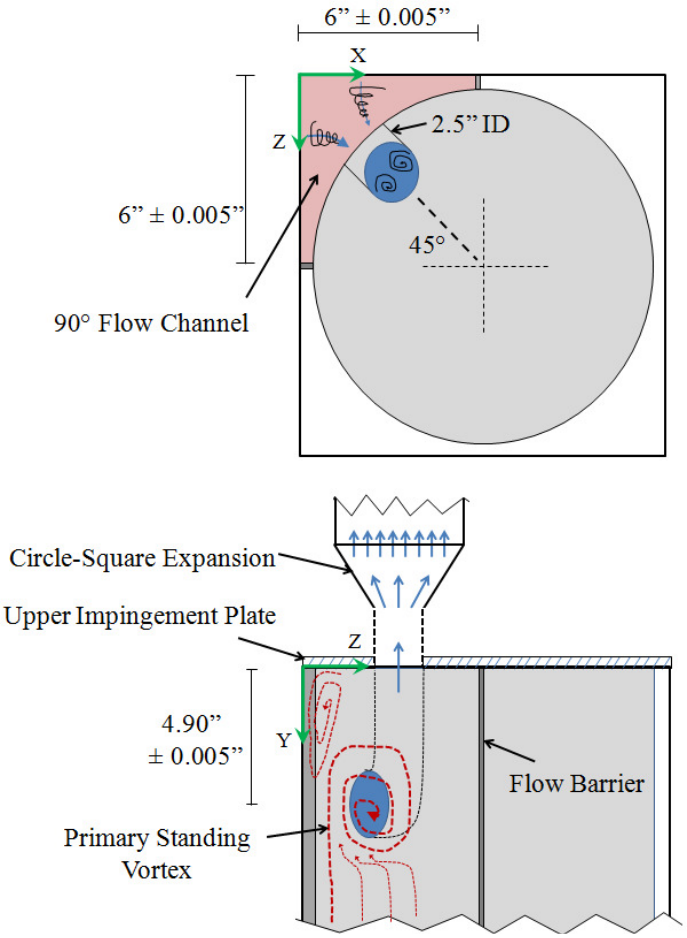

Figure 12 Side entry orifice orientation and position with respect to core (impingement) plate and sidewalls.

A calibrated Data Industrial SDI impeller type insertion flow meter was used to measure volumetric flow rate through the inlet pipe to the test section. The location along the loop of this flow-meter is indicated in figure 11, just prior to flow entering the test section. In accordance with manufacture guidelines, more than 10 hydraulic diameters of straight pipe before and 5 diameters following the flow meter were used to maintain the ±1% rate accuracy for the sensor. The flow rates measured with this flow meter were used to calculate the Reynolds number based on the average velocity through

the 2.5” side entry orifice diameter. The full technical brief and specification sheet are included in the supplemental data package.

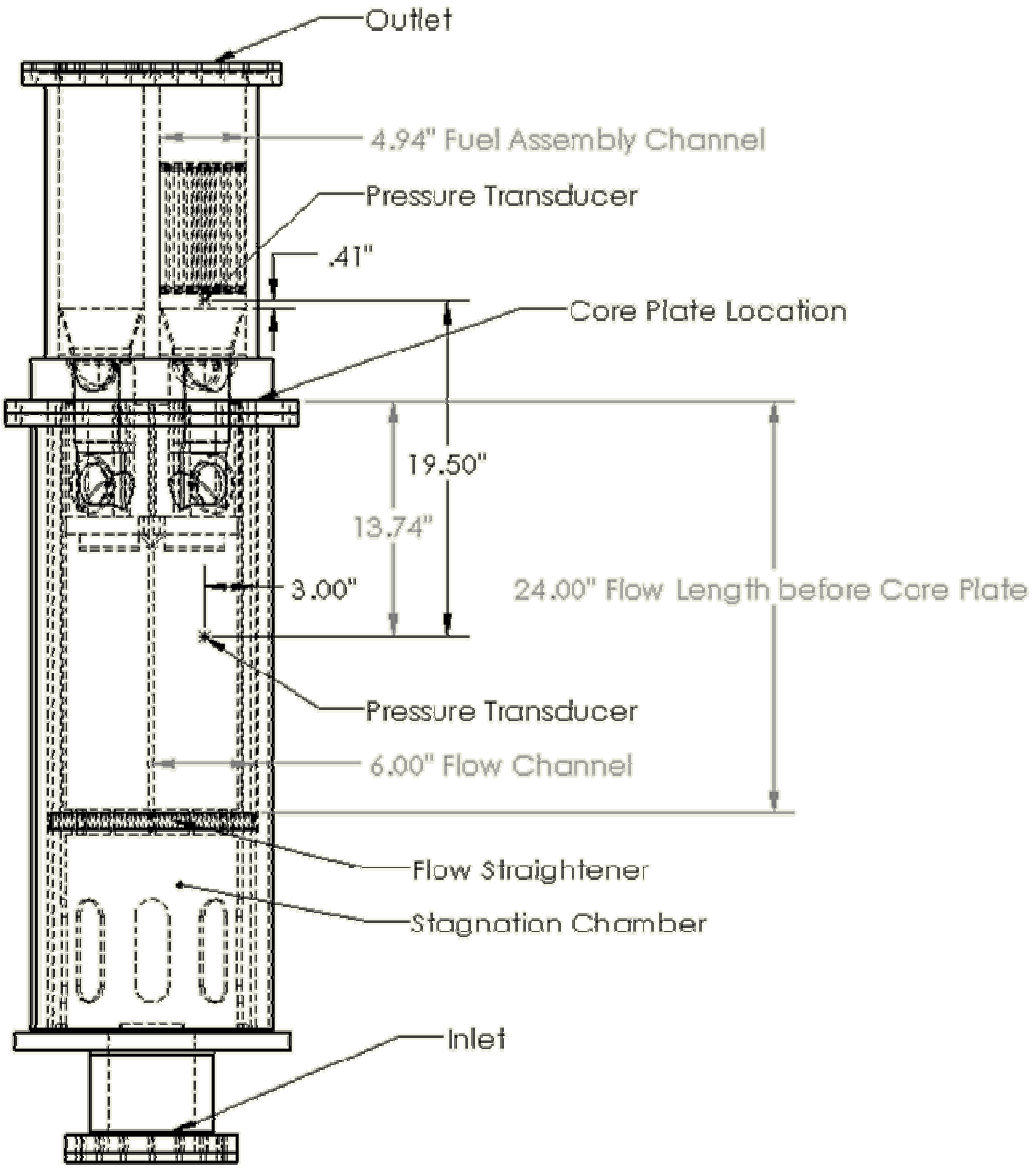

Figure 13 Schematics of experimental facility with pressure transducer locations

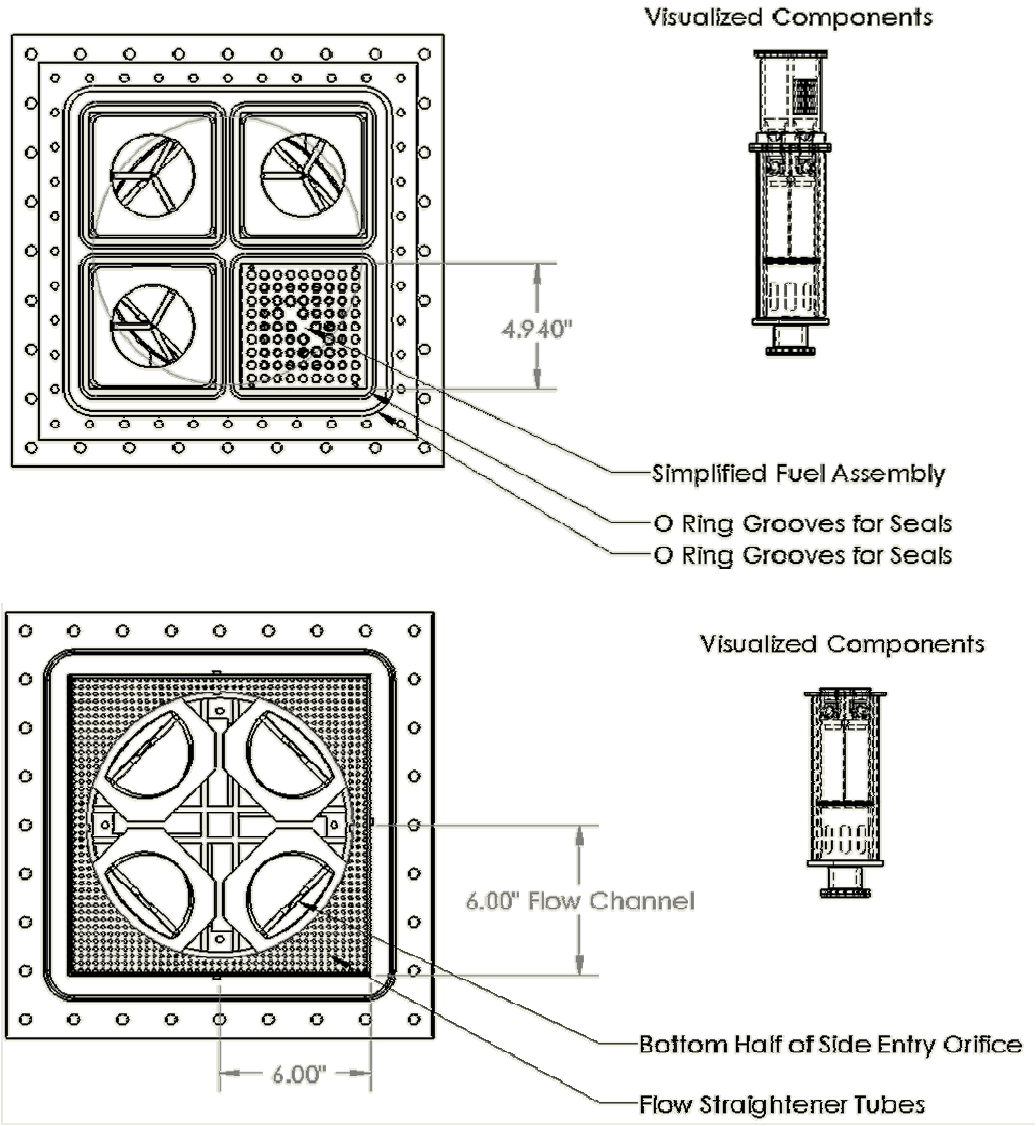

Figure 14 Top view schematics of experimental facility with pressure transducer locations indicated

3.1.2.1 Pressure Measurement Cases

Initially, a feed tank volume of 150 gallons was used for performing measurements, but two significant problems arose. Significant amounts of micro-bubbles were present in the flow. As will be discussed later, particle tracking velocimetry relies on the use of particles with a specific gravity close to that of water to faithfully follow the flow. In addition to the bubbles being mistaken for particles, the density difference between the gas and liquid phases led to the orifice acting as a cyclonic separator, forming a well defined gas filament in the vortex cores similar to that shown in the experimental work of Movafaghian *et al*. [13]. As a two phase regime in this region is not characteristic of normal operating conditions in the BWR-6, the elimination of air bubbles the flow was necessary. As the feed tank water volume was increased to 300 and eventually 500 gallons, bubbles were reduced to the point that they were no longer visible in the camera images and any smaller bubbles that might reflect laser light would be filtered out through the use of laser induced fluorescent particles and light filters on the camera lenses (this technique is described in more detail later). Fortunately, the principle of the cyclonic separator worked to the advantage of the experiment, purging all trapped air bubbles present at the startup of the experiment rather than them pooling in locations just before the core plate of the test section. It was found that letting the flow loop run for approximately one hour at 100gpm with the 500 gallon tank, the flow loop degassed itself to the point that no noticeable quantities of micro-bubbles were visible in the test section.

Through the process of eliminating the micro-bubbles, it was found that the height of the tank volume played a large role in the accuracy of pressure measurements across the orifice. When the tank volume was 150 and 300 gallons and the Reynolds number was below $1.0x10^5$, the flow loop siphoned from the experiment, resulting in a positive gauge pressure prior to the side entry orifice and a negative gauge pressure afterwards. At low pressures, the accuracy of the large range pressure gauges diminishes, and by increasing the tank level above the height of the experiment, the issue was mitigated and the accuracy of the transducers regained.

Piezoelectric pressure transducers with frequency responses of 1 kHz and maximum operating pressures of 30 psig were placed 8.675" downstream of the orifice center and 0.41" past the circle-square expansion section located in the bottom tie plate. These locations are indicated in the experimental schematic in figure 13. Additionally, an identical pressure transducer was placed just downstream of the 7.5 hp pump in test set 2 to catch dominant fluctuations generated by the operating frequency of the pump. The specifications of the pressure transducers used are provided in table 1, and the Reynolds numbers as which pressure measurements were taken across the orifice are indicated in tables 2 and 3.

Table 1 Piezoelectric pressure transducer specifications

Pressure Transducer Model:	PX309-030G5V
Long-Term Stability (1 Year):	±0.25% typical
Accuracy:	±0.25 FS BSL ≈ ±0.2 psi
Typical Life:	10 million cycles
Operating Temperature:	-40 to 85°C (-40 to 185°
Proof Pressure:	90 psia
Burst Pressure:	150 psia
Response Time:	<1 ms
Shock:	50 g, 11 ms half-sine
Vibration:	±20 g
Pressure Port:	1/4-18 MNPT

Table 2 Pressure measurement data set 1 test cases

Test Type	Pressure Data
Test Number	1
Folder Name	Pressure Test 1
Pressure Transducer Type	30 psig piezoelectric
Transducer Frequency	1 kHz
Flow Rate (gpm)	**$Re = \frac{\rho U D_{orifice}}{\mu}$**
85	129031
90	136621
95.5	144970
101.5	154078
106	160909
110	166981
115.5	175330
120.75	183300
123	186716
133.5	202655
136	206450

Table 3 Pressure measurement data set 3 test cases

Test Type	Pressure Data
Test Number	2
Folder Name	Pressure Test 2
Pressure Transducer Type	30 psig piezoelectric
Transducer Frequency	1 kHz
Flow Rate (gpm)	**$Re = \frac{\rho U D_{orifice}}{\mu}$**
91	138139
100	151801
107.5	163186
114	173053
120	182162
125	189752
130	197342
133.5	202655

Pressure transducers were calibrated with a water column to verify their ±0.25% (±0.2psi) accuracy. Calibration of pressure transducers have been performed using a water column for verification of measurements in low pressure conditions. The pressure transducers were found to be within the vendor accuracy specifications.

3.1.3 2D Particle Tracking Velocimetry (PTV) Methods

3.1.3.1 Dynamic and Straddling PTV

The general principle of particle tracking velocimetry (PTV) is fairly straight forward. Two images are taken with a pulse of laser light formed into a thin sheet of light in each frame for illumination. Particles that are seeded within the flow reflect photons that are then detected by a high speed camera. Through the use of a cross correlation, the particles in the first frame are matched with themselves in the second frame following a translation with flow. By knowing the distance of translation and the time between the frames, two velocity components may be extracted from the images. While the principle is straight forward, there are many intricacies involved in successful implementation of the method to obtain accurate data.

A high speed CCD camera was used to capture seeding particles illuminated by high speed pulsed laser light. For the time resolved measurements, a New Wave twin cavity Pegasus PIV Nd:YLF laser along with laser optics were used to pulse a 1.5mm thick light sheet at 527nm with a frequency of 1 kHz and an average output power of 8mJ per pulse. At 1 kHz pulse frequency, the pulse power from the laser is sufficient for the CCD camera to capture the moving particles; however, at Reynolds numbers above 1.30×10^5, a higher frequency is needed to faithfully track particles between captured images. This type of measurement in which the laser pulse frequency is constant and at a high repetition rate will be referred to as 'dynamic PTV.' Due to the reduction in laser

output power at higher pulse frequencies, there is insufficient light to capture images in a large flow field.

To mitigate the illumination issue, a technique of straddling is used in which a Spectra Physics twin cavity Nd:YAG laser capable of independent cavity firing each with a frequency of up to 30Hz but an output power of 300mJ per pulse. By firing each cavity in short succession (Δt =1ms to 0.25ms between cavities), the CCD camera exposes two sequential frames with an effective frequency of 1 kHz to 4 kHz. Between each set of straddled pulses, the 30Hz frequency is maintained for each cavity. This method will be referred to as 'straddling PTV.' The ramification of this frequency gap is that the power spectra at very high and very low frequencies are obtained but statistics in between are missing. Timing diagrams in figure Figure 15 further illustrate the differences between dynamic PTV and straddling PTV. The use of a twin cavity Nd:YLF laser provides an advantage over traditional Nd:YAG lasers by allowing high repetition rates to be achieved while sacrificing pulse energy, but the need for the higher laser power achievable only with the Nd:YAG laser using the straddling technique necessitated the decision to use this method of measurement. The specifications of the two lasers under consideration are provided in tables 4 and 5.

The high speed camera used to capture images of the illuminated particles was a Phantom v7.3 produced by Vision Research. While the camera has the capability to record images into the hundreds of thousands of frames per second (fps) at reduced resolution, it is only capable of capturing 6,688fps at full resolution. The current application only required between 1000 and 4000 fps. This also allows full resolution

images to be obtained, thus improving the overall accuracy. At full resolution (800x600 pixels), a maximum of 4399 frames may be obtained before the internal storage is filled. The CCD sensor provides 12-bit sensitivity which allows for the sub-pixel accuracy when locating the centroid of individual particles.

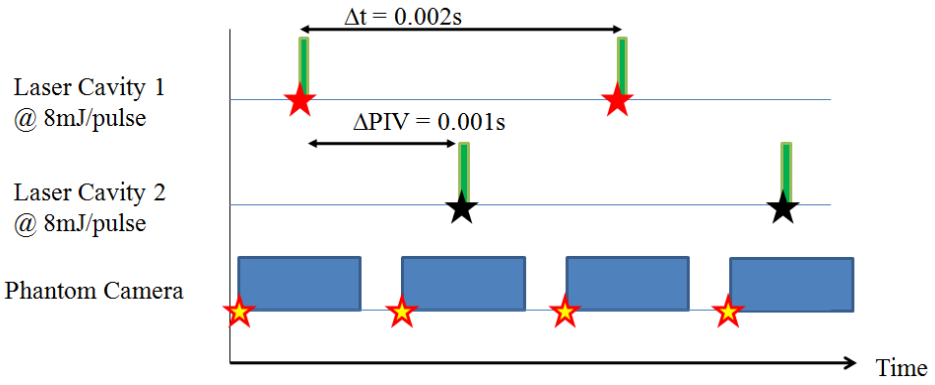

(a)

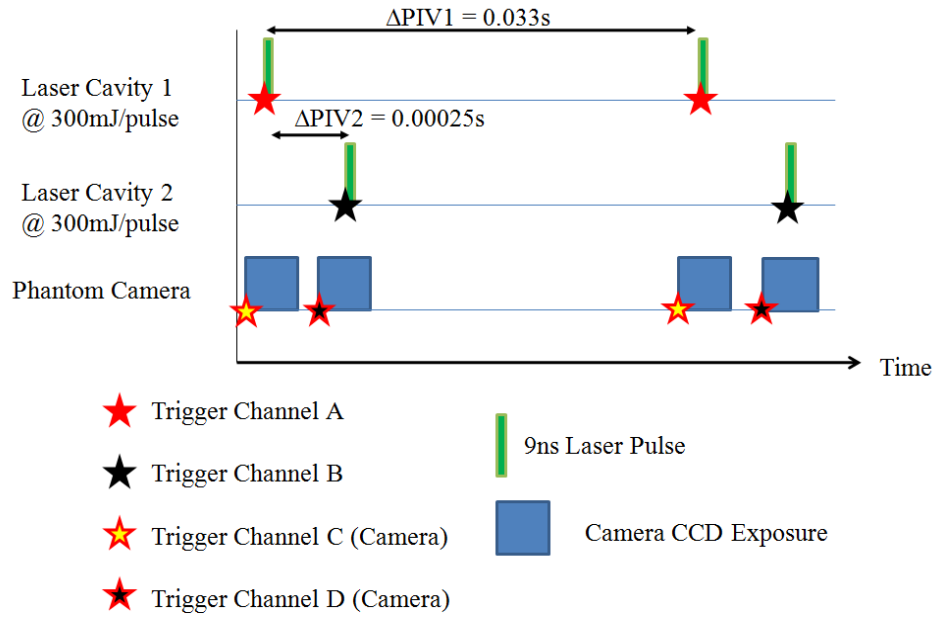

(b)

Figure 15 Timing diagrams for (a) dynamic and (b) straddling PTV

Table 4 New Wave laser specifications

Laser Model		New Wave Pegasus PIV Nd:YLF
Wavelength		527 nm
Repetition Rate	Dual Cavity System	2 cavities up to 10,000 Hz each
Energy	Dual Cavity System	10mJ @ 2,000 Hz (2x 1,000 Hz per cavity)
Beam Diameter		1.5 mm

Table 5 Spectra-Physics Quanta Ray laser specifications

Laser Model		Quanta-Ray PIV-400-30
Wavelength		532 nm
Repetition Rate	Dual Cavity System	2 cavities up to 30 Hz each
Energy	Dual Cavity System	300mJ @ 60 Hz (2x 30 Hz per cavity)
Beam Diameter		9 mm

To synchronize all of the devices involved in the data acquisition, a high precision 8-channel pulse generator was used. The twin pulsed Nd:YAG laser required four channels to initialize and fire each lasing chamber, the high speed camera required two channels to start capture prior to each laser pulse, and the data acquisition system for the pressure transducer required one channel to initialize the start of the measurements. This channel was also fed to the cameras to start measurements at the same time. A Quantum Composers 9500+ pulse generator was used for triggering due to the extreme sensitivity of measurements to any inaccuracies in the laser pulse timing.

As an example, assume the pulses or cameras are off by 100 microseconds in a 2.5 m/s flow measured by a camera with a spatial resolution of 4 pixels/mm. The optimal particle displacement between frames, according to previous sensitivity

studies[14], indicates a particle displacement of 4 pixels/time-step achieves the best results. If the camera sees a particle move 2500 mm/s, or 10,000 pixels/s, the time step needed to achieve this optimal tracking would be 0.0004s. The assumption of a pulse error of 100 microseconds results in an error of 25% in the resulting particle velocity. For this reason, the pulse generator chosen has a 1ns temporal resolution with less than 400 seconds of jitter to ensure this potentially large source of error is minimized to a negligible amount.

3.1.3.2 PTV Imaging Volume Calibration

One of the main challenges involved with particle tracking velocimetry measurements is the calibration of the images throughout the entirety of the volume. For the current experiment, 10 xy-planes with z locations described by tables 6 and 7 were illuminated in the fluid domain. The change in the distance photons must travel through air and water to reach the camera objective results in a zooming effect of the area of observation due to the differences in refractive indices of the fluids. This must be accounted for to ensure accurate velocity and location representation. This optical effect is illustrated in figure 16 in which the camera and laser sheet are translated by identical distances (Δz), but the resulting viewing window of the CCD camera differs between the two ($a_1 > a_2$) regions. As the CCD sensor is a constant 800x600 pixels, the relation of mm/pixels is adjusted depending on the plane location visualized.

Table 6 PTV measurement test 8 at Re=1.83E5

Test Type	PTV
Test Number	8
Folder Name	t9-100gpm-final
Orifice Reynolds Number	1.83E+05
Volumetric Flow-rate	120 GPM
PTV Method	Straddling
Straddling Frame Rate	4 kHz
Plane Number	**Z Position (mm)**
00 (2nd set of two)	4.83
3	19.46
4	34.10
5	48.74
6	63.37
7	78.01
8	92.65
9	107.28
10	121.92
11	136.56
12	151.19

Table 7 PTV measurement test 9 at Re=1.5E5

Test Type	PTV
Test Number	9
Folder Name	t8-120gpm-final
Orifice Reynolds Number	1.50E+05
Volumetric Flow-rate	100 GPM
PTV Method	Straddling
Straddling Frame Rate	4 kHz
Plane Number	**Z Position (mm)**
13	4.83
14	19.46
15	34.10
16	48.74
17	63.37
18	78.01
19	92.65
20	107.28
21	121.92
22	136.56

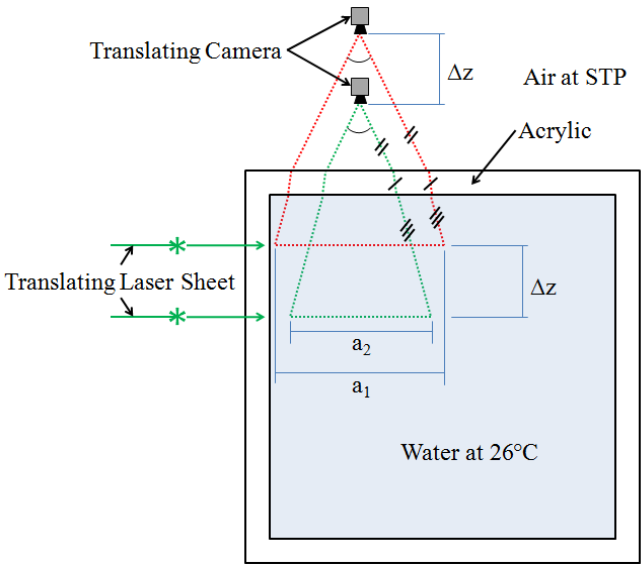

Figure 16 Zooming effect of adjusting camera and laser sheet positions synchronously

The calibration procedure involved a grid 150mm by 180mm placed in the xy-plane at position z=3.2mm. The front of the camera objective, initially at z=-258.0mm, and the calibration grid were incremented at a Δz=6.53mm for 26 total planes that cover volume of interest for the measurements. Seven different coordinates with varying radiuses from the center of the effective zoom, also known as the principle point, were chosen and tracked in each image. This data was used to generate translation and zoom maps for adjusting the data.

The importance of choosing various positions off axis from the principle point (zoom center) are that many camera lenses produce a fisheye effect that can cause dependence on x, y, and z directions. The selection of positions on the x and y axis allows these to be accounted for if they are present, and the off axis points are to verify the result. The resulting maps verified the presence of a linear zoom with respect to

plane position as well as determined this zoom effect to be dependent on radial distance from the principle point.

The principle point was obtained by picking points on the calibration grid and tracking the pixel locations in each image. By extrapolating through the tracked points, a point of intersection is found that corresponds to the principle point. Figure 17 shows a portion of the calibration grid with tracked points and the principle point determined by the extrapolated lines in figure 18.

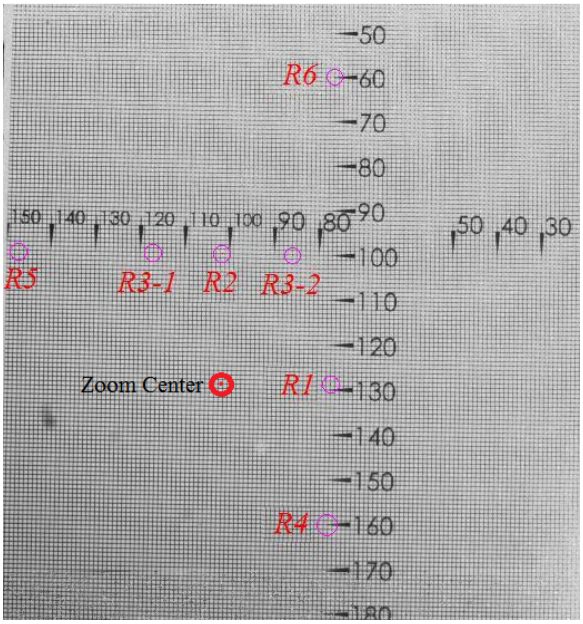

Figure 17 Calibration grid image with points tracked for zoom adjustment. The principle point (zoom center) is indicated on the grid.

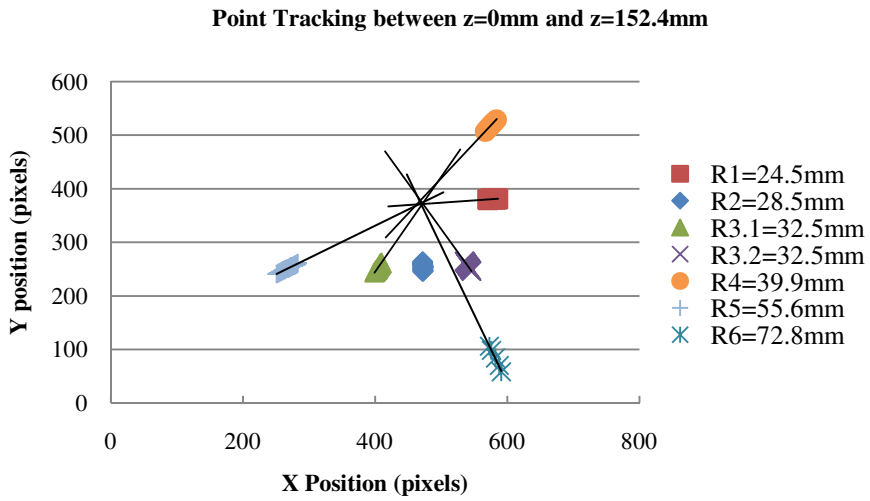

Figure 18 Extrapolated lines from observed tracking point locations over all the calibration planes. The principle point is located at the intersection of the lines.

Failure to account for this zoom through the domain would result in a synthetic 19% variation for a uniform velocity from z=0mm to z=152.4mm as implied in the calibration data plots in figure 19. The resulting calibration equation for adjusting velocities from the pixel/time-step data obtained from particle tracking velocimetry routine is shown in equation 9, where CF is the conversion factor in mm/pixel units that is to be multiplied by the velocities to obtain mm/time-step units. The final calibration relations for corrected velocities, u_c and v_c, are given by equations 10 and 11.

$$CF(z) = -0.0002 \cdot z + 0.2414 \quad \text{(mm/pixel)} \tag{9}$$

$$u_c(x,y,z) = \frac{u_p(x,y,z) \cdot f \cdot CF(z)}{1000} \quad \text{(meters)} \tag{10}$$

$$v_c(x,y,z) = \frac{v_p(x,y,z) \cdot f \cdot CF(z)}{1000} \quad \text{(meters)} \tag{11}$$

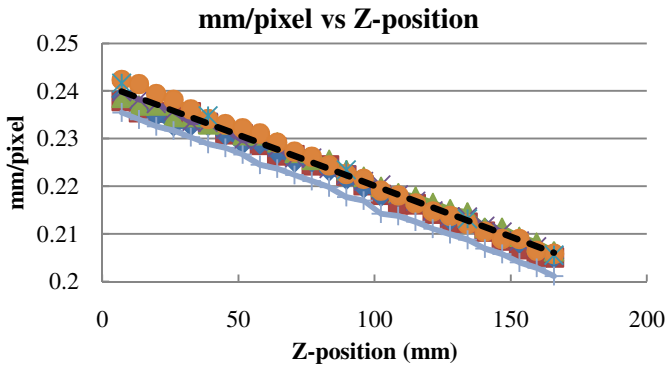

Figure 19 Correlation data and extrapolated coefficient CF (eqn.9) indicated by the dashed line. Plot legend in Figure 18.

Similarly, positions are adjusted to account for zoom about the principle point by determining the rate at which points expand out from the principle point with respect to the radial distance as well as z position. At the principle point, the location appears to remain in the same location; however, because the velocity maps are to be adjusted to account for the zoom, these principle point locations must be repositioned to all line up with one another.

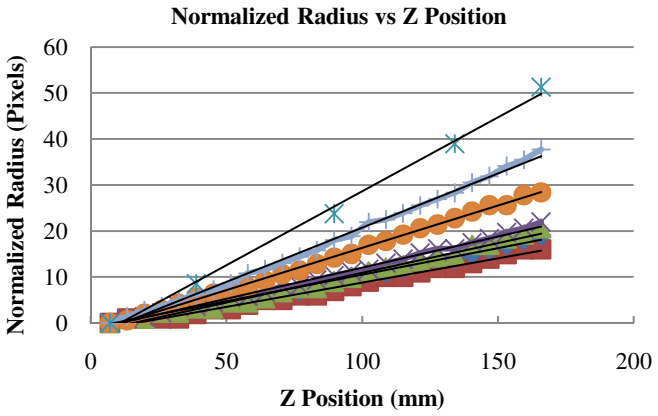

Figure 20 Normalized observed radiuses of each point from the principle point with respect to Z position. Plot legend in Figure 18.

The normalized radius, NR, (eqn. 12) in figure 20 represents the change in observed radius (in pixels) of the specified points on the calibration grid at each Z-position. The increasing slope coefficient of these lines, α, with respect to increased physical distance (R) from the principle point can be closely approximated by the linear regression (eqn. 13*)* shown in figure 21.

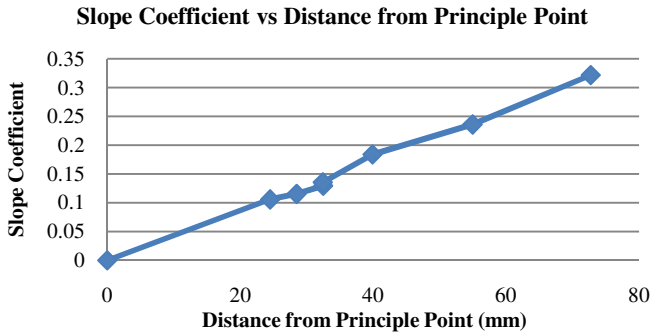

Figure 21 Slope coefficient, $\boldsymbol{\alpha}$, of radius zoom factor with respect to physical distance from the principle point.

$$NR(x, y, z) = \alpha(x, y) \cdot z - 2.1122 \tag{12}$$

$$\alpha\,(x, y) = 0.0046 * R(x, y) - 0.0056 \tag{13}$$

Where

$$R(x, y) = \sqrt{(x - x_0)^2 + (y - y_0)^2} \tag{14}$$

Fortunately, this linear relationship with respect to distance from the principle point means that the calibration process may use the simplified correction factor relationship, CF(eqn. 9) to resize the image, with the addition of the change in principle location. These relationships for x and y positions are given in equations 15 and 16; where x_p and y_p, are in pixels, z is in mm, and Xop and Yop are the principle point

locations in pixels (Xop=470 and Yop=379). The term Ycorrection takes into account that the top of the first image was not located directly at the underside of the core plate. This adjustment value is Ycorrection=0.0201m.

$$x_c(x,z) = \frac{x_p \cdot CF(z) + (z - zo) \cdot (-0.0002) \cdot Xop}{1000} \quad (meters) \tag{15}$$

$$y_c(y,z) = \frac{y_p \cdot CF(z) + (z - zo) \cdot (-0.0002) \cdot Yop}{1000} + \text{Ycorrection} \quad (meters) \tag{16}$$

3.1.4 Additional Experimental Consideration

In addition to achieving proper illumination, exposure, and correcting for zoom effects, spurious reflections from curved surfaces within complicated geometries must be mitigated to avoid erroneous velocity vectors in the data. Laser induced fluorescence (LIF) techniques were used to mitigate this problem by dyeing particles with Rhodamine-B. The particles used in the current study are 3μm diameter polystyrene spheres with a density of 1.05 g/cc. The use of polystyrene allowed for thorough impregnation of Rhodamine-B dye in a heated solvent mixture under reflux conditions. A rotating evaporator was used to extract all solvent from the particle mixture, leaving a dry powder which was a mixture of particles and excess dye not absorbed by the particles. To avoid coloring the test fluid with excess dye, the powder was suspended in de-ionized water and subjected to eight rinse-and-centrifuge cycles to clean the particles.

The resulting particles are excited by 248 – 542 nm light wavelengths and have a peak fluorescence at 568 nm[15]. The large excitation range of Rhodamine-B makes the particles useful for both lasers described here as well as UV laser light at 355nm achieved by adding a third harmonic crystal to the Nd:YAG laser. By placing a band pass filter in front of the camera lens, the laser light is attenuated and only the fluorescing light from the particles reaches the camera sensor. As a result, reflections from walls or any micro-bubbles in the system are filtered out of the images. The fluorescing particles may be seen in figure 22, where the particles are fluorescing yellow/orange light, and the laser light only occupies a very narrow band in the green spectrum.

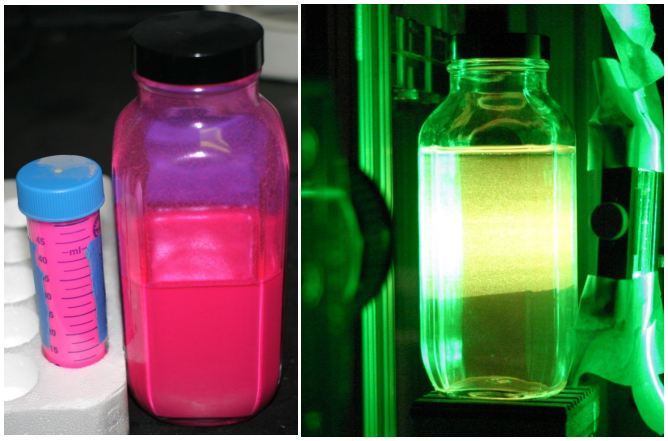

(a) **(b)**

Figure 22 Fluorescent tracer particles(a) prepared for use in PTV and 0.1mL of particle solution suspended in 0.5L H_20 and fluoresced with a 527nm laser (b)

Taking advantage of the fluorescence of the Rhodamine-B, it was decided dye injection tubes should be installed along the straightener plate. In this manner,

fluorescent dye could be injected and a plane of light to only visualize flow in this plane as opposed to a volume of dye as normally done. An image from the series of visualizations using this technique is shown in figure 23, where the SEO is located directly behind the center of the vortex. The dye visualization portion of this study was only part of the initial scoping phase of the experiment to determine PTV measurement locations; however, the small dye injection tubes were left in the straightener plate following the conclusion of this phase of tests.

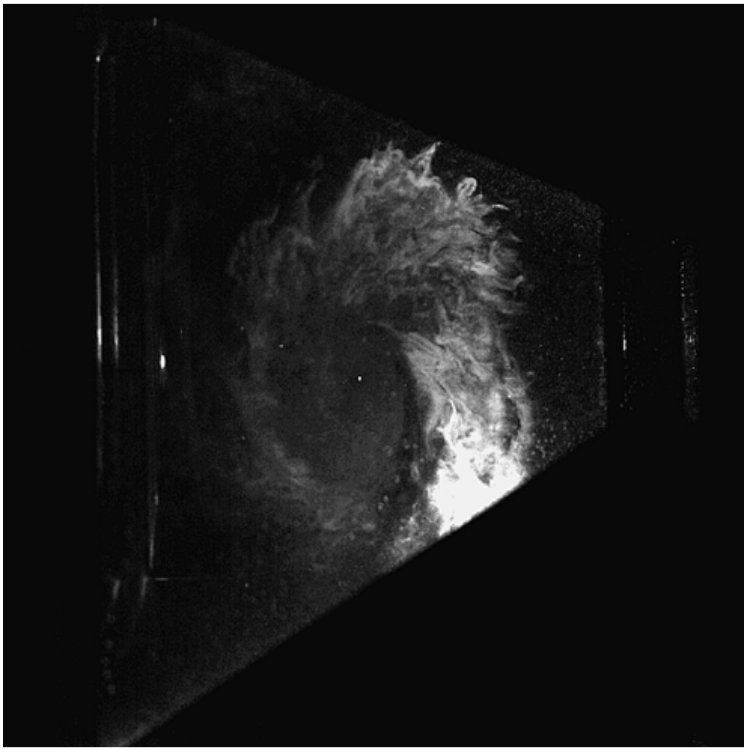

Figure 23 Rhodamine-B dye injection test identifying size and location of primary vortex prior to the SEO.

As part of the search for possible sources of error in the measurements, 1/8" OD nylon dye injection tubes were installed into the straightener plate that extended 2-4"

beyond the plate, but still 15.1" prior to the first pressure tap. At high Reynolds numbers, it was found that these tubes vibrated with specific frequencies depending on their height. To account for these vibrations, a Photron FASTCAM Ultima-ATX high speed CCD camera was set up to take video images of the tubes. Interrogation windows were drawn around the tips of the tubes exhibiting noticeable fluctuations and pixel color metrics were used as a transient signal for Fast Fourier transform (FFT) signal decomposition. Although the intensity of the signal may not be directly correlated to intensity of the presence of the generated fluctuation in the flow, the method provides an account of possible frequency generation sources. At a Reynolds number of 1.83×10^5, the FFT of the main fluctuating injection tube is shown in figure 24 and has a dominant peak at 37 Hz. This tube was located directly in line with the first pressure transducer, but will be shown in the results section to have had no noticeable effect on the measured pressure fluctuations at this location.

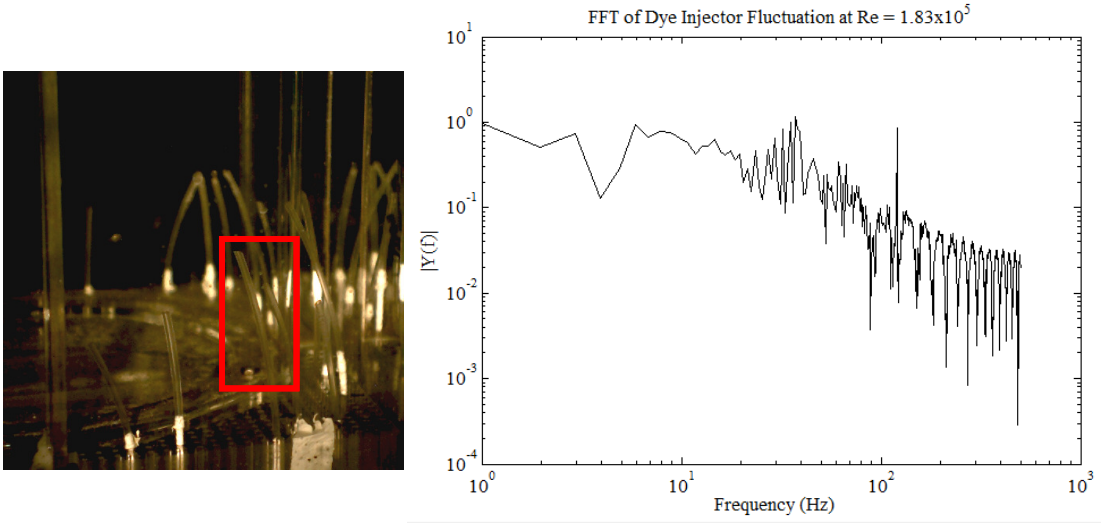

Figure 24 FFT of indicated dye injection tube vibration

3.1.5 GE BWR-6 Side Entry Orifice Results

This section details many of the measurements taken at optimal conditions for the designed experimental setup. Pressure data was acquired over a wider range extending to higher flow rates and at smaller increments throughout the experimental envelope. This was done to ensure the quality of fitted correlation curves. Time averaged velocity and vorticity data at 10 individual planes located just outside the side entry orifice is presented for three Reynolds numbers.

3.1.5.1 Pressure Drop Results and Analysis

This section gives an overview of the findings of the pressure loss coefficient of the side entry orifice, K_{seo}, as a function of Reynolds number. The side entry orifice pressure loss coefficient, K_{seo} (eqn. 17), is a commonly used quantity in system level codes for nuclear plant balance simulations. The definition is often normalized across the system by a characteristic length scale, but in the current calculation, no normalization was performed.

Pressure data had been acquired during two separate test series in the same range of Reynolds numbers but with slightly varying flow rates over the range. The relationship between raw voltage data obtained through the data acquisition process and the final voltage is given by equation 18. The second test was initially done due to new instrumentation at the pump being implemented for frequency analysis, but the second

set of data proved to be a valuable verification set of the initial measurements. The second set of pressure measurements also had measurements at the pump outlet. Tables 8 and 9 detail the specific Reynolds numbers tests and the determined pressure drops associated with each. Additionally, the K_{seo} values are given in the same table.

$$K_{seo} = \Delta P/0.5\rho v^2 \quad (17)$$

$$P(V) = 6*V \text{ (in psi)} \quad (18)$$

The pressure drop across the orifice and K_{seo} as a function of Reynolds number is shown in figure 25 and figure 26 respectively. The power laws for pressure and K_{seo} determined over the given range are described by equations 19 and 20.

$$P(Re)=(7.569*10^{-15})*Re^{2.646}+1.238 \quad (19)$$

$$K_{seo}(Re) = (2.65*10^{8})*Re^{-1.2555} \quad (20)$$

Table 8 First pressure drop measurement data set across the SEO

Test 1 (480 Gallon Tank)				
Flow Rate (gpm)	**Average V in Orifice (m/s)**	**Re**	**Delta P across SEO (psi)**	**K_{seo}**
85	1.794	129031	1.525	106.043
90	1.899	136621	1.567	97.175
95.5	2.015	144970	1.587	87.439
101.5	2.142	154078	1.607	78.383
106	2.237	160909	1.634	73.085
110	2.321	166981	1.671	69.391
115.5	2.437	175330	1.751	65.956
120.75	2.548	183300	1.832	63.127
123	2.595	186716	1.861	61.808
133.5	2.817	202655	2.057	57.997
136	2.870	206450	2.103	57.139

Table 9 Second pressure drop measurement data set across the SEO

Test 2 (500 Gallon Tank)				
Flow Rate (gpm)	**Average V in Orifice (m/s)**	**Re**	**Delta P across SEO (psi)**	**K_{seo}**
91	1.920	138139	1.577	95.670
100	2.110	151801	1.636	82.209
107.5	2.268	163186	1.736	75.460
114	2.405	173053	1.812	70.050
120	2.532	182162	1.903	66.410
125	2.638	189752	2.006	64.502
130	2.743	197342	2.072	61.590
133.5	2.817	202655	2.126	59.933

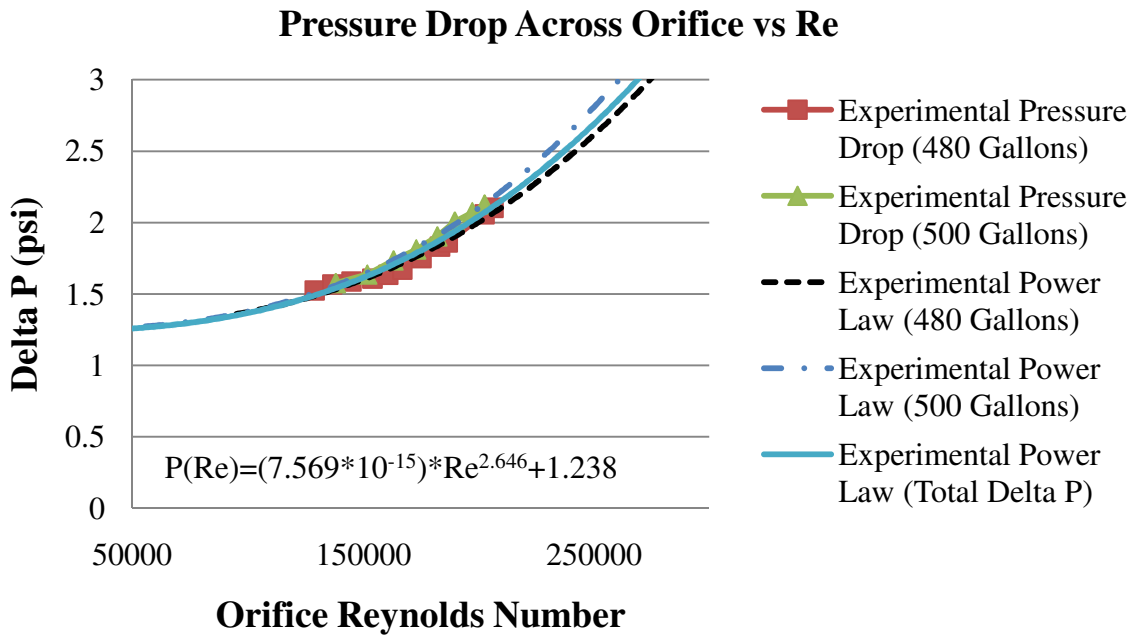

Figure 25 Pressure drops versus Reynolds number for tests 1 and 2

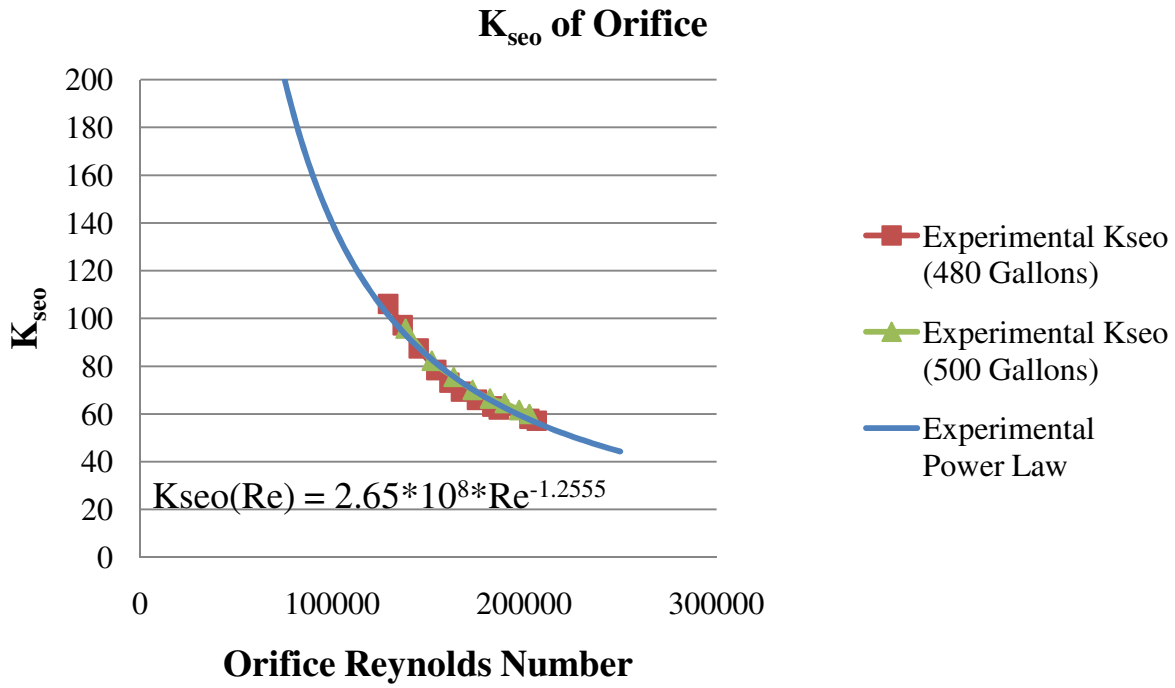

Figure 26 K_{seo} versus Reynolds number for tests 1 and 2

In addition to pressure drop correlation, fast Fourier transforms (FFT) and power spectral density (PSD) plots were used to determine dominant frequencies present in the flow before and after the side entry orifice. While a stagnation tank was designed into the experiment to eliminate spurious pump noise in the signal, measurements were also taken at the pump for comparison. Baseline readings under zero pressure shown in figure 27 were obtained to subtract out instrument noise from the other signals. The PSD of the signal generated just after the pump was also recorded to ensure spurious frequencies measured across the orifice were not due to the pumping frequency. The plot, figure 28, indicates high frequencies were produced by the pump, but were attenuated in the stagnation tank as indicated by the PSD before the orifice in figure 29.

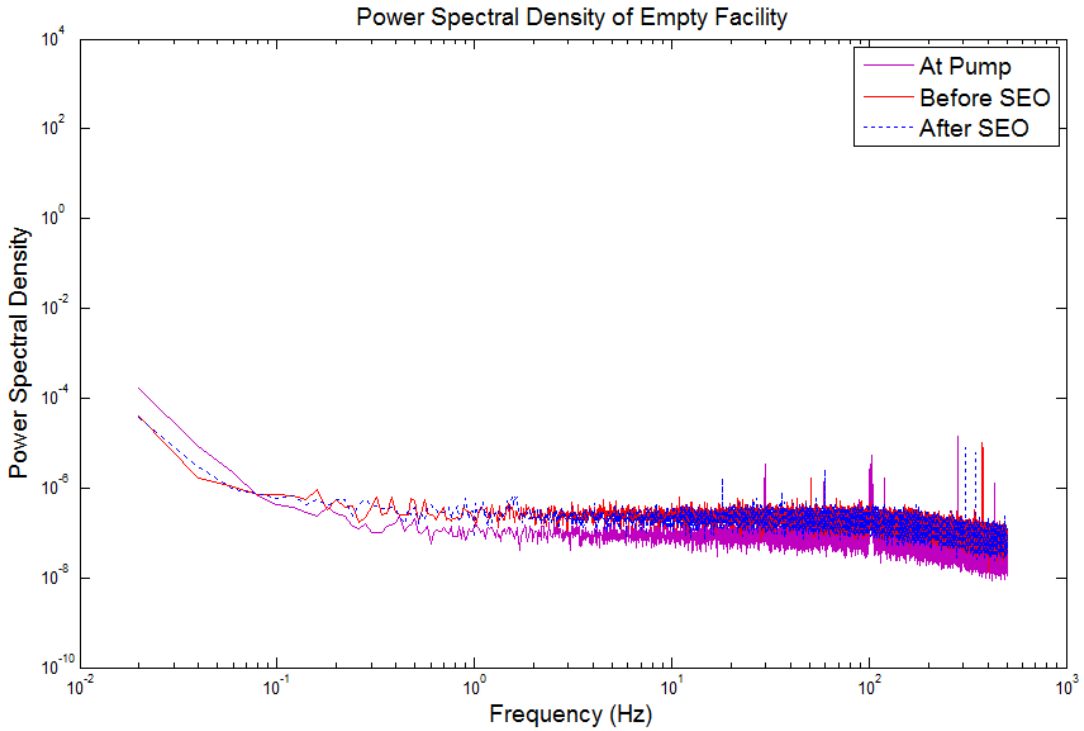

Figure 27 Power spectral density of pressure measurements of empty facility to obtain baseline measurements

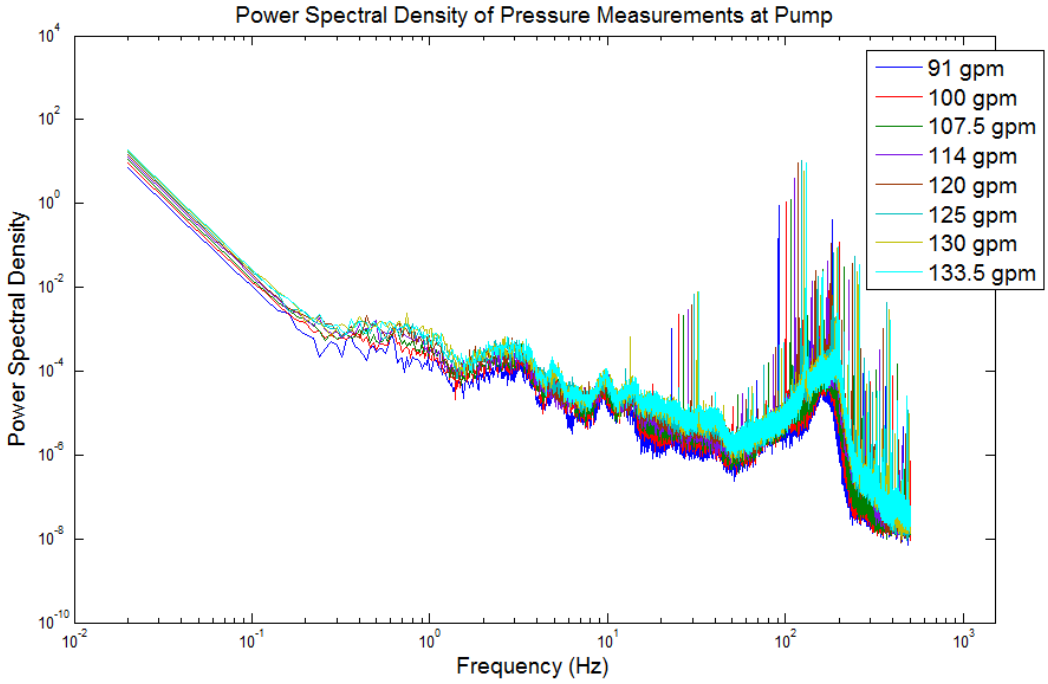

Figure 28 PSD of pressure measurements in test 2 at the pump outlet

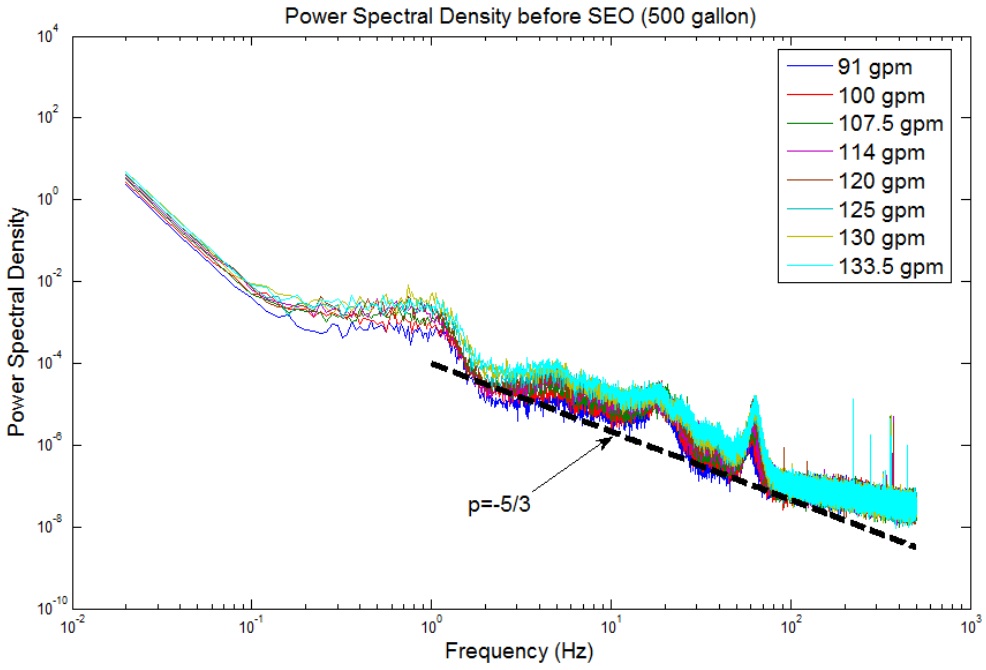

Figure 29 PSD of pressure measurements in test 2 before the SEO

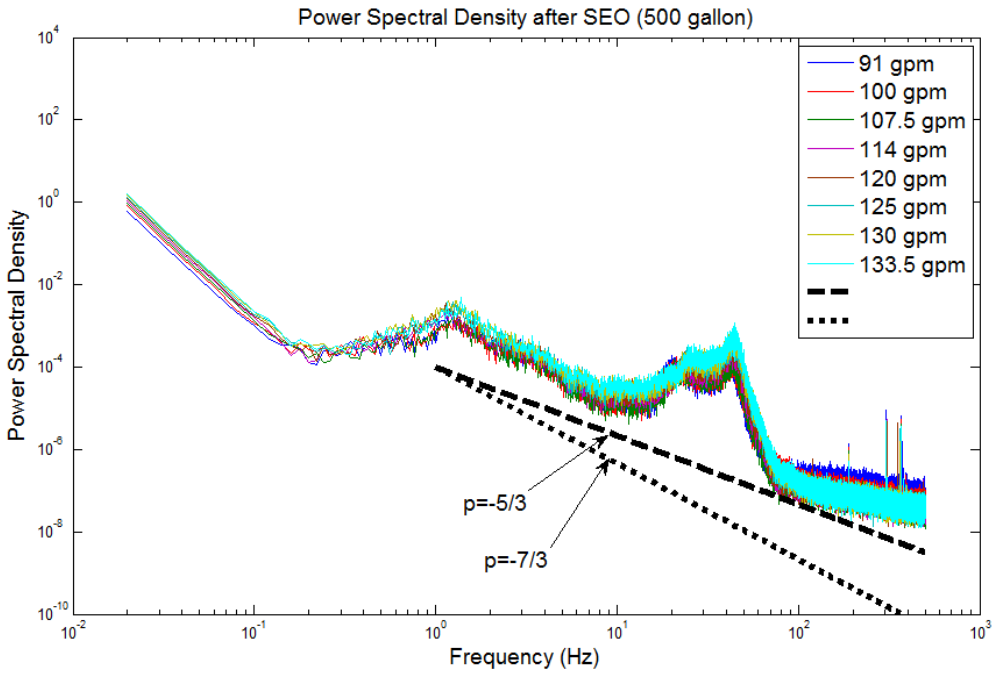

Figure 30 PSD of pressure measurements in test 2 after the SEO

The PSD of this signal following the SEO, figure 30, shows a large generation of frequencies between 5 Hz and 60 Hz. By taking the same pressure signals before and after the SEO and applying the 1D wavelet transform to it, it is very easy to see frequency concentrations in these frequency bands. For identification of frequency concentrations present over the entire length of the signal, visualizing a larger time range enhances the presence of distinct bands of higher correlation coefficients. In the case of the signal prior to the SEO, the wavelet coefficient plot in figure 31 shows a very faint but distinct frequency band around 60 Hz. This same frequency was identified by the power spectra of the same signal in figure 29. The same plot of the decomposition of the signal after the SEO clearly shows large scale generation of frequencies across the decomposed spectrum below 60 Hz.

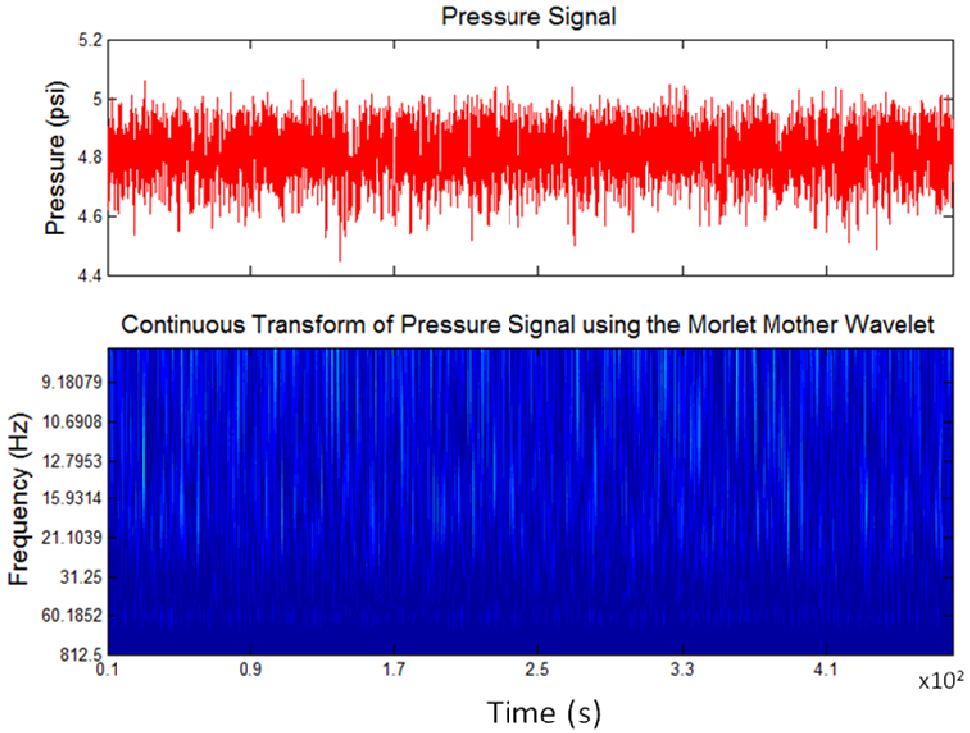

Figure 31 1D Wavelet transform before the SEO for Re=2.06E5

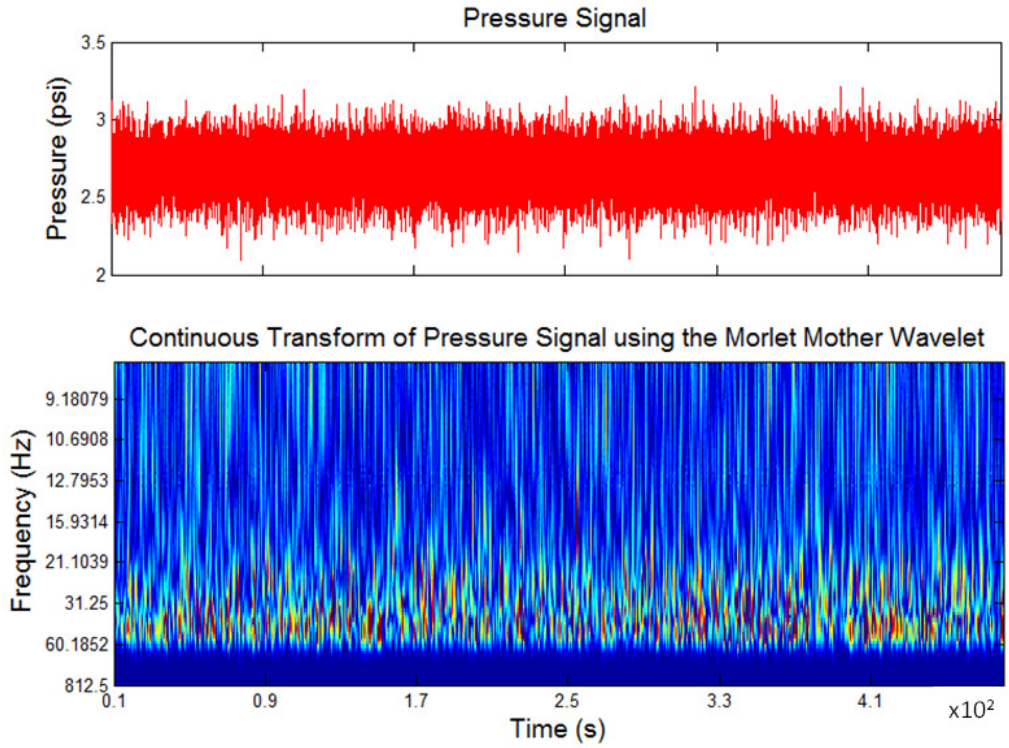

Figure 32 1D Wavelet transform after the SEO for Re=2.06E5

Although useful, the representation on this time scale provides about the same level of information as the PSD. To better understand the interplay between the signals, both are reduced to a time scale over which individual frequency peaks and troughs can be identified. The coefficient plots in figure 33 and figure 34 show a one second section mid-way though the acquisition of both signals. Although the section shown is just one second, care was taken to perform the decomposition on a large time range to avoid any spurious decomposition result at the start and end of the coefficient plots due to the finiteness of the signal. This effect is not covered directly in this work, but additional information regarding it may be found in any standard wavelet text.

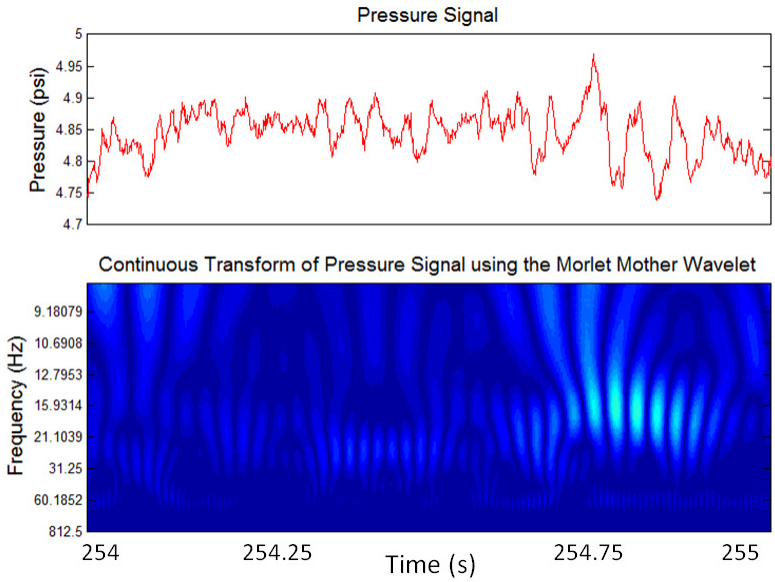

Figure 33 Zoom of 1D Wavelet transform before the SEO for Re=2.06E5

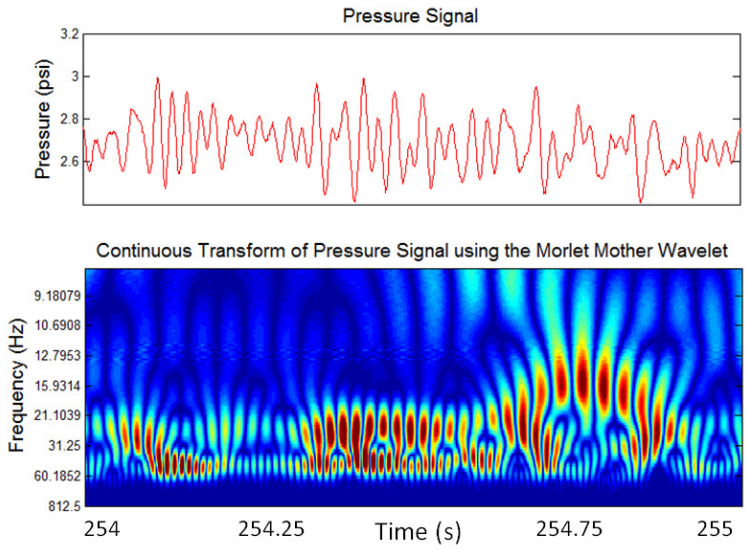

Figure 34 Zoom of 1D Wavelet transform after the SEO for Re=2.06E5

The semblance plot between the two signals has been determined over an equally large time range for the two coefficient plots, but also over a larger frequency range extending into very low large scale frequencies present in the flow. The wavelet plots shown with the semblance plot has a contour range that identifies peaks and troughs of the signal. Visually, this allows for easier interpretation of the information the semblance coefficient is providing. As may be clearly seen in figure 35 at frequencies around 2 Hz, the peaks and troughs in the two coefficient plots denoted by orange and blue are nearly perfectly in phase with one another. The semblance plot in this figure illustrates this point very clearly with high levels of correlation at this frequency.

At the higher frequency ranges shown in figure 36, particularly around t=254.8s, shows a very uniform zebra stripe pattern at a frequency around 16 Hz. This even pattern between correlated and uncorrelated coefficients is representative of a frequency that is correlated, but has undergone a phase shift of 90 degrees.

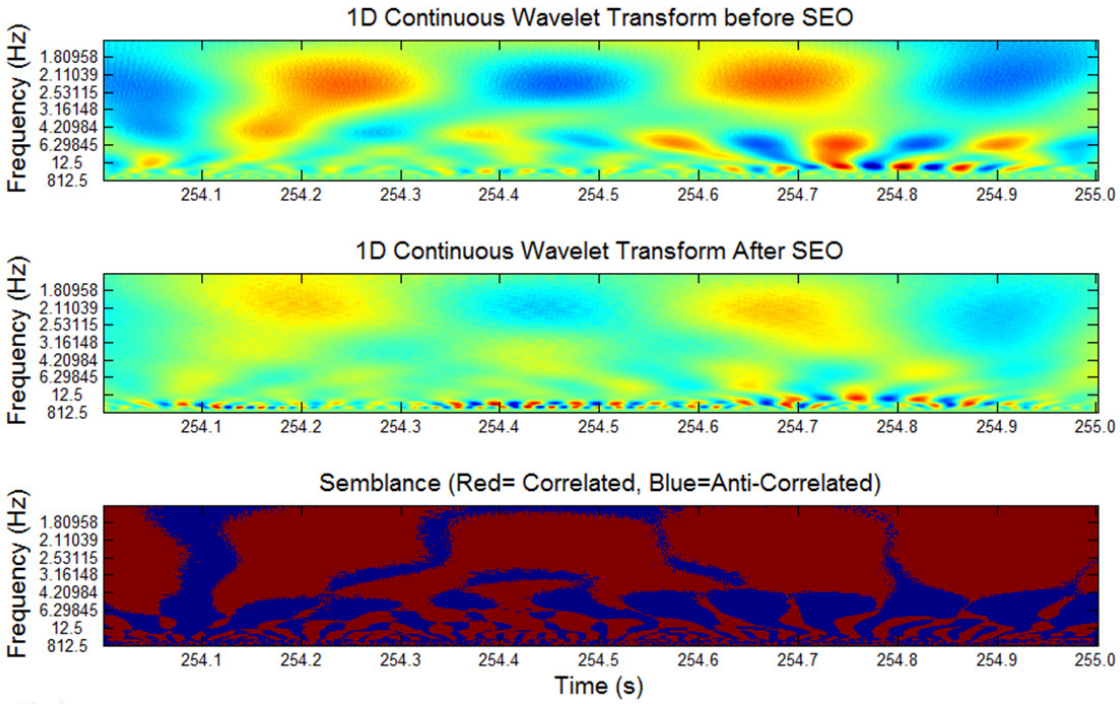

Figure 35 1D Wavelet transform semblance plot of low frequency pressure signals before and after the SEO for Re=2.06E5

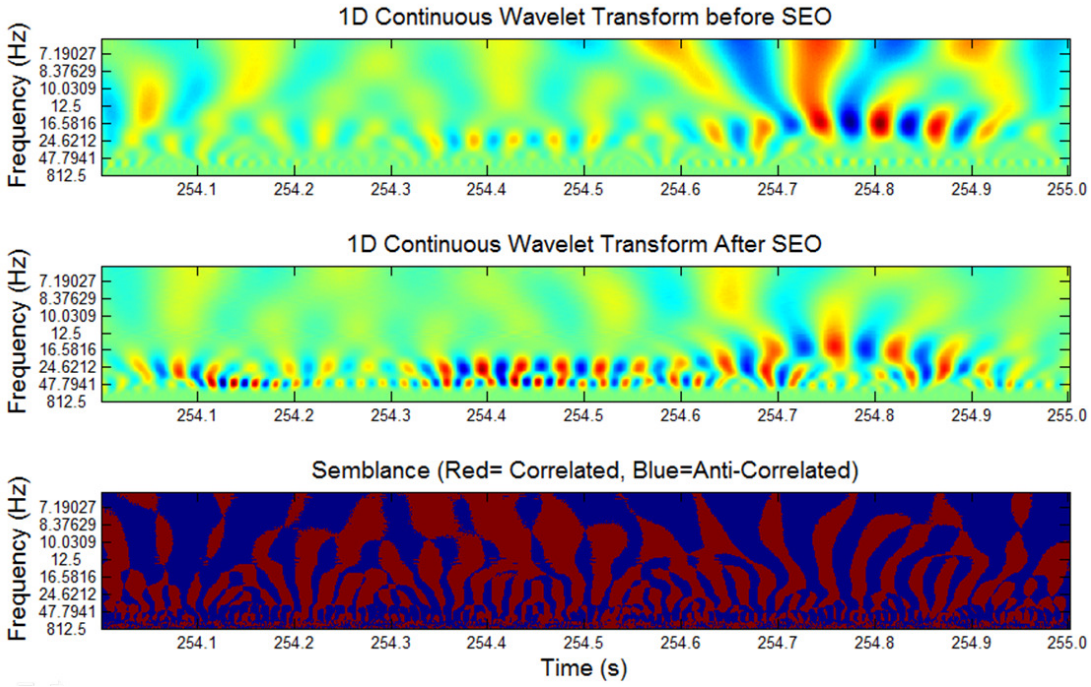

Figure 36 1D Wavelet transform semblance plot of high frequency pressure signals before and after the SEO for Re=2.06E5

By taking the average of the correlation coefficients across time at each frequency and plotting the average versus frequency as shown in figure 37, some high level information about certain frequency correlation may be obtained. Due to the binary nature of the semblance coefficient either indicating whether the signals are correlated or anti-correlated, the averages can be difficult to discern meaning from with the exception of when averages are near either of the extremes (1 or -1). For this reason, it is suggested that this averaging method is useful for drawing conclusions only for extremes in the signal correlation as is seen around frequencies of 7.5Hz in the anti-correlated regime, and below 5 Hz in the correlated regime.

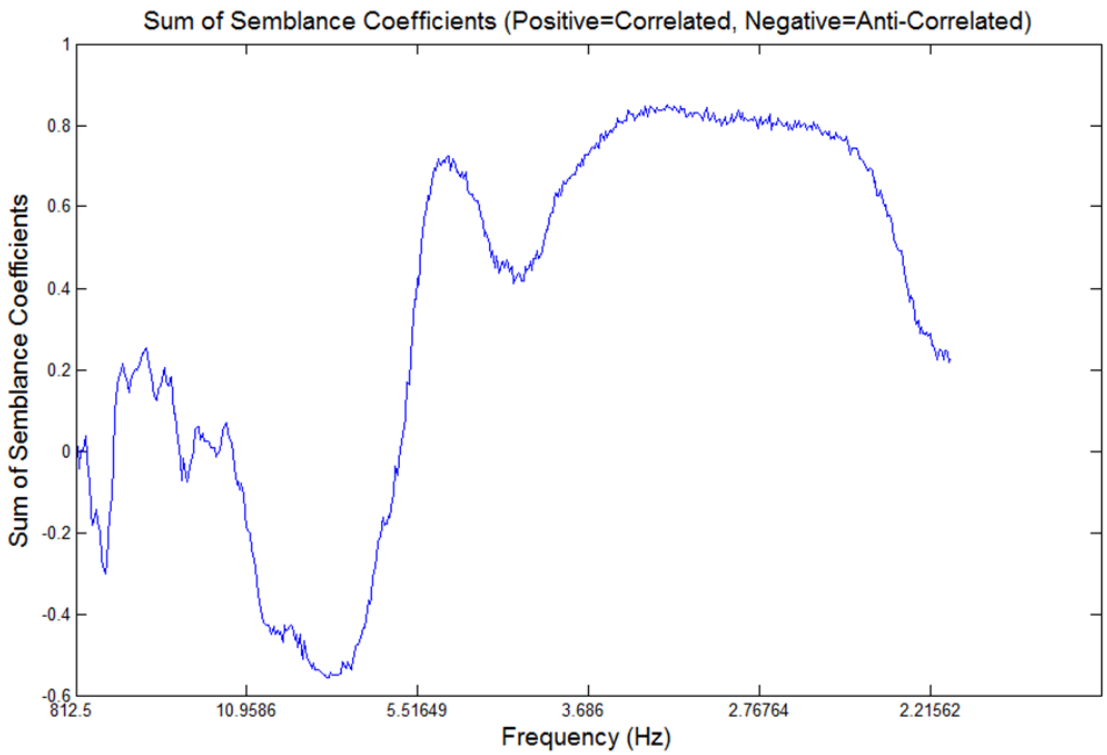

Figure 37 Sum of semblance coefficients denoting correlation between signals at different frequencies.

3.1.5.2 Pressure Measurement Uncertainty

As mentioned previously, the pressure transducers used are accurate to ±0.2 psig, and factory calibrations were verified using a water column to check low pressure readings in the pressure range of this study. In addition to checking that the pressure drop measurements across the orifice were sensible, probability density functions were extracted from the data over the range of flow rates measured to ensure the fidelity of the pressure measurements and the calibration of the transducers. Measurements performed in preliminary tests showed that evidence of faulty measurements or calibration could be detected in this fashion by looking for very clear logarithmic trending in the peaks of the PDF with respect to measured pressure. An example is shown in figure 38 and figure 39 of pressure measurement distributions deemed acceptable because of the near uniform distribution shape across the measured pressure ranges without double peaking or peak trending. When tank volume was insufficient, pressure measurements neared the lower limits of the transducers and calibration sensitivities caused error to increase. Increasing the tank volume and cross checking the measurements with the histograms provided a quick method for scrutinizing the data.

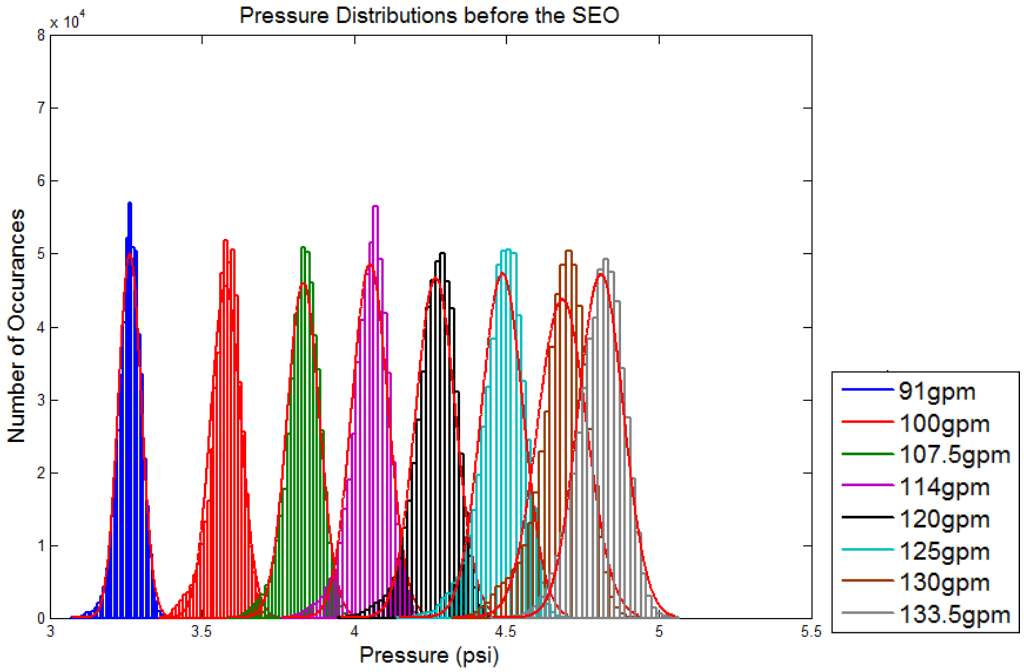

Figure 38 PDFs of pressure measurements taken before the SEO at different flow rates for test set 2

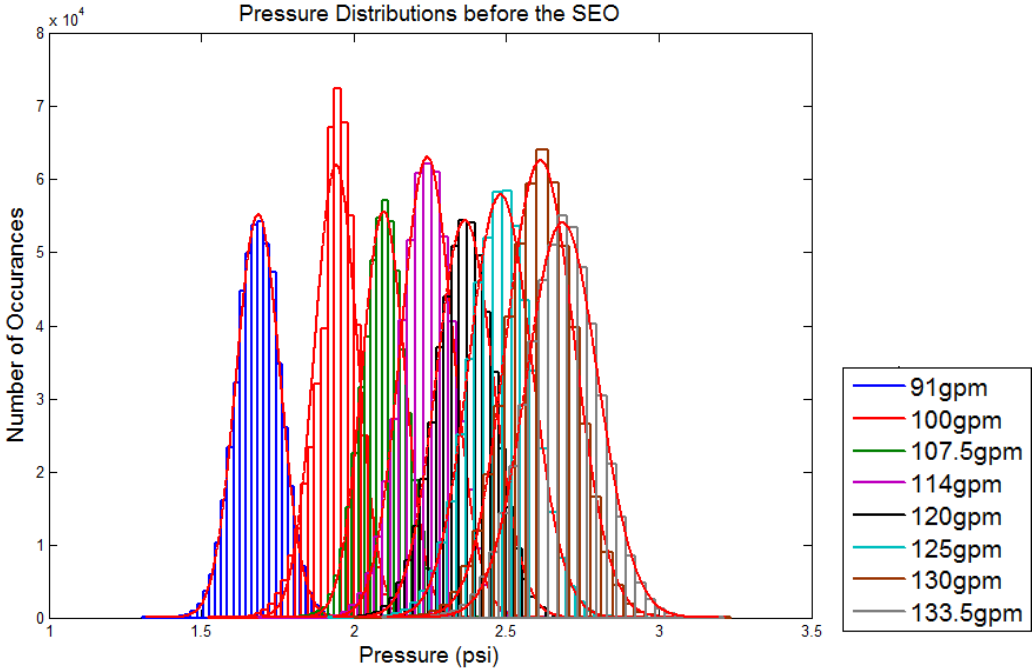

Figure 39 PDFs of pressure measurements taken after the SEO at different flow rates for test set 2

3.1.6 Side Entry Orifice Velocity PTV Study

3.1.6.1 Results and Analysis

Although many different flow rates were used for development of the pressure drop correlations, the volume of video data produced when performing PTV prohibits so many cases to be run. Despite this limitation, three Reynolds number cases were run with 10 planes of data acquired for each. The Reynolds numbers for which PTV data was taken and processed into validation datasets were 1.5E5 and 1.83E5.

The reconstructed velocity fields for the flows just prior to the side entry orifice show strong swirling characteristics. By observation while running the experiment, it was seen that there was some degree of large time scale chaotic switching in the swirl direction, or the core location, but due to the large time scale and the limitation of the data acquisition methods, such switching was not able to be studied in more detail. It should be noted from observation that this switching phenomenon could not readily be predicted or be characterized by a frequency. In most cases, the flow patterns switched, and stayed for a few brief moments before shifting back to the primary flow structure. Care was taken to ensure the flow pattern remained in the same pattern regime throughout data acquisition of each plane in the following cases.

The y-velocity component of the Re=1.5E5 case is shown in figure 40 with streamlines indicating the size and location of the primary vortex. The secondary feature near the top corner at position (0.15m, 0.025m, 0m) comes as a result of the flow

impinging on the core plate located at a position of y=0m. In the actual reactor, the presence of the secondary flows may not be as pronounced or present at all due to the flow being unbounded by walls. To investigate this unbounded case, validated CFD methods shown to accurately predict the experimental data acquired in the present study may be applied with periodic boundary conditions to more faithfully represent the unbounded case. To better visualize the flow features, the z-axis has been expanded in figure 41.

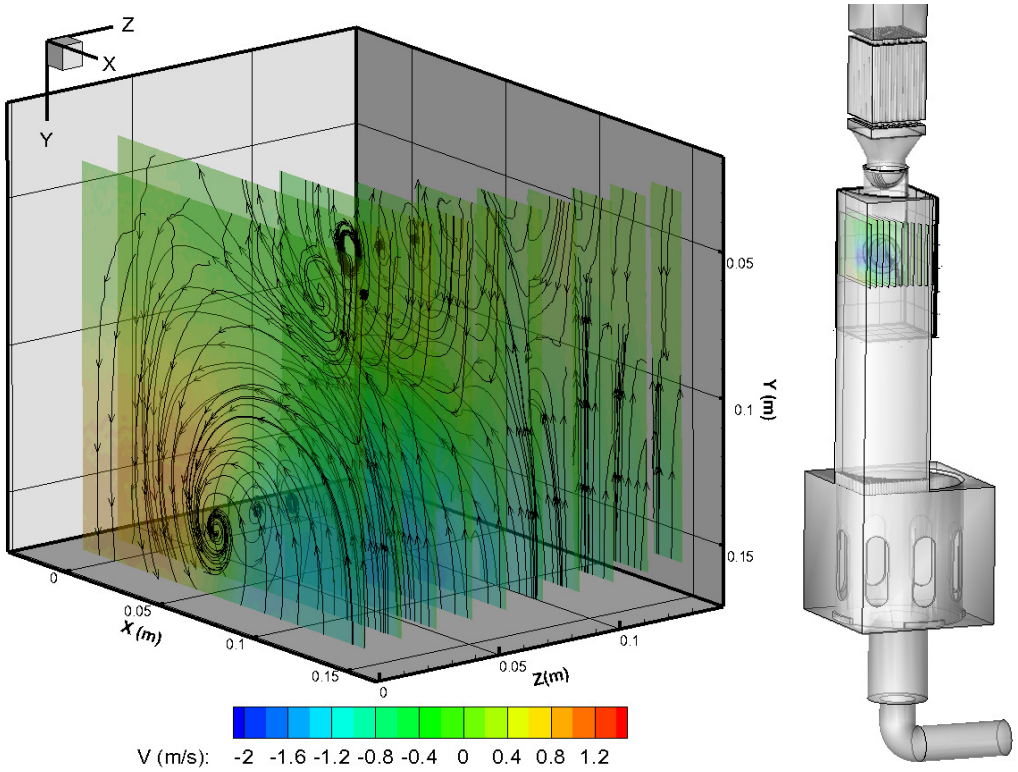

Figure 40 Re=1.5E5 y-velocity component contour map with streamlines showing primary swirl direction and secondary flow locations

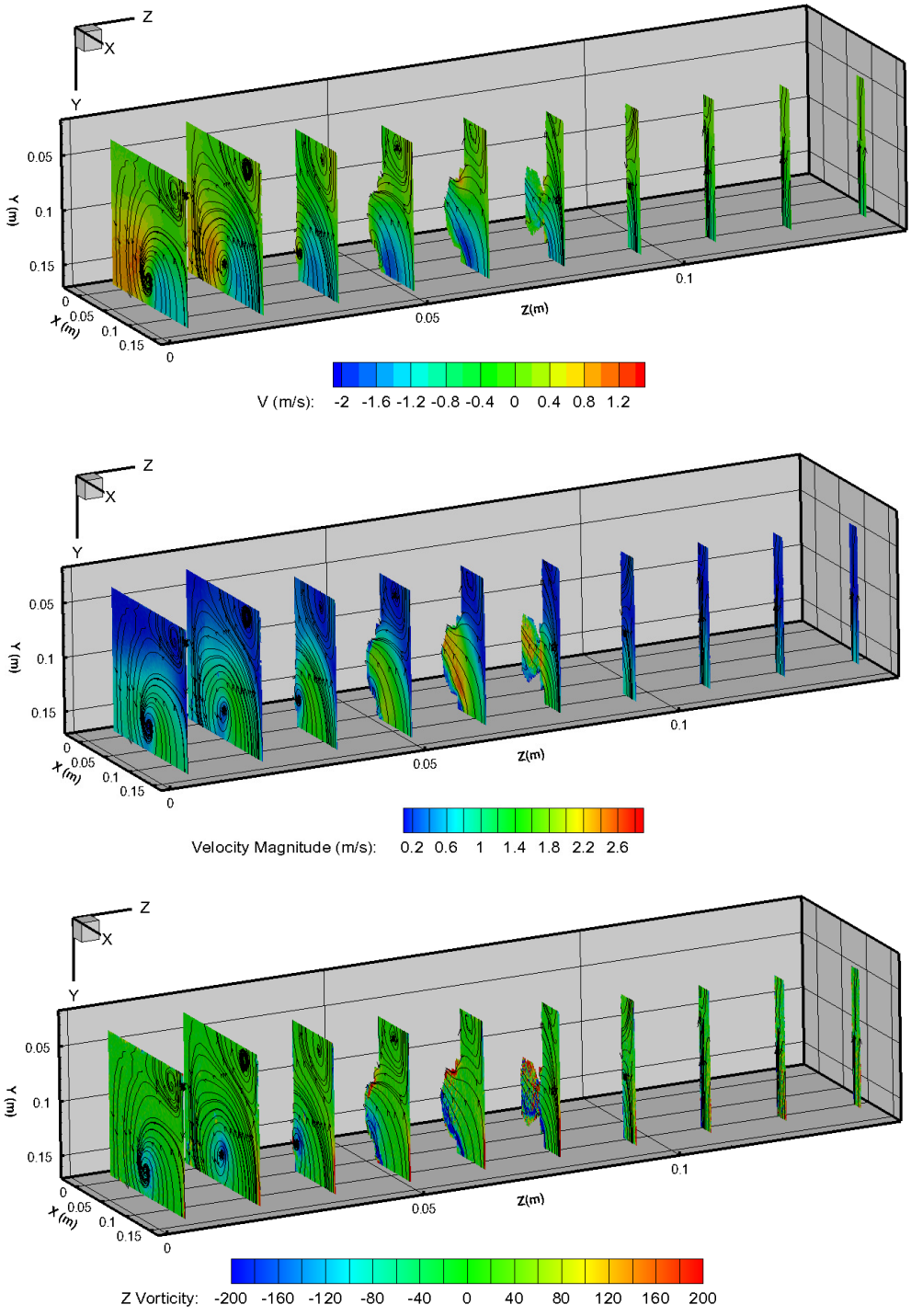

Figure 41 Expanded Re=1.5E5 contour maps with streamlines showing primary swirl direction and secondary flow locations

The primary difference between flow patterns between the lower Reynolds number flow visualized, and the higher Reynolds number visualized in figure 42 and figure 43 is in the secondary vortex present at the top corner. This vortex is present in both flows; however, the vortex extends all the way to the front wall (z=0m) in the Re=1.5E5 case, whereas in the Re=1.83E5 case this vortex begins to take form around z=0.019m and is fully formed by z=0.034m. The reasoning for this difference in behavior is not entirely clear, but it is possible it is due to a higher pressure gradient at the SEO location, pulling the secondary vortex toward the orifice and away from the wall. This is purely conjecture however, and additional tests would be required to confirm this is the responsible phenomenon.

In addition to the primary vortex located at the z=0.0048m plane, a counter rotating vortex was intermittently observed along the x=0.152m plane. While not present at all instances, this vortex was sometimes present as a secondary vortex with a core estimated to be between 2 and 5cm higher than the core of the primary vortex core visualized in figure 40. At other times the vortex along this x-normal plane took the role of the primary vortex. Due to the construction of the single quarter model with a symmetry plane directly through the orifice, it was assumed that this reversed vortex pattern closely mirrors that shown in the measured data presented in this section.

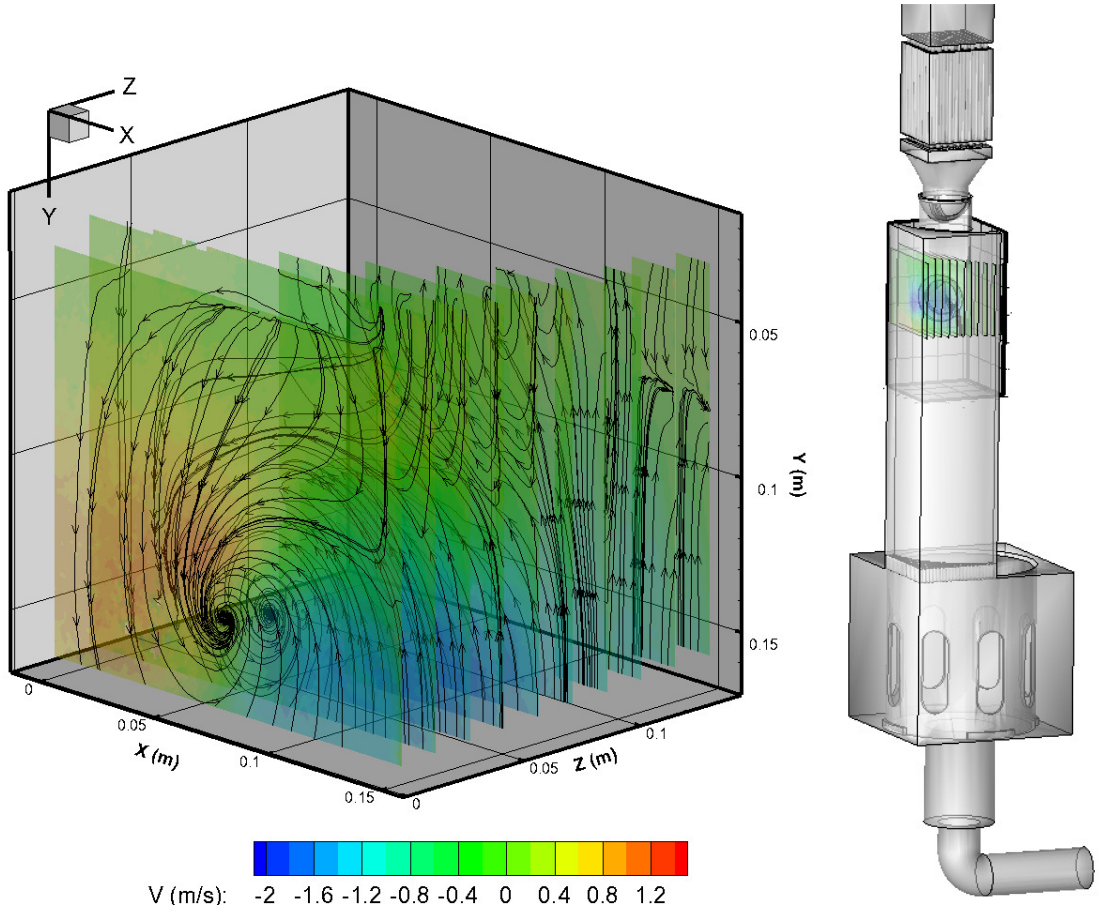

Figure 42 Re=1.83E5 y-velocity component contour map with streamlines showing primary swirl direction and secondary flow locations

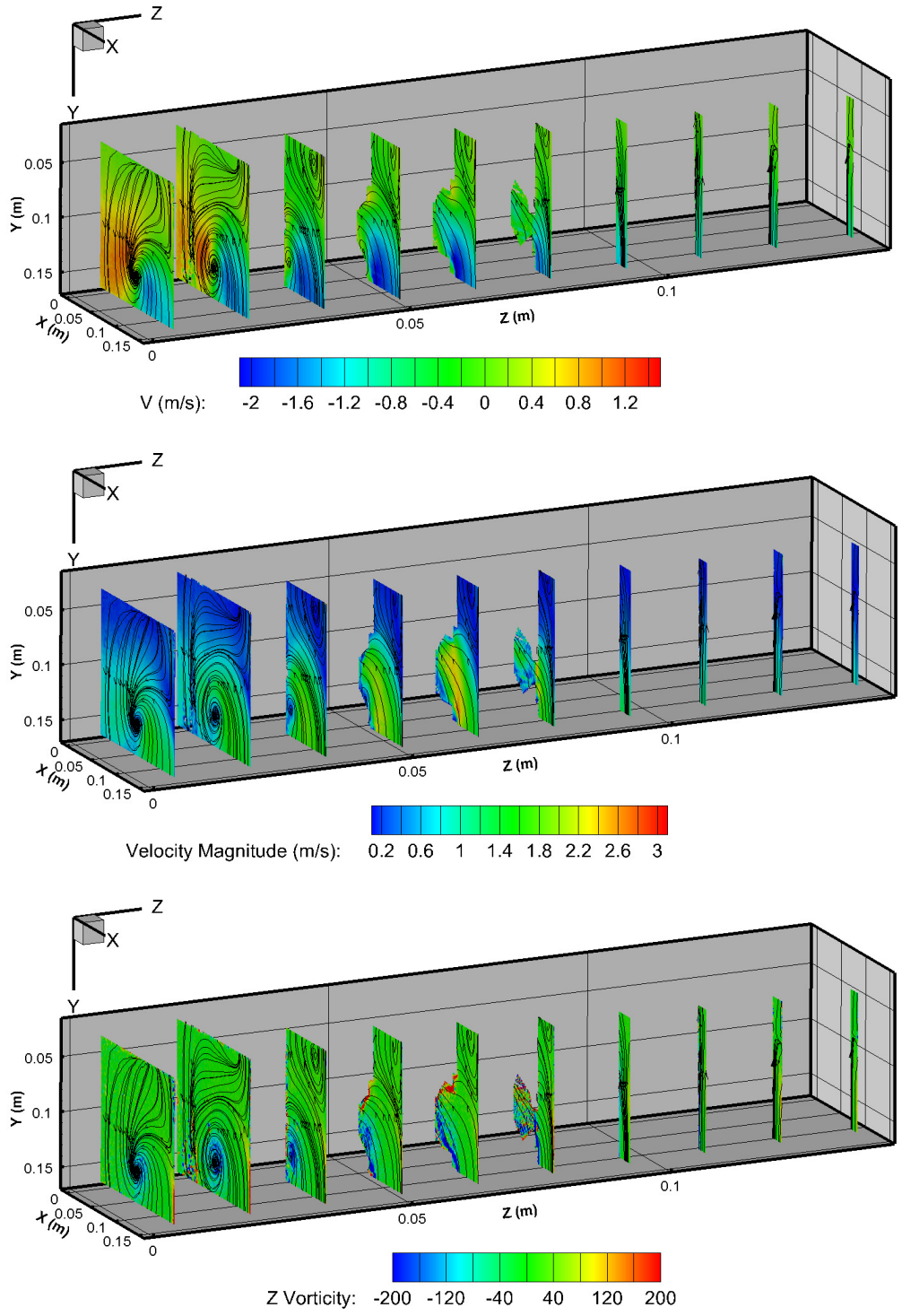

Figure 43 Expanded Re=1.83E5 contour maps with streamlines showing primary swirl direction and secondary flow locations

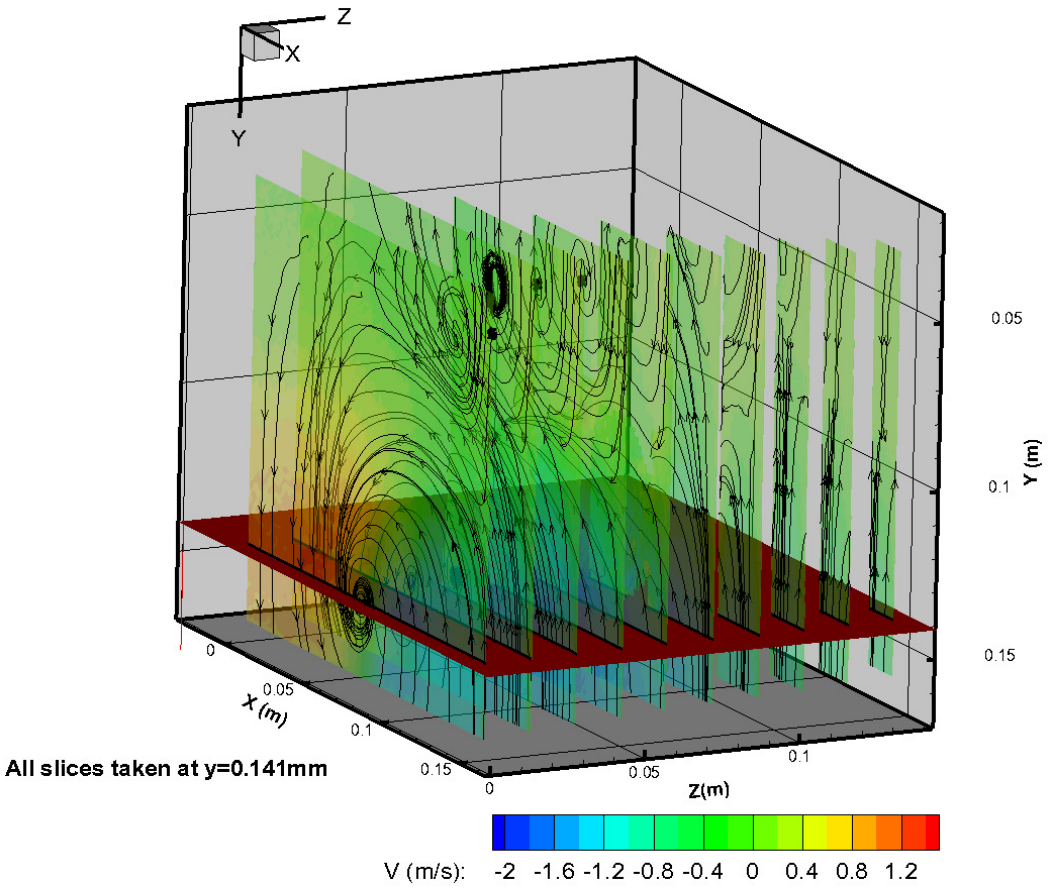

Figure 44 Line probes taken at the intersection of PTV data planes and a y-normal plane at y=0.141m.

To facilitate the comparison of velocity profiles with CFD predictions, a data reduction has been done in the form of line probes taken at the intersection of the data planes and a y-normal plane (figure 44) located at y=0.141m. This y-position corresponds with the vortex core location for the Re=1.5E5 case at the z=0.0048m plane. For consistency, the same y-location was used for the Re=1.83E5 case, despite the vortex core being slightly shifted towards the upper impingement plane. Figure 45 through figure 47 provides line probe data for the Re=1.5E5 case and figure 48 through figure 50 provide the data for the Re=1.83E5 case.

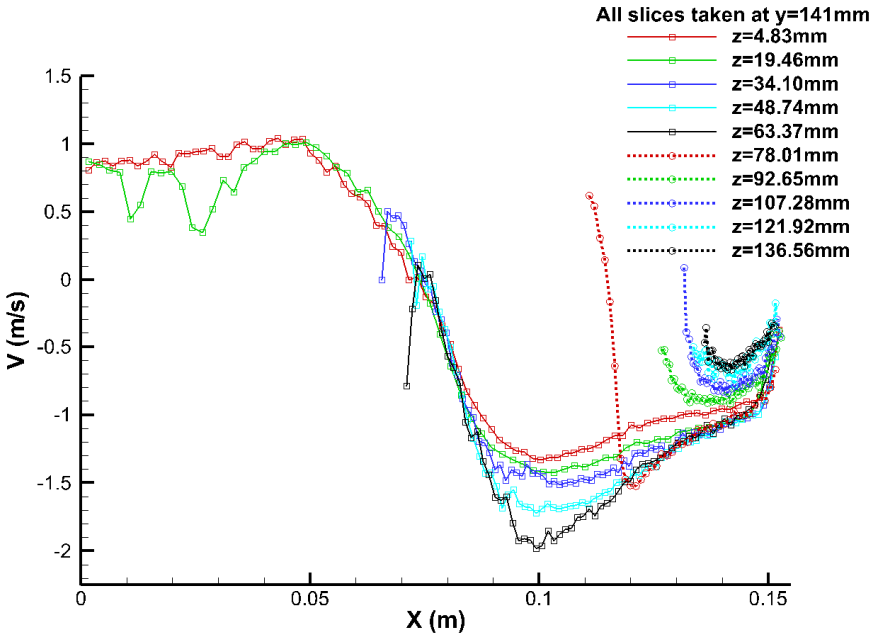

Figure 45 Y-velocity component line probes taken at y=0.141m for the Re=1.5E5 case

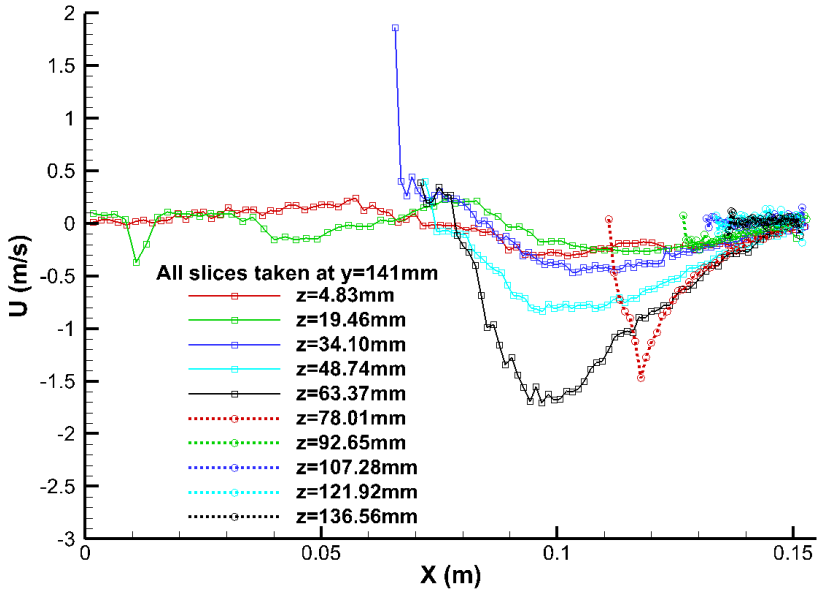

Figure 46 X-velocity component line probes taken at y=0.141m for the Re=1.5E5 case

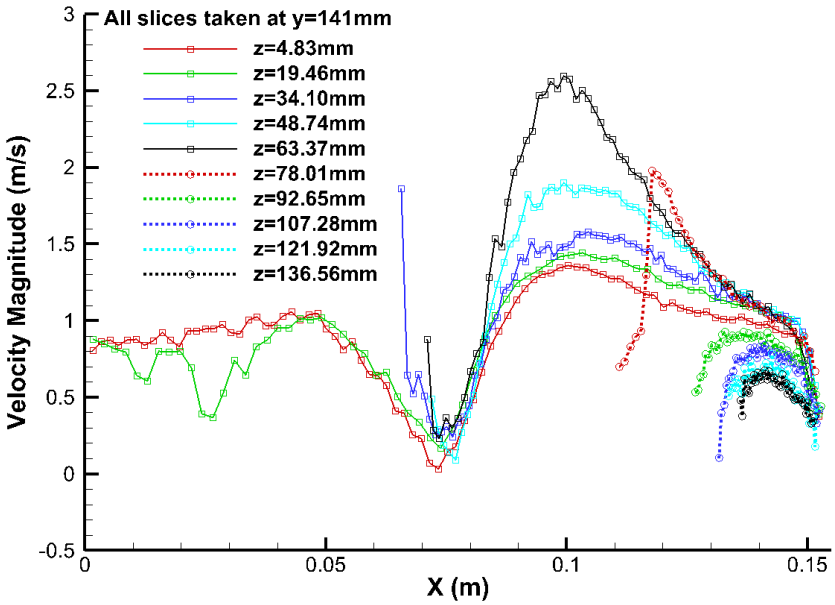

Figure 47 Velocity magnitude line probes taken at y=0.141m for the Re=1.5E5 case

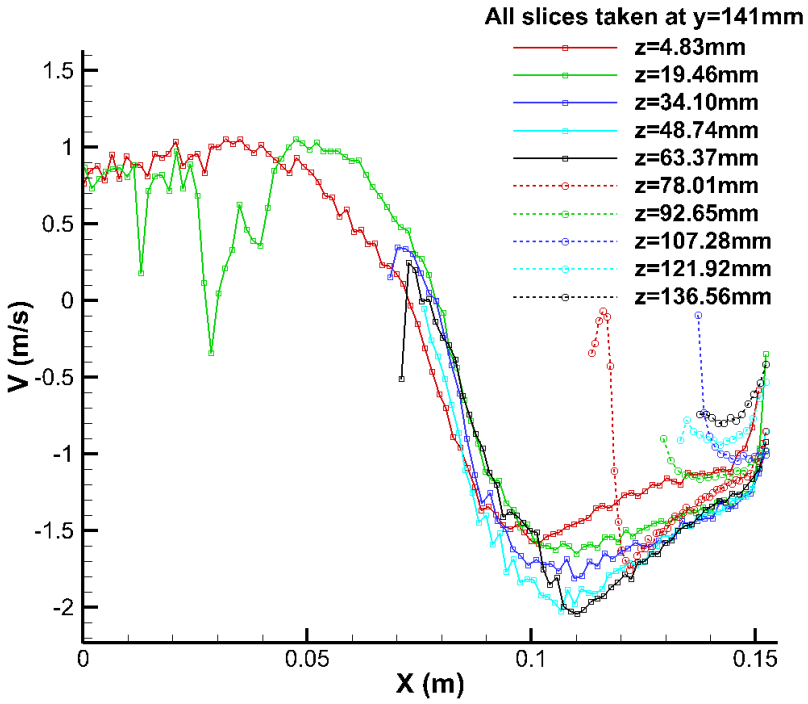

Figure 48 Y-velocity component line probes taken at y=0.141m for the Re=1.83E5 case

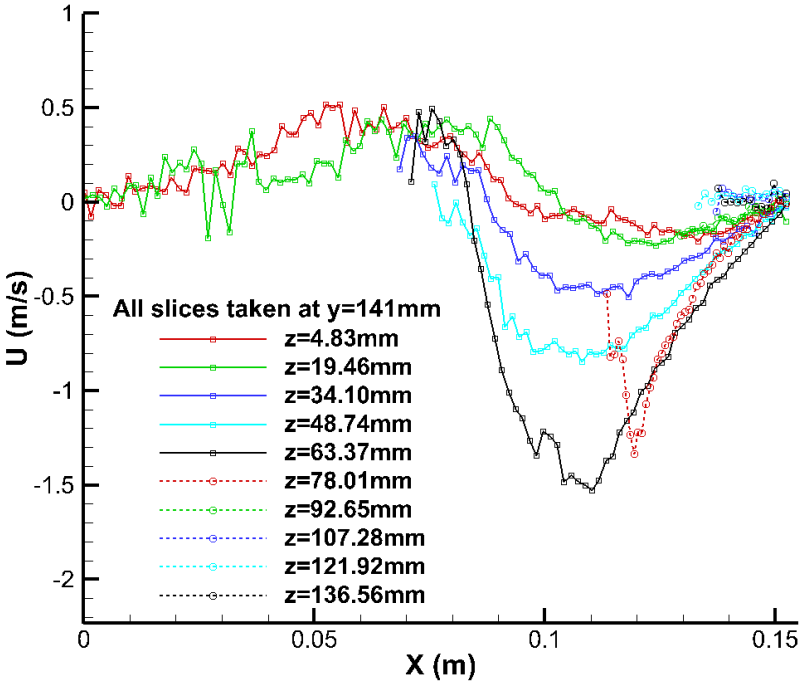

Figure 49 X-velocity component line probes taken at y=0.141m for the Re=1.83E5 case

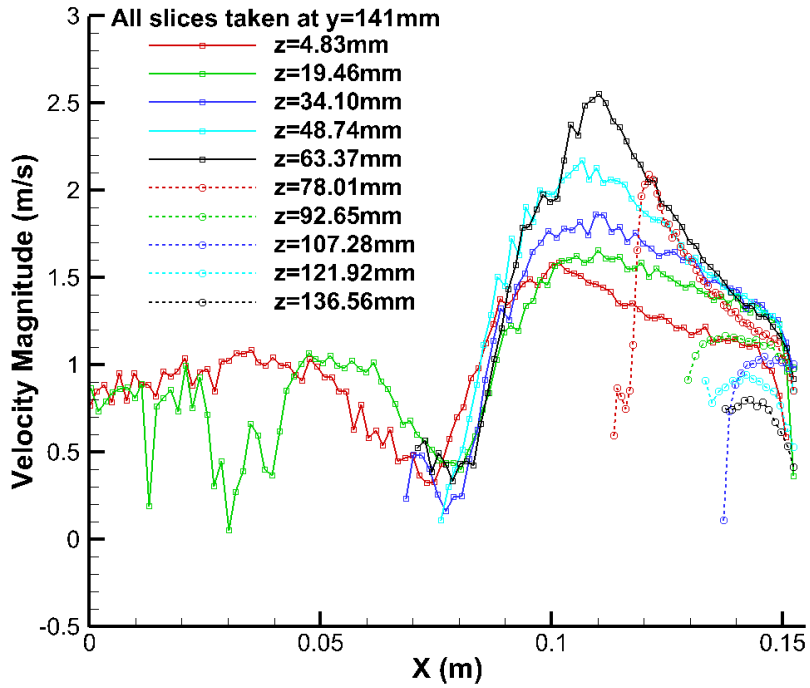

Figure 50 Velocity magnitude line probes taken at y=0.141m for the Re=1.83E5 case

Comparisons between these two cases are shown in figure 51 through figure 53 and show good agreement between the profiles. As expected from conservation principles, the higher Reynolds number case exhibits higher velocity magnitude peaks near the center planes where the orifice is located.

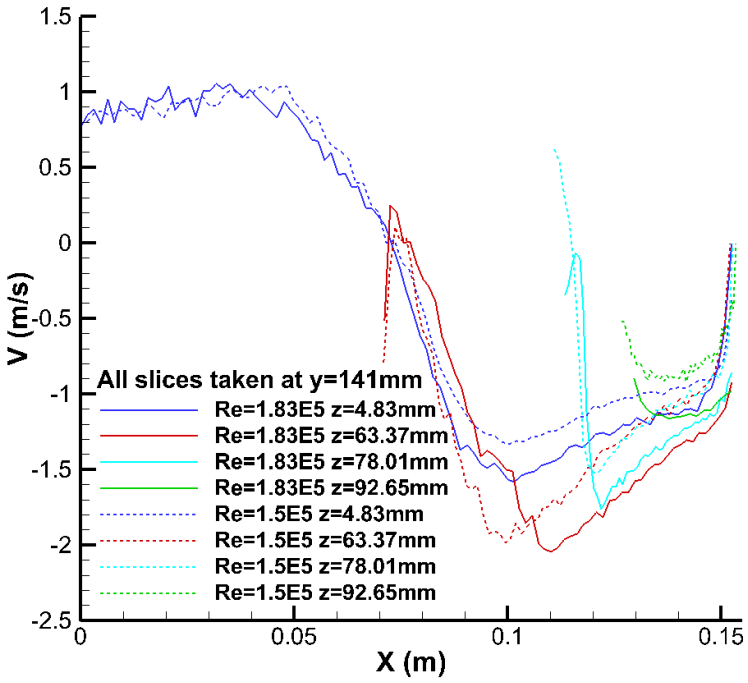

Figure 51 Y-velocity component line-probe comparison between Re=1.83E5 and Re=1.5E5 cases

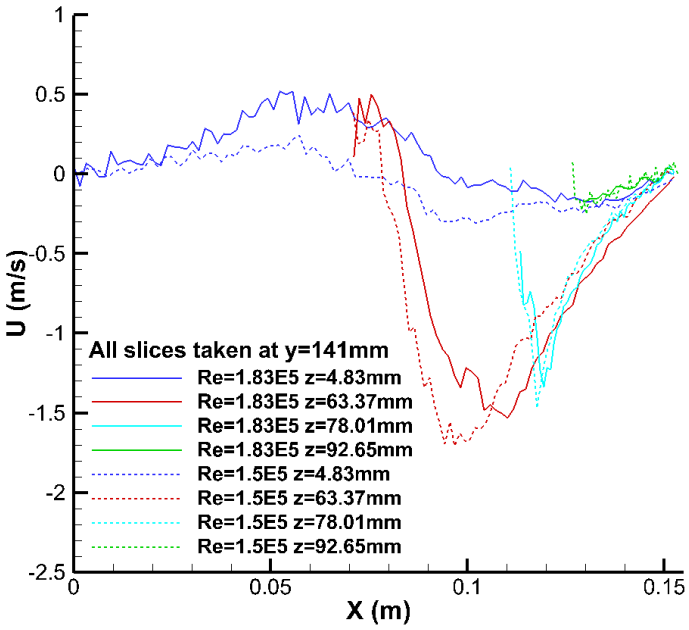

Figure 52 X-velocity component line-probe comparison between Re=1.83E5 and Re=1.5E5 cases

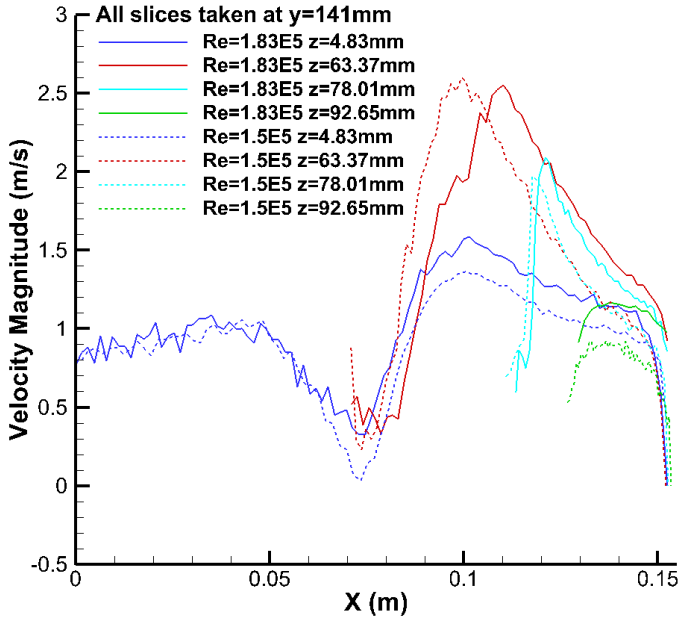

Figure 53 Velocity magnitude line-probe comparison between Re=1.83E5 and Re=1.5E5 cases

3.1.6.2 Uncertainty Analysis of PTV Results and Acquisition Methods

The effect of the chosen time between the straddled pulses is particularly noticeable in regions with large variances in velocities. The average velocity fields shown in figure 42 are taken in the XY plane that intersects the orifice. Highly 3-dimensional flows combined with lower velocities along the upper region of the interrogation zones contribute to the misleading flow fields and significant absence of vectors. At low velocities, the time between subsequent frames must be long enough for the particles to visually move, but short enough so that significant correlation is detected between the frames for a moving particle. For high speed flows the difficulty is in achieving a high enough frame rates such that good correlation can be made between subsequent frames. If the frame rate not high enough, the particles will move from one frame to the next to the extent that reliable correlation cannot be determined and good vectors are unobtainable. In interrogation regions where both high and low speed flows are present (as well as flows highly normal to the laser sheet plane), the potential for bad data increases drastically.

The influence of time steps between PTV images can play a large role in the correlation of tracked particles from one frame to the next. In the present sensitivity study, a central plane intersecting the orifice (figure 54) is investigated at a $Re=1.83x10^5$ with varying straddled Δt at 0.001s, 0.0005s, 0.00033s, and 0.00025s. Results of this study are shown in figure 55. At this Reynolds number, the bulk velocity through the orifice based on mass flow rate is 2.38m/s.

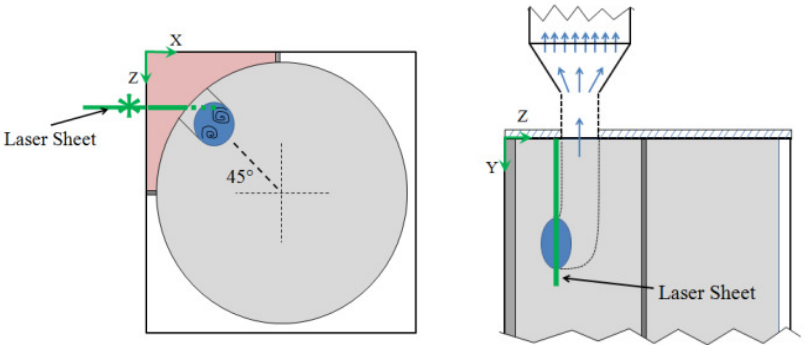

Top view ***Side View***

Figure 54 Laser plane for straddling PTV Δt sensitivity study at z=78.01mm

An average velocity was measured for the Δt=0.00025s case by taking a line probe at the orifice entrance region where the highest measured velocity is located. This line probe spanned approximately 2cm of the entrance region between the points (0.136m,0.051m) and (0.136m, 0.032m) and had an average value of 2.39m/s, which is a 0.42% variation from the average velocity approximated from the flow rate. The velocity vectors in the low velocity regions (y<0.10m) maintain the same relative magnitude, with slight variation in the 0.00033s case. This variation was likely due to a switch of vortex side preference during the measurement. The similarity between the streamlines for the 0.0005s and 0.00025s cases but not in the 0.00033s case in regions outside the take-off orifice suggest a dominant vortex preference, but with a degree of instability. Qualitatively, this instability could be seen in the flow during the conduction of the experiment. A statistical analysis has yet to be performed due to the long timescales of the phenomena as well as the inability to predict the point of vortex switching due to the apparent randomness of the process

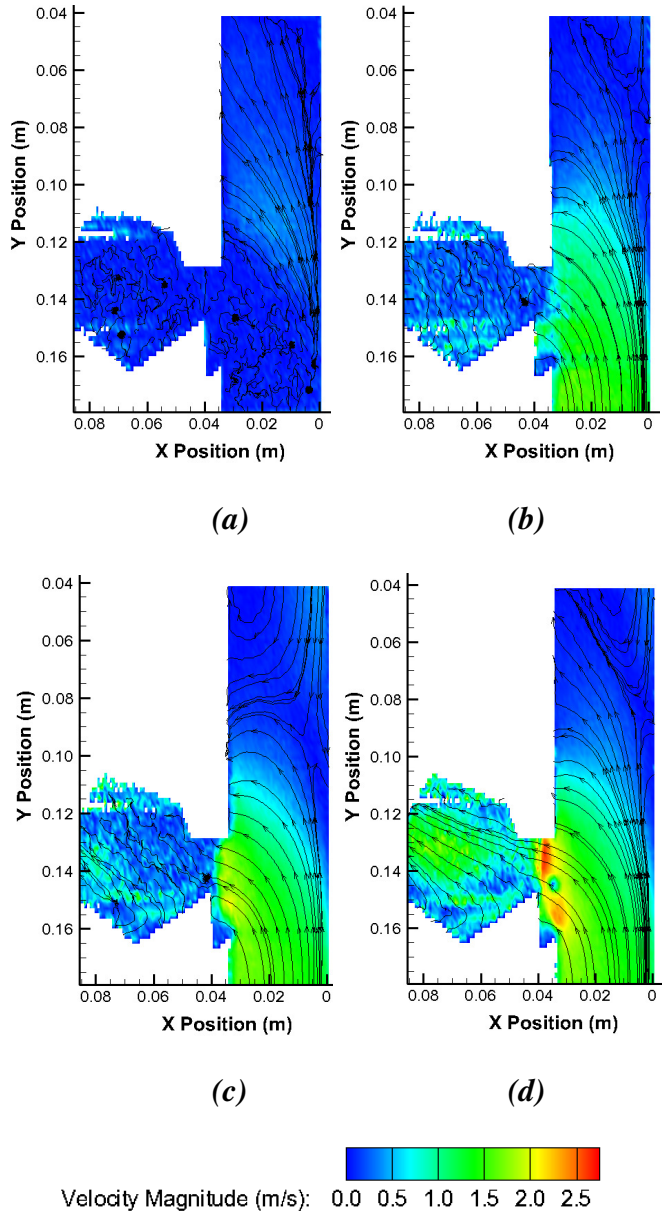

Figure 55 Velocity fields of straddling PTV Δt sensitivity study for times (a) 0.001s, (b) 0.0005s, (c) 0.00033s, and (d) 0.00025s at z=3.0”

The tracking scheme developed at Texas A&M University has undergone extensive error analysis in a variety of conditions and using varying interpolation

methods for achieving sub-pixel accuracy on the velocities[14]. The results of that study indicated that for lower particle density conditions, the maximum total error was approximately ±0.2 pixel/Δt. The location in the current study where this translates into the largest error is along the front plane (z=0m) where the mm/pixel ratio is largest. At this front plane, a ratio of 0.24 mm/pixel translates into a ±0.192 m/s error band assuming a 0.00025 second (4 kHz) gap between straddled laser pulses. It should be noted that the images used for tracking were very clean and free from significant noise, so this should have improved upon the error; however, keeping in accordance with good experimental practices, this is neglected unless otherwise shown to be the case.

In addition to the introduction of error from the tracking methods, error can come from insufficient data in the averaging process. To ensure that the number of vectors fields that were averaged over is sufficient for good statistics on the average field, a parametric study was done of the same image set but with increasing number of image pairs over which the data was averaged. Averaging was done over 10, 100, 500, 1000, and the full 2200 image pairs for the z=19.46mm plane of the Re=1.83E5 case. Each image pair consists of two separate images, each with one of the straddled pulses of laser light. The image pair together forms one set of vectors in the imaging plane. The results shown in figure 56 indicate that the average velocity field begins to stabilize between 500 and 1000 image pairs, and by 2200 image pairs the average deviates from the 1000 pair case by a negligible amount. This averaging study was performed using 8x8 interpolation windows for the vector averaging process.

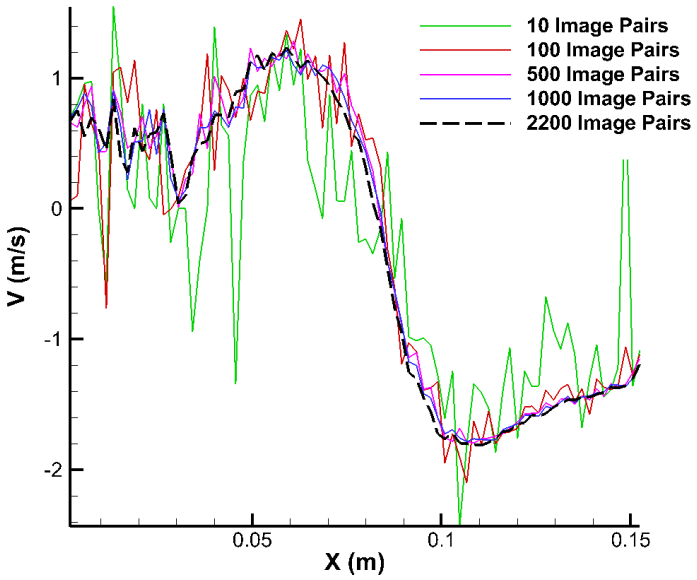

Figure 56 Sensitivity study to the number of image pairs used in averaging process.

Spatial averaging is also a large source of error that must be accounted for in high fidelity PTV analysis. The raw data consists of vectors located in free space without any interpolation onto a presentation grid. When performing data reduction on the instantaneous vectors, they are also placed onto a structured grid and interpolated with their neighboring vectors to obtain a good estimation of the vector at the cell center. This ordered vector field may then be averaged with the next ordered instantaneous vector field. Contour plots for qualitative comparison between averaged velocity fields with different window sizes are shown in figure 57. This plot has been zoomed onto a region with both high and low velocities present in the flow.

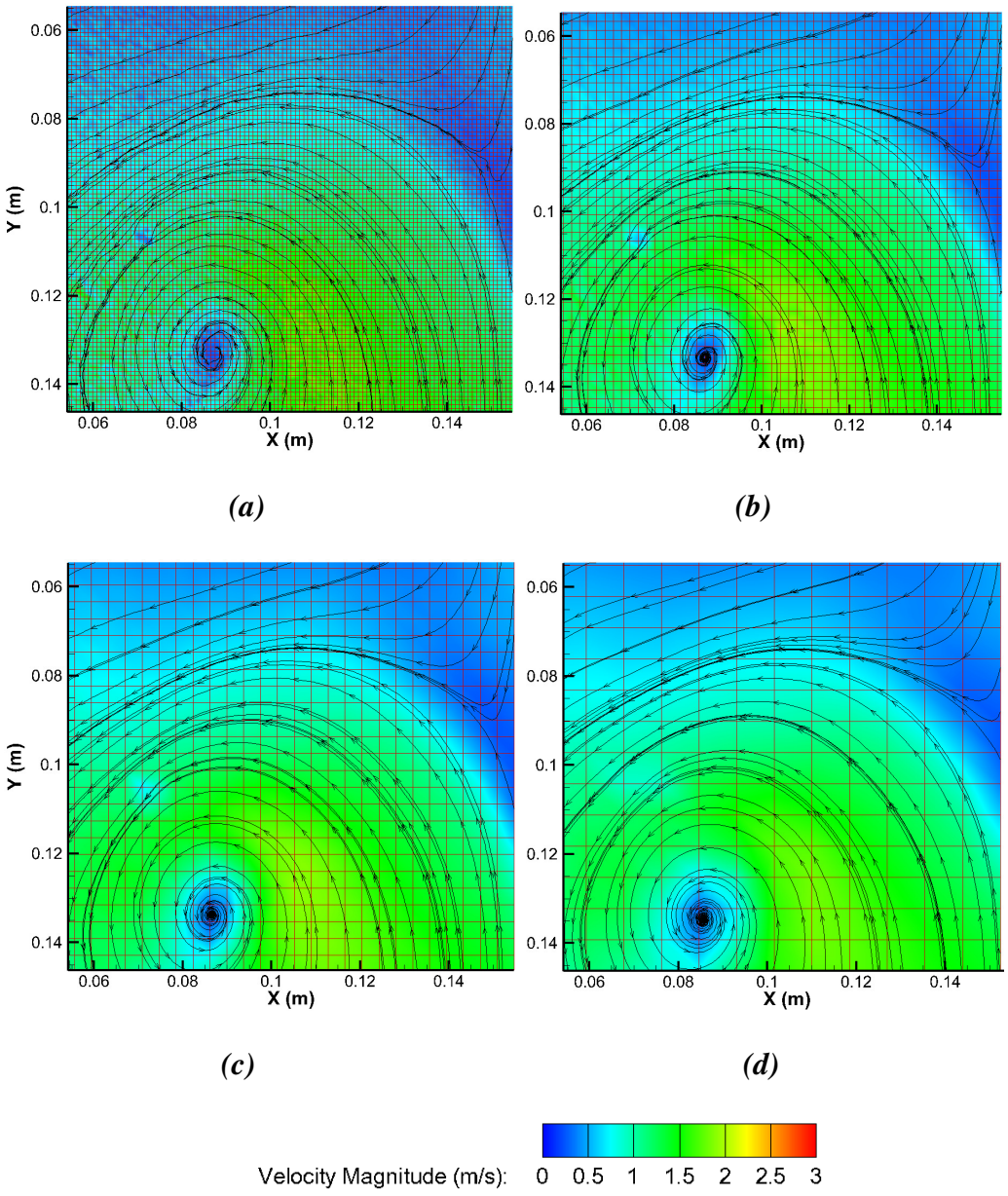

Figure 57 Filter window size for vector averaging. Window sizes of (a) 4x4, (b) 8x8, (c) 16x16, and (c) 32x32 pixels were used.

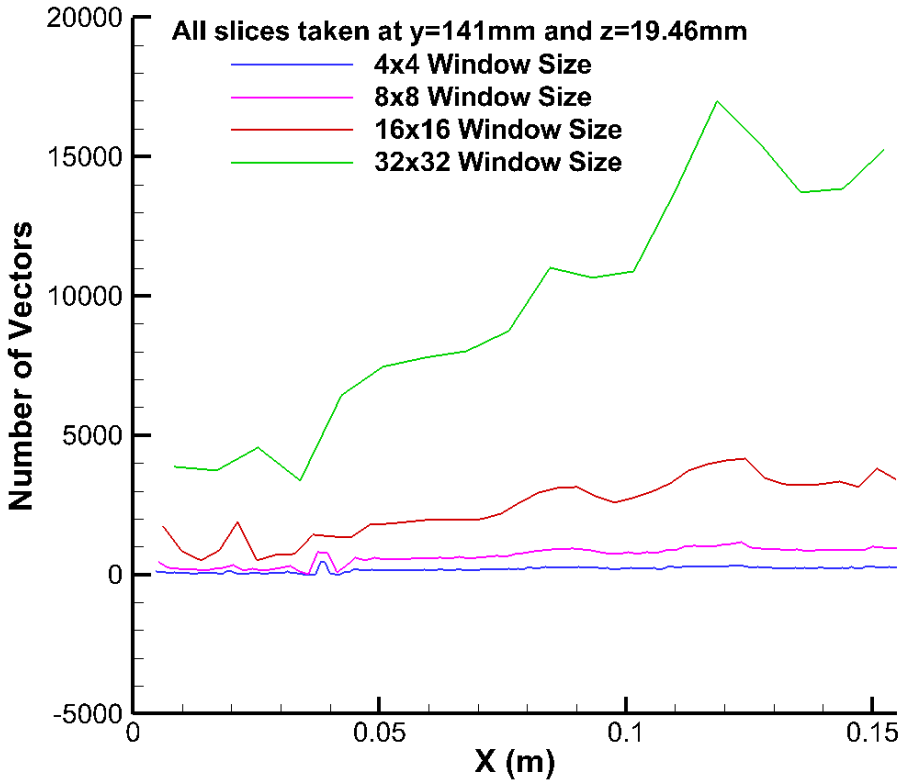

Figure 58 Local number of averaged vectors in a given window.

While it is intuitive that a larger window size means more vectors get averaged into each block (figure 58), the result of a large block can also mean de-featuring of the flow patterns and loss of information in regions of high velocity gradients. To check for de-featuring and other filter based errors, line probes taken across the channel but using different window sizes. The results of these line probes shown in figure 59 through figure 61 illustrate the drastic impact of the filtering window size on the data. The 8x8 pixel interpolation window for the averaging process provided the best balance between spatial accuracy and reduced noise.

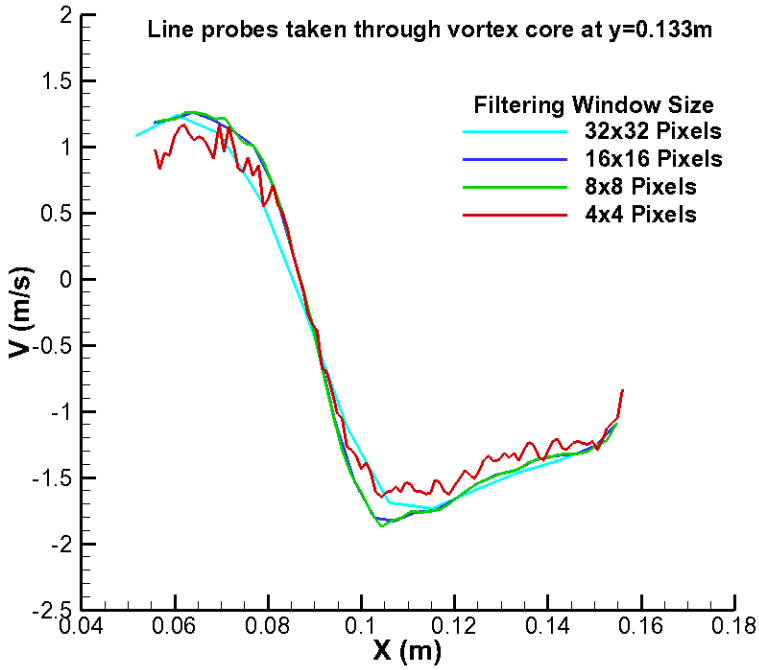

Figure 59 Line probes of V velocity with different filtration windows

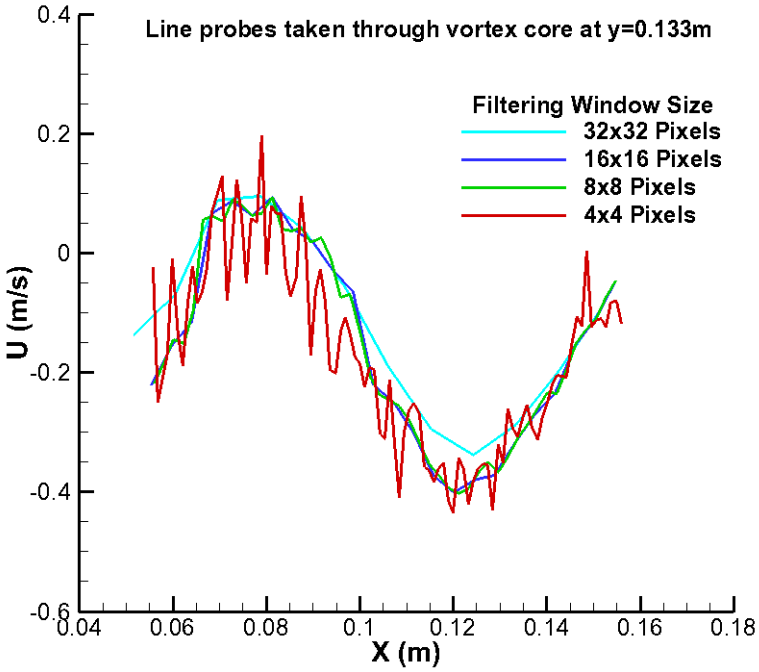

Figure 60 Line probes of U velocity with different filtration windows

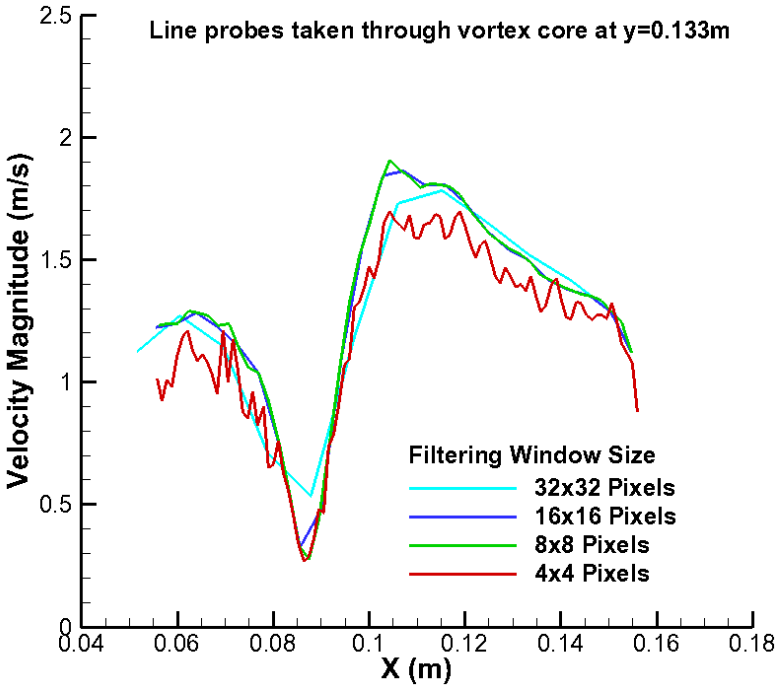

Figure 61 Line probes of velocity magnitude with different filtration windows

The primary objectives set out for this experimental objective was to obtain high fidelity pressure drop and velocity data across the side entry orifice for use in CFD validation. While many sets of data were acquired over the course of this project, ultimately a few were determined to be benchmark class data sets. Through the analysis, it has been determined that there are in fact large standing vorticies present just prior to the side entry orifice, and they do in fact shift sides across the 45 degree bisection of the orifice in an infrequent and unpredictable manner. This study was unable to conclusively determine the primary mode by which this vortex shift occurs, but only that it was seen. Pressure drop correlations have been determined through two extensive tests covering the operable range for which the facility was designed, and the 1D wavelet

semblance method was used to show high degrees of correlation between low frequency signals present within the flow.

3.2 Scaled Experiment of the Postulated Air Ingress Scenario in the VHTR

3.2.1 Background

The push for next generation reactors stems from the need for inherently safe and high efficiency energy sources. The prismatic block gas cooled reactor is one such proposed design that is helium cooled and relies on the high heat capacity of graphite to mitigate a catastrophic scenario in the event of a loss of coolant accident. While there are several modes that can lead to a loss of coolant scenario, none are as pronounced as the double ended guillotine break scenario in the co-annular inlet and outlet. A simplified illustration of the break location is shown in figure 62. Following a postulated break, depressurization of the helium takes place until a 'near' equilibrium is reached at which point oxygen carrying air begins to enter the reactor vessel.

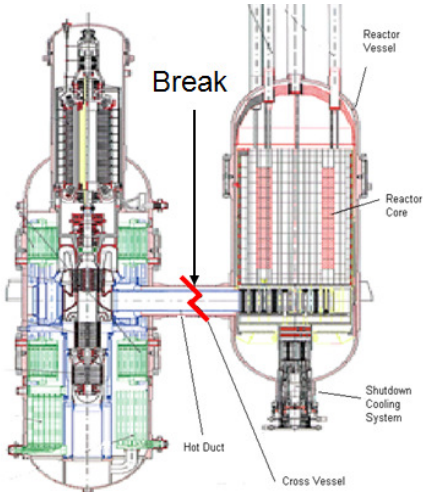

Figure 62 GT-MHR with postulated break location between the reactor vessel and turbine

The main concern of oxygen ingress into the lower plenum of the reactor vessel is the potential for oxidation to occur at the high temperatures. The resulting reduction in density[16] and degradation of structural integrity following sufficient oxidation could potentially place the core support structure at risk; however, there is debate over the presence of sufficient oxygen in the surrounding containment vessel to result in such high levels of oxidation.

Originally, it was thought that following the depressurization, oxygen would enter the reactor vessel following Fick's Law of diffusion described by equation 21, where J is the flux, D is the diffusivity, and φ is the concentration. By this principle, diffusion of oxygen gas molecules into the helium reactor environment is driven by the concentration gradient. For a higher gradient, a larger flux takes place. While the concentration gradient is large at the onset of the break scenario, the gradient quickly diminishes and the diffusion flux reduces with time. As a result, the time scale of the air

ingress following diffusion principles to populate the lower plenum of the reactor vessel with oxygen has been predicted to be on the order of ~150 hours[17] whereas the time scales predicted with CFD simulations[18] that assume the initial ingress of air into the lower plenum is driven by the density difference between the cooler high density air and the hot low density helium is on the order of a couple of minutes.

$$J = -D\frac{\partial \varphi}{\partial x} \tag{21}$$

The gravity driven counter current exchange of gas leading up to the eventual onset of natural circulation may be theoretically determined for a 2D channel flow by the manipulation of Bernoulli's principle[19]. The manipulation results in the bulk velocity of both the high and low density counter current flows described by equations 22 and 23. Experiments on the lock exchange problem in channel flows have shown that the 0.5 coefficient in equation 22, is actually closer to 0.44, but the relationship otherwise holds.

$$u_L = 0.5\sqrt{\frac{gd(\rho_L - \rho_H)}{\rho_L}} \tag{22}$$

$$u_H = \sqrt{\frac{2gd(\rho_L - \rho_H)}{\rho_L}} \tag{23}$$

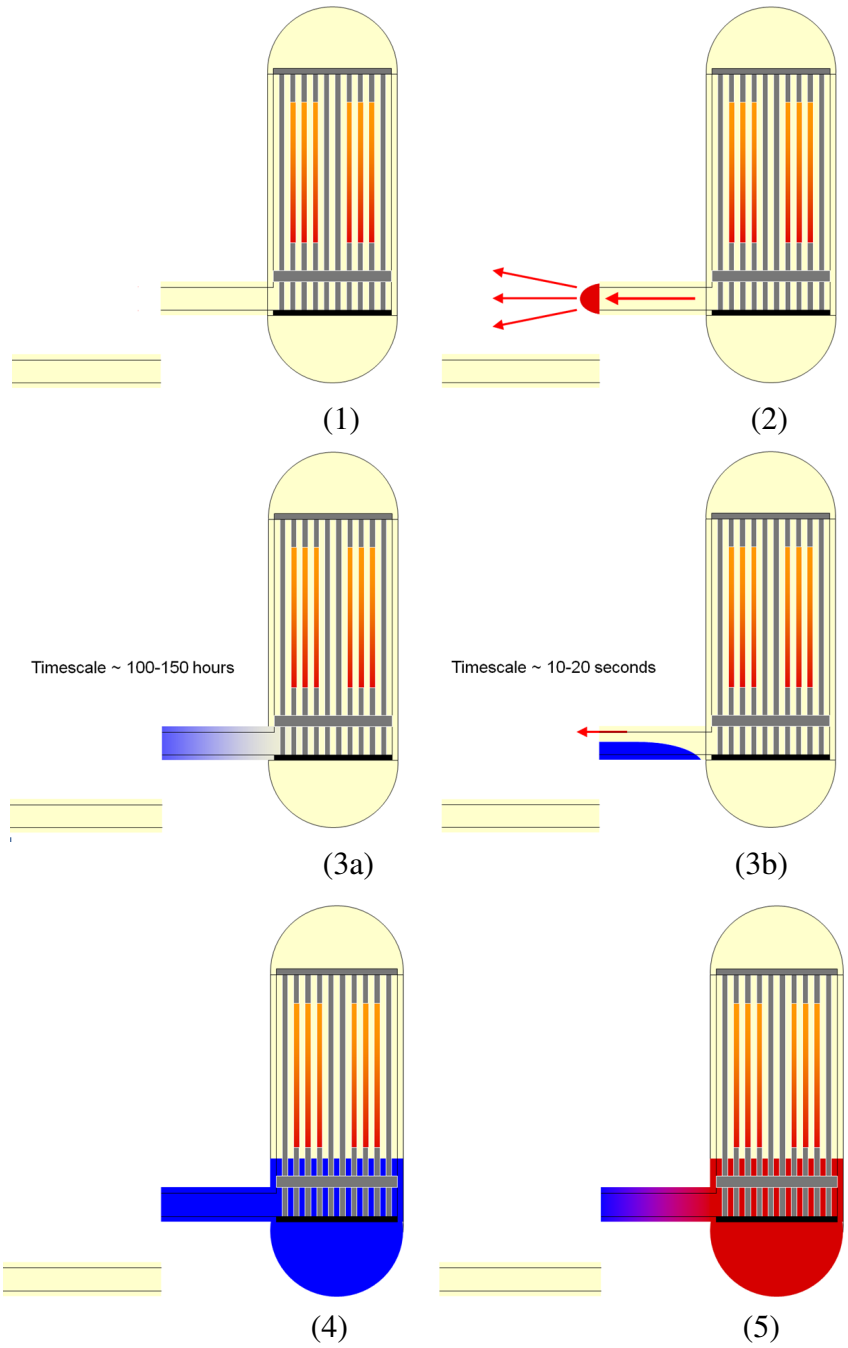

Figure 63 Stages of air ingress scenario: (1) Break, (2) Depressurization, (3a) Diffusion, (3b) Gravity driven flow, (4) Filling of lower plenum, and (5) Heating of lower plenum air

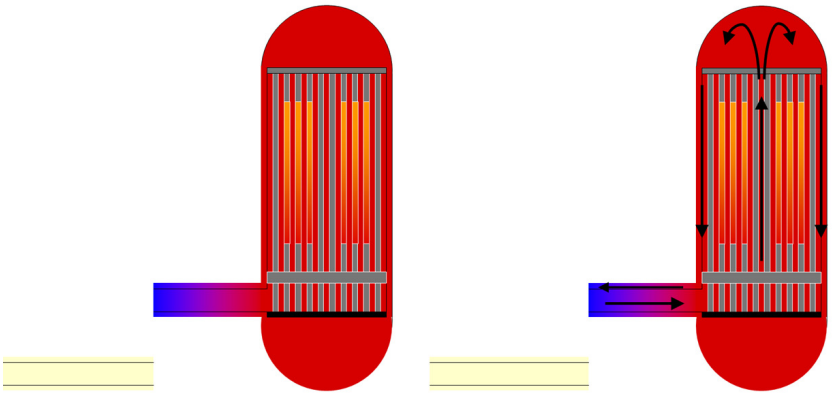

(6) (7)

Figure 64 (*cont.*) Stages of air ingress scenario: (6) Buoyancy driven filling of reactor vessel and onset of natural circulation and (7) Steady natural circulation

The stages of the proposed air ingress accident scenario are shown in figure 63 and figure 64. Initially, a double ended guillotine break occurs in the co-annular duct (1), followed by a depressurization of the hot helium in the reactor vessel (2). Phases 3a and 3b are the two modes in which air is thought to enter the reactor vessel. In phase 3a, the ingress mechanism is diffusion, and 3b is gravity driven flow. Once the cool air enters the lower plenum and begins to heat up (4 and 5), the air expands and begins to drive itself upwards (6) as additional cool air continues to flow in underneath the expanding hot air. This buoyancy driven mechanism is the same mechanism that leads to a steady natural circulation that continues to pull in cool air from the containment through the inner annulus and drive out hot air through the outer annulus (7). The continual replenishment of air into the lower plenum is a mechanism that has been proposed leading to oxidation of the support structure and a postulated large scale failure event of the lower plenum support structure. While simulations have been performed on

such scenarios, and simplified gravity driven current experiments have been performed, there is still a need to perform a prototypic experiment that matches the accident conditions closely. A scaled experimental facility aimed at representing the gravity driven flow stage of the accident scenario has been designed and constructed for the purpose of code validation and pieces of the data will be used in the present work for demonstrating the applicability of the newly proposed spatio-temporal wavelet method.

3.2.2 Experimental Design and Scaling Analysis

While analytical models for channel flows are fairly accurate, the geometry in the GT-MHR consists of two co-annular pipes. The need to validate the applicability of both analytical models and computational fluid dynamics (CFD) simulations against experimental data under the same phenomenological circumstances as in the postulated guillotine pipe break of the GT-MHR is necessary. To scale the phenomena properly, the densimetric Froude number is used as the driving dimensionless parameter. The reasoning behind the use of the Froude number is that the parameter is effectively based on a speed to length ratio that relates the gravitational flow front to the reduced gravity (which takes into account the density difference of the two fluids). The form of the Froude number used in the scaling analysis of this experiment is described by equation 24. When the ratio between the prototypic Froude number and the experimental Froude number is equal to unity, the experiment faithfully represents the dominant phenomena present in the accident scenario following depressurization.

$$Fr = \frac{u}{\sqrt{gd\frac{\Delta\rho}{\bar{\rho}}}} \tag{24}$$

By examination of the flow front velocity and Froude number formulations, it becomes clear that the most important terms are the density ratio between the light and heavy gases and the characteristic diameter of the channel or pipe. The first step was to scale the facility to geometrically match the GT-MHR design. The key geometries to scale were determined to be the co-annular pipes, reactor core diameter, lower plenum height, and outer communication channels that transfers the cool transferred to the upper plenum of the reactor vessel before travelling down through the core. A schematic of the facility is shown in figure 65 identifying the major components, and in figure 66 giving the geometric scales in inches.

The design of the facility was in a modular fashion to allow the co-annular pipe lengths to be changed to simulated different break distances from the reactor. The tank representing the containment vessel has been built with a flat viewing window that looks directly down the length of the co-annular pipes. The purpose for this window is to allow a sheet of laser light to be passed into the vessel at a right angle to avoid diffraction. At the long distance the light sheet must travel down the length of the co-annular pipe. The only mechanical device in the facility is the pneumatically actuated sliding knife gate valve. The particular valve in the facility was chosen for its ability to fully open in 0.53 seconds while still being able to hold a gas-tight seal when closed.

In the case of the actual reactor scenario, the depressurization of high temperature helium is expected to heat the air in the containment vessel, and in the final stages of the phase, the high thermal diffusivity of the helium is expected to lead to a rapid cooling of the outlet temperature. Further tests are needed to confirm the actual temperature in this region, but for the validation case scaling analysis, the outlet helium temperature was assumed to be around 300° C at the onset of the air ingress mechanism. The density of helium at different conditions was calculated from an empirical relationship developed out of an extensive collection of data[20] on helium across a wide range of temperatures. This relationship is described by equation 25.

$$\rho = 48.14\,\frac{P}{T}\left[1 + 0.4446\,\frac{P}{T^{1.2}}\right]^{-1} \quad \left(\frac{kg}{m^3}\right) \tag{25}$$

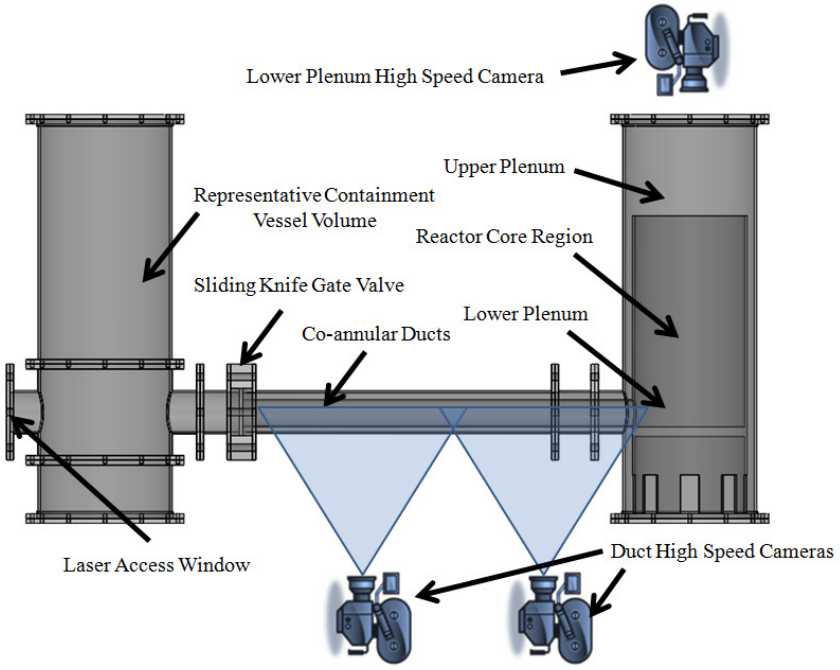

Figure 65 Air ingress experimental facility with major components identified

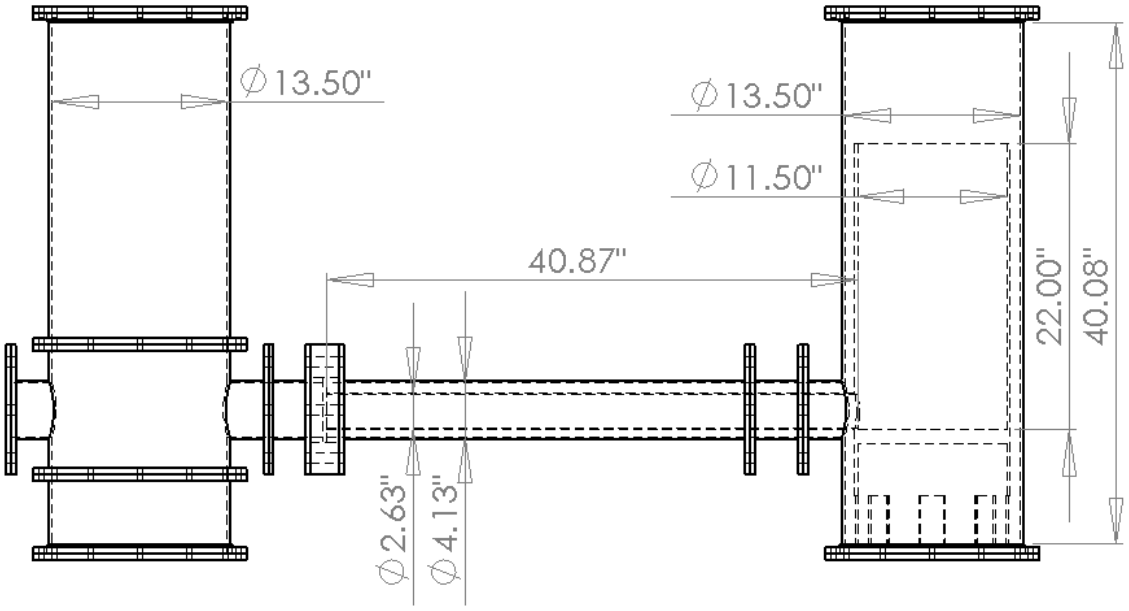

Figure 66 Air ingress experimental facility with geometric scales

Table 10 Scaling parameters used in design of experimental facility for He-SF6 test

Parameter	GT-MHR	Experiment
Vessel Diameter (m)	6.800	0.296
Cold Duct Diameter (m)	2.400	0.104
Hot Duct Diameter (m)	1.500	0.065
D_{cold}/D_{hot}	1.600	1.600
ρ_{heavy} (kg/m3)	1.226	6.270
ρ_{light} (kg/m3)	0.084	0.179
$\rho_{heavy}/\rho_{light}$	14.596	35.106
u_{heavy} (m/s)	4.211	2.110
u_{light} (m/s)	1.567	0.347
u_{heavy}/u_{light}	2.687	6.081
Froude Number	**0.322**	**0.315**

The scaling parameters and analytical flow front velocity calculations are shown in table 10. These are the final experimental design parameters used for the gas-gas flow case; however, in a preliminary study of lock exchange flows, the facility was tested with water and brine solutions. The density ratio of these two fluids was measured to be approximately 1.13. The scaled parameters for the water-brine case are shown in table 11. The Froude number in this test does not match as closely as in the gas-gas test case, but it is still a reasonable scaling.

Table 11 Scaling parameters used in design of experimental facility for water-brine test

Parameter	GT-MHR	Water-Brine Experiment
Vessel Diameter (m)	6.800	0.296
Cold Duct Diameter (m)	2.400	0.104
Hot Duct Diameter (m)	1.500	0.065
D_{cold}/D_{hot}	1.600	1.600
ρ_{heavy} (kg/m3)	1.226	1125.480
ρ_{light} (kg/m3)	0.084	996.000
$\rho_{heavy}/\rho_{light}$	14.596	1.130
u_{heavy} (m/s)	4.211	0.161
u_{light} (m/s)	1.567	0.151
u_{heavy}/u_{light}	2.687	1.063
Froude Number	**0.322**	**0.427**

As previously documented in a thesis on this particular experiment[21], the flow front velocities in the co-annular duct of the water-brine test matched up very closely with the analytical flow front velocities and the calculated flow front velocities obtained from CFD simulations using large eddy simulation methods. Two cases were performed

with co-annular pipe lengths of 0.38m and 1.0m for cases A and B respectively and the results presented in table 12 indicate good agreement with one another.

Table 12 Comparison between air ingress flow front velocities calculated and determined experimentally.

Flow Front Velocity (m/s)		
	Case A	**Case B**
Benjamin's Theory	0.161	0.161
Experimental	0.164 ± 4.29 %	0.168 ± 3.64 %
CFD	0.17	--

The analysis of flow front speed has been done previously[21], but the purpose of inclusion in this piece of work is because of the presence of a particular flow feature in the brine-water test when the brine enters the simulated lower plenum region of the reactor vessel. In this test, a camera view from above the lower plenum allows the flow front of the heavier brine solution to be visualized as it exits the inner hot duct pipe and spreads to fill the larger area. Following the initial flow front head into this region, a distinct wave pattern develops at the exit region of the pipe. The time sequence shown in figure 67 illustrates the onset of this large scale frequency.

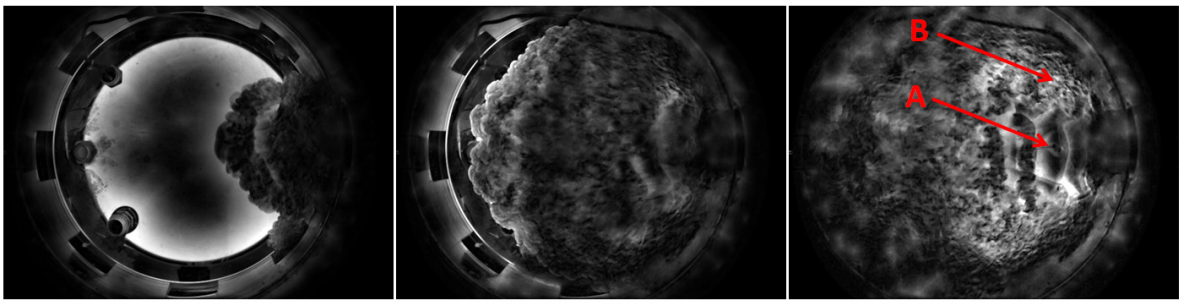

(1) (2) (3)

Figure 67 Time lapse of onset of instability in lower plenum of GT-MHR

The shadowgraphy method employed allowed for such dramatic images of the flow features to be obtained. Backlighting the visualization section was done by placing a uniform capacitative light source below the simulated reactor vessel and a high speed camera above the vessel. In this flow visualization test, dye was added to the brine solution to make the flow more distinguishable. The resulting solution transmits light proportional to depth with significant light absorption when the fluid is greater than about two inches deep. In this fashion, it becomes very easy to detect shallow and deep regions by the amount of light penetration through the flow. By applying a filter to normalize the levels of the image, features are further exaggerated to the point that distinct rib vortices present on the large scale fluctuations near point A become apparent as well as small scale fluctuations in the viscous super-layer at point B.

Obtaining the grayscale value between 0 and 255 of a pixel at point A for each time-step, the resulting signal may be used for performing a FFT to obtain global frequency information. The signals at points A and B are shown in figure 68 and figure 69. By observation, it is evident there are large scale fluctuations in point A with less

smaller fluctuations present in the signal indicative of smaller scales of turbulence. This is consistent with visual inspection of the flow features in this region. The signal of point B, which is present within the viscous super-layer of the incoming flow, has a significantly noisier signal which can be attributed to the shear generated turbulence in this location producing many disturbances within the brine solution, thus affecting the obtained signal. Even despite the turbulence generated noise, it is still clear around t=2s, that the strong fluctuations from point A are present in this region.

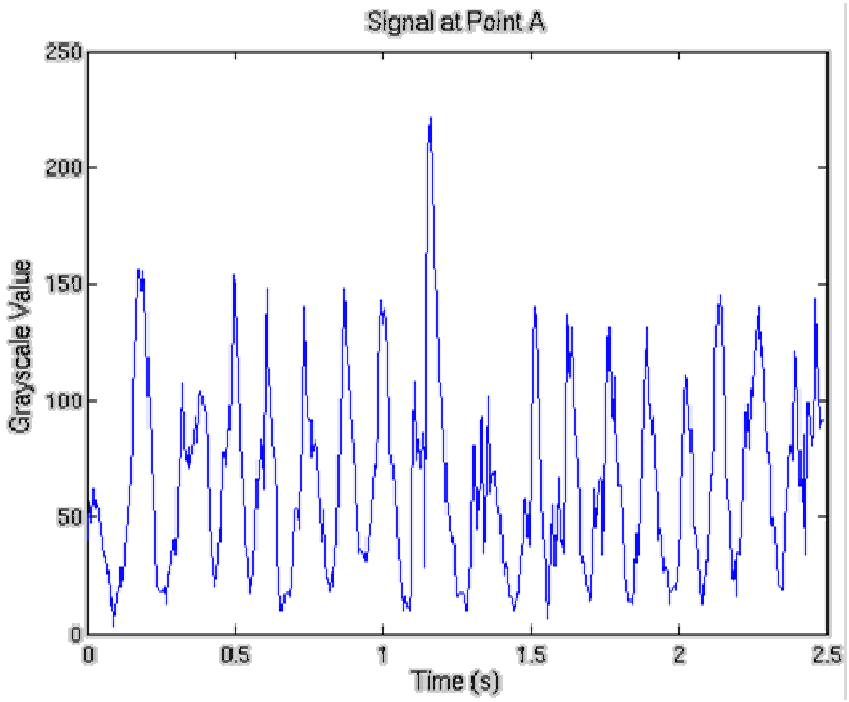

Figure 68 Grayscale value at point A of air ingress lower plenum

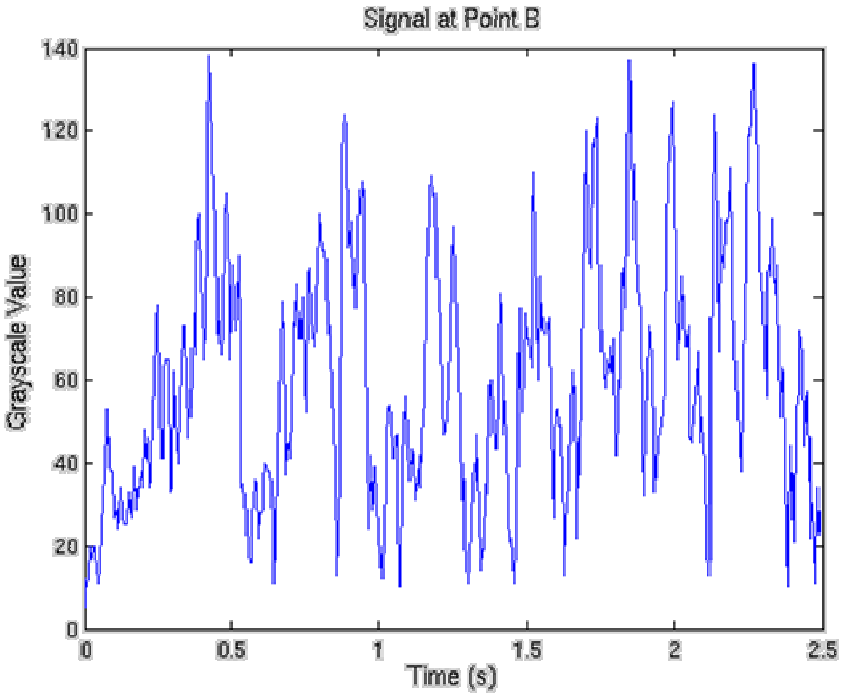

Figure 69 Grayscale value at point B of air ingress lower plenum

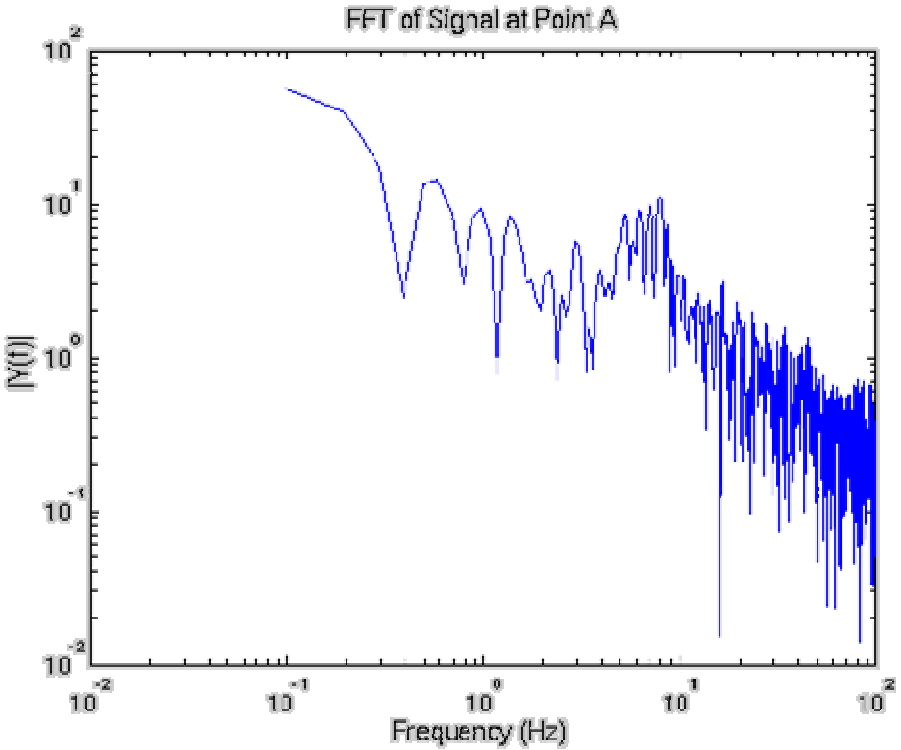

Figure 70 FFT of large scale fluctuations at point A in air ingress lower plenum

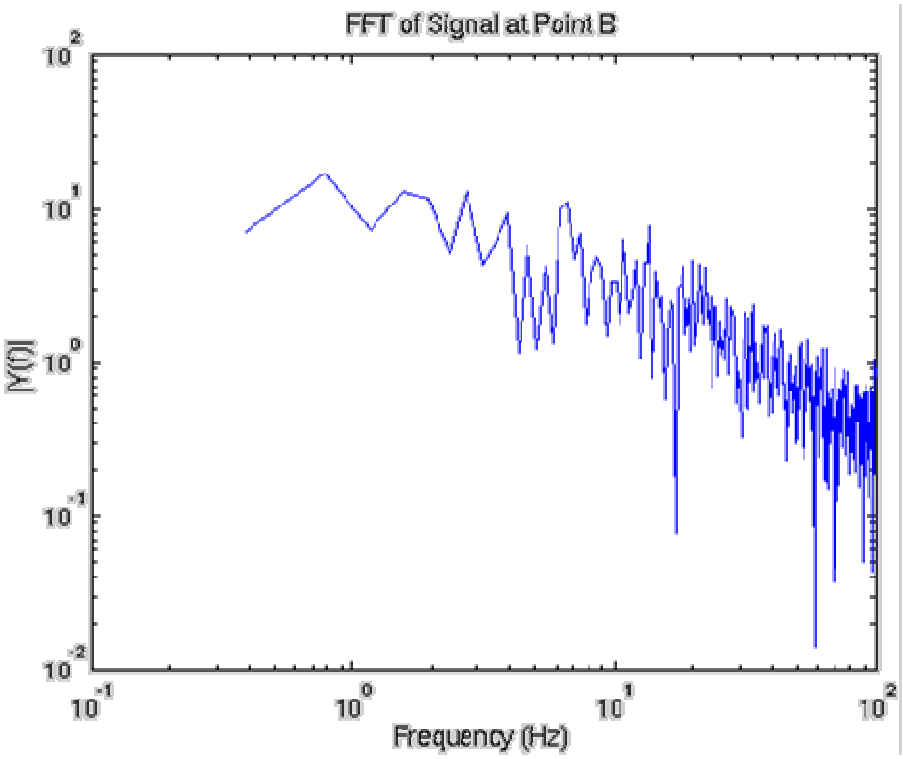

Figure 71 FFT of small scale fluctuations at point B in air ingress lower plenum

The FFT results of the signal at point A (figure 70) indicates a strong frequency present around 6.7 Hz. The FFT of the signal at point B (figure 71) indicates no clear dominant frequency, but instead a very uniform cascade of energy across the frequency spectrum.

3.2.3 Spatio-Temporal Wavelet Method Applied to Raw Images

This section serves to make use of the filtered images and apply the spatio-temporal 1D wavelet method proposed in this work for visualization of the propagation of the frequencies in this entrance region. Based on the FFT of the grayscale signal

obtained at point A, the frequency at which the large scale fluctuation occurs is around 6.7Hz. The dominance and scale of the frequency makes it easily identifiable in the raw images, and provides a good verification data set for the method. An instantaneous snapshot of the flow following the onset of the fluctuation with is shown in figure 72(a). The same snapshot using the spatio-temporal wavelet method at a frequency of 6.77 Hz (figure 72(b)) shows the correlation intensity in the domain. The striping that is seen is at half the wavelength of the instabilities. A zoom on this region is shown in figure 73, with the peak and trough of a single wavelength is indicated in red and blue. The black stripe separating these two colored regions indicates the point of inflection in the signal at this frequency.

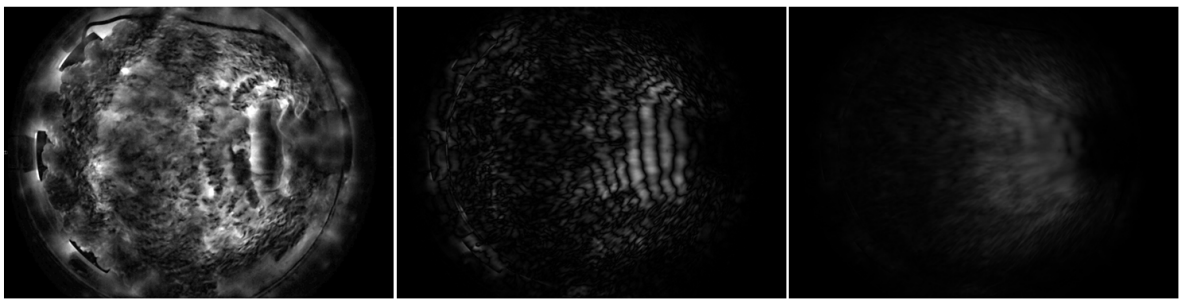

(a) (b) (c)

Figure 72 Spatio-temporal wavelet decomposition of lower plenum instability at 6.77 Hz showing (a) filtered image, (b) wavelet snapshot, and (c) average coefficient contour map

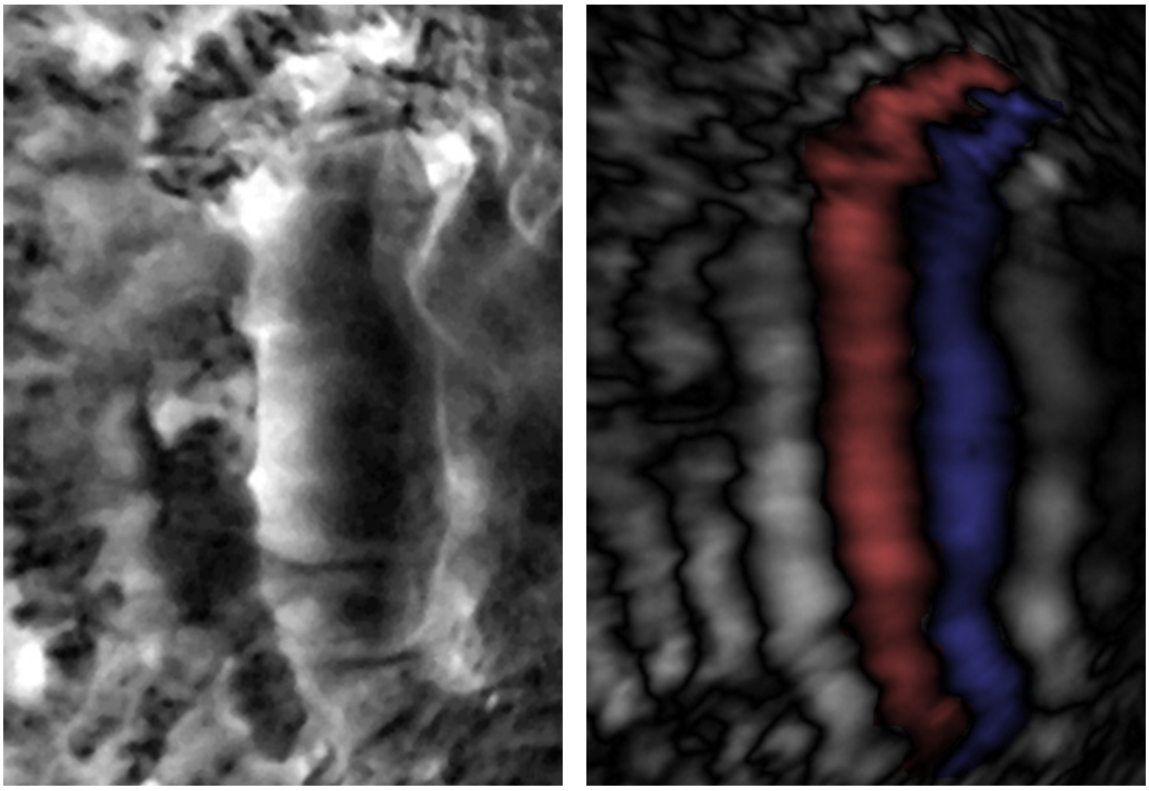

Figure 73 Zoom of instantaneous wavelet coefficient map at 6.77 Hz

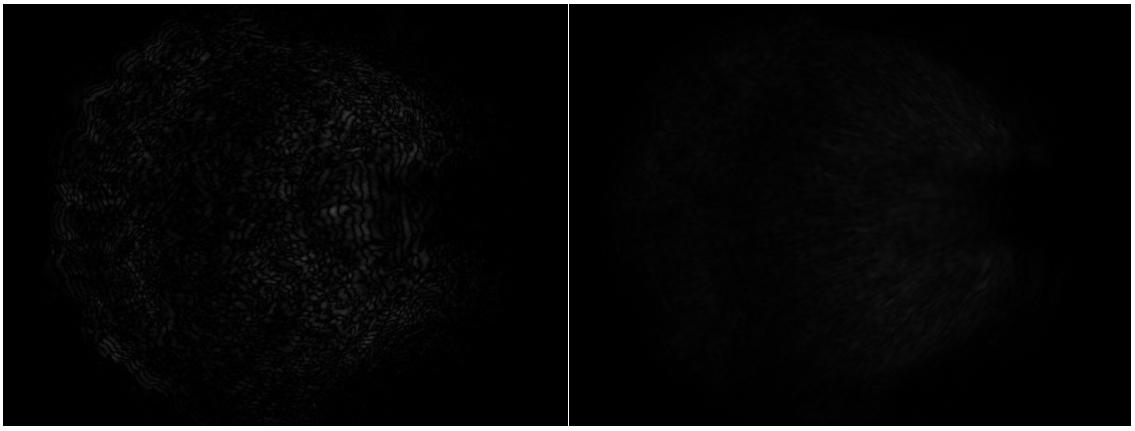

(a) (b)

Figure 74 Instantaneous(a) and average(b) wavelet coefficient decomposition at 20.3 Hz showing little dominant presence of the frequency

At higher frequencies such 20.3 Hz shown in figure 74, the lack of a large dominance at this frequency leads to an instantaneous coefficient plot that shows low intensity coefficients, but it is quite clear that it does not have a dominant presence in the flow. This test case successfully demonstrates the applicability of the spatio-temporal 1D wavelet method proposed for decomposition of raw images. Without any modification other than the way the data is imported, this same method may be applied to instantaneous velocity fields and fields of turbulence quantities such as Reynolds stress components. The next section investigates the same method applied to vector fields generated as part of a CFD validation study.

3.3 CFD Simulations of Iso-thermal Jets in a Staggered Rod Bundle

3.3.1 Introduction

The Gas Turbine – Modular Helium Reactor (GT-MHR) design of General Atomics is a proposed high temperature reactor that offers the benefit of higher outlet coolant temperatures that may then be used for both producing electricity at higher thermal efficiencies, as well as enabling the higher temperature process heat to be linked to hydrogen production and other high temperature applications. The primary coolant path in this reactor concept is downwards through the core before impinging in the lower plenum populated with core support columns and then exiting out a single duct. The experimental work of Amini and Hassan[22] investigating isothermal jet interactions

within a staggered rod bundle served as the validation data set for this computational study. This study focuses on comparison of large eddy simulation (LES) results using two different numerical schemes with experimental data in order to advance best practice guidelines further for such flows.

The experimental test section used in this investigation is represented in figure 75 with the measurement plane bisecting both jets. The test section includes a rectangular channel with a length of 1 m and a square cross sectional area of 76.2×76.2 mm^2. An array of staggered rods is set inside the channel which represents the configuration of the graphite supports rods within lower plenum geometry. The channel has a single outlet modeling the single outlet of the lower plenum (i.e. hot duct). Moreover, the two inlet jets which model the flow of the helium jets into the lower plenum are fixed to the top wall of the channel. Inlet Reynolds numbers and measurement locations along the mid-plane bisecting the two inlet jets are indicated in figure 76.

Water was used as the working fluid in this experiment and the results were obtained under isothermal condition. In order to obtain the jets' mean velocity, one flow-meter is installed in each of the flow loops that are designed for each of the jets. Reynolds numbers are based on bulk inlet velocity and nozzle diameter.

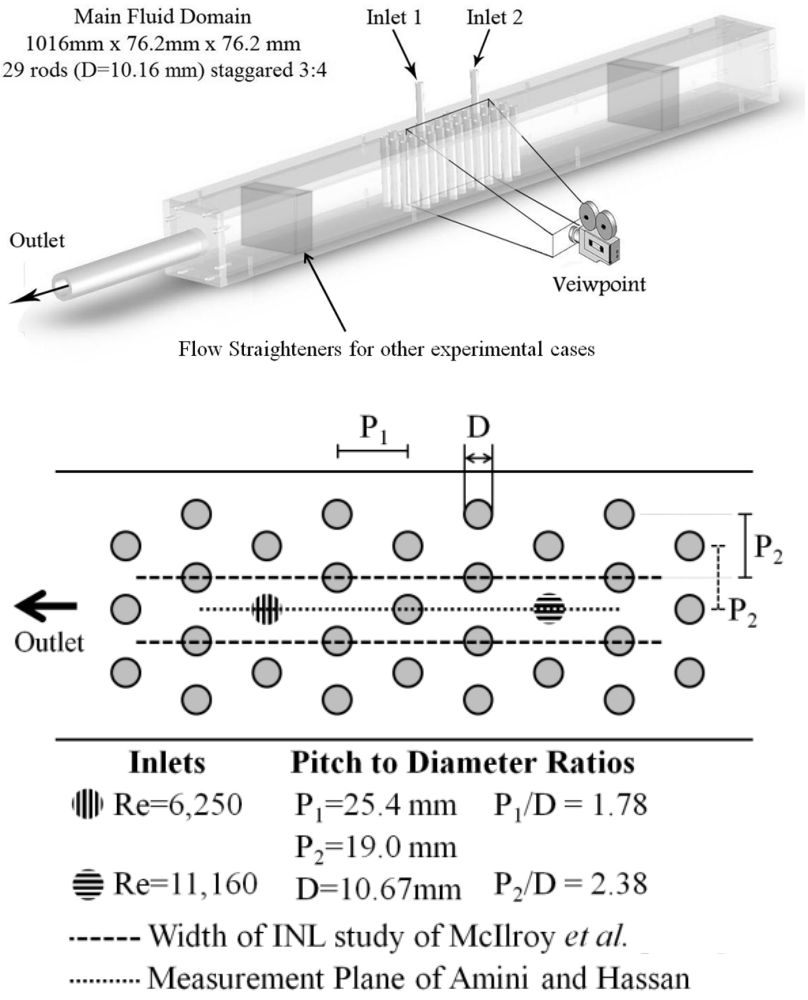

Figure 75 Experimental setup of Amini and Hassan[22]

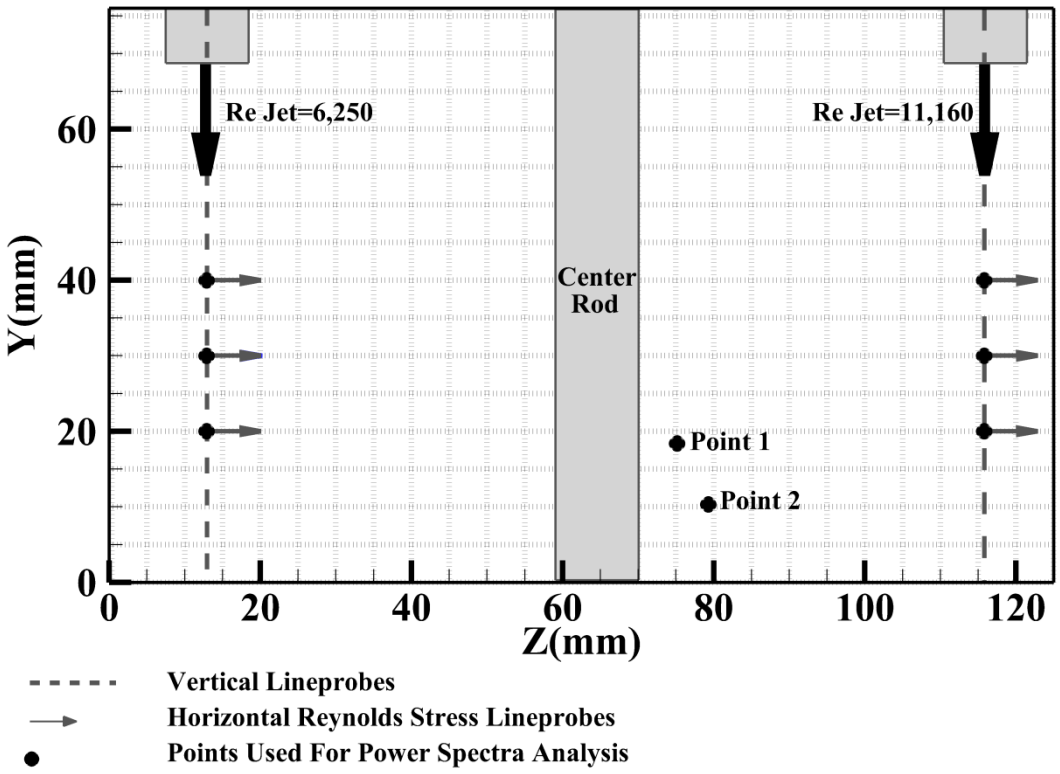

Figure 76 Line probes and point locations used for validation

A study by Shu *et al.*[23] on round jets at these Reynolds numbers indicated the presence of strong Kelvin-Helmholtz instability generation in the viscous super-layer of the jet plume into a quiescent fluid body. In these regions, the higher velocity in the flow leads to a low pressure within the plume, driving a slight contraction in flow area that leads to the onset of a ring vortex disturbance. This disturbance reduces the jet plume area, leading to a higher core velocity, thus reinforcing the low pressure zone and driving the ring vortex to continue to grow in size until it is sufficiently far from the jet source and loses the energy needed to sustain its coherence. At this point, viscous forces dissipate the energy into smaller structures before ultimately diminishing the structure all

together. The purpose of this study focuses on the importance of these smaller scales of turbulence in such configurations to accurate prediction of such flows.

An extensive set of experiments was performed by Cooper *et al.*[24] to study the behavior of turbulent air jets impinging on a flat plate using hot wire anemometry. Two different Reynolds numbers ($Re=2.3\times10^4$ and 7×10^4) and different jet-to-plate distances (from two to ten diameters) were considered for these set of experiments. To have a comparison between the experimental results with the results obtained by different turbulence models (k–ε eddy viscosity model and three other second moment closure models), a numerical study was done by Craft *et al.* [25] applying four different turbulence models using the same geometry and flow characteristics. The comparison is mainly focused on the data obtained for cases of two and six diameters distance between the jet and the impingement plane. None of the four models is capable of fully capturing the effect of the Reynolds number. Moreover, both k–ε eddy viscosity model and the "basic" Reynolds stress model show poor agreement with the experimental results and predict larger turbulence levels close to the stagnation point of the jet. However, the "new wall-reflection model" and the "new Reynolds stress model" provide a significantly improved agreement with the experimental results in capturing the effect of the jet to impinging plate distance.

The flow field of twin turbulent impinging air jets was experimentally and numerically studied by Abdel-Fattah[26]. Several cases were studied with different Reynolds numbers ($9.5\times10^4\leq Re\leq22.4\times10^4$), nozzle to plate distance ($3\leq h/d\leq12$), nozzle to nozzle centerline spacing (l/d=3, 5, and 8) and jet angle (0° to 20°). The experimental

measurements were obtained using pressure taps installed on the impingement surface while the numerical calculations were performed using a finite volume method to solve the mass, momentum, turbulent kinetic energy, and turbulent kinetic energy dissipation rate equations. The result show that jet spreading decreases by increasing the nozzle to plate distance.

Flow characteristics of gaseous impinging jets with $1000< Re <4000$ are numerically and experimentally studied in an investigation done by Angioletti *et al.*[27]. PIV technique is applied to obtain the velocity fields of the impinging jets. Moreover, three different turbulence models (k–ε Re-Normalized Group (RNG), k–ω Shear Stress Transport (SST) and the Reynolds Stress Model (RSM). The CFD results have been validated against the experimental results. It was concluded that at lower Reynolds numbers, the k–ω SST model provided a better agreement with the experimental data; however, for higher Reynolds number cases, k–ε RNG and RSM turbulence models compared better with the experimental data.

Sengupta and Sarkar[28] performed experimental and CFD studies on the outflow velocity characteristics of a microburst type thunderstorm modeled as a round impinging jet with Reynolds number of 1.4×10^5 and 2.2×10^5. Hot wire anemometry, PIV, and pressure racks were utilized for experimental measurements of the flow field while different turbulent models such as k–ε (standard, RNG, realizable), k–ω(SST), Reynolds stress model (RSM), and large eddy simulation (LES) were used for the numerical simulations. The comparison between the numerical and experimental results show that all the turbulence models were successful in capturing the decay of the jet

centerline velocity and the boundary layer growth; however, LES, realizable k–, and RSM models provide values that better correspond to the experimental results than compared to the other turbulence models.

Previous simulations by Salpeter and Hassan[29] involved using semi-structured polyhedral grids with the standard and realizable k-ε models as well as large eddy simulations (LES). This previous study incorporated an extensive grid sensitivity study incorporating seven levels of refinement and following the best practice guidelines for quantifying discretization error. In the present work, LES results are compared between the polyhedral and hexahedral grids. The key numerical difference between grid types is in the ability of the hexahedral grid to be used with a central-difference (CD) scheme as opposed to the use of a second order upwinding (SOU) approach with the polyhedral grid. The SOU approach uses high levels of second order upwinding to maintain stability in the solution. The upwinding subsequently kills smaller scales of turbulence that are not dissipated in a CD scheme.

3.3.2 Methods

To obtain the velocity fields within the rod bundle, Matched Index of Refraction (MIR) and Particle Image Velocimetry (PIV) techniques are applied through the experimental investigation. Matching the refractive index of the material of the tubes

used for the rob bundle with that of water provides the optical access that is required to acquire the velocity fields in the interior regions of the rod bundle.

In the experimental study, a 2D Dynamic PIV technique is employed to obtain the velocity fields within the flow field. The PIV system consists of a high power laser, a set of mirrors and lenses, and a high resolution/high speed CCD camera. The laser beam was transformed into a laser sheet using the set of mirrors and lenses. The laser sheet illuminated planes parallel to the vertical access within the test section. The CCD camera recorded videos of the illuminated planes at a rate of 1000 frames per second over a 5 second period resulting in having a total of 5000 PIV images for each experimental case. The uncertainty analysis on the adequacy of the number of the recorded images shown by Amini and Hassan[22] confirms the 5,000 images recorded in this experiment provide a large enough sample size to capture the flow behavior. Moreover, the uncertainty analysis performed on the PIV analysis software using the PIV standard images shows that the error of the PIV analysis software is of sub-pixel order (0.629 pixel/(time-step)).

In this study, comparisons are made using large eddy simulations (LES) using two different numerical schemes. The LES approach is a transient model which resolves large scales using the filtered Navier-Stokes equations (eqn. 26), and uses a sub-grid scale(SGS) model for the turbulent stress tensor to model the effects of scales smaller than those resolved. The scales modeled are those on the order of the dissipation scales, which would only be resolved through the impractical use of direct numerical simulations (DNS), thus necessitating the use of a modeling approach for theses smallest

scales. The turbulent stress tensor, $T_{ij,}$ is represented in equation 27 as a function of the subgrid scale turbulent viscosity μ_t, kinetic energy k, and the strain rate tensor $\overline{S_{ıȷ}}$.

$$\frac{\partial \overline{u_ı}}{\partial t} + \frac{\partial \overline{u_ı u_ȷ}}{\partial x_j} = -\frac{1}{\rho}\frac{\partial \bar{p}}{\partial x_i} + \frac{\partial^2 \overline{u_ı}}{\partial x_j^2} - \frac{\partial \tau_{ij}}{\partial x_j} \tag{26}$$

$$T_{ij} = 2\mu_t \overline{S_{ıȷ}} - \frac{2}{3}(\mu_t \nabla \cdot \boldsymbol{v} + \rho k) \tag{27}$$

Where $\overline{S_{ıȷ}}$ is computed by:

$$\overline{S_{ıȷ}} = \frac{1}{2}(\nabla \boldsymbol{v} + \nabla \boldsymbol{v}^T) \tag{28}$$

The sub-grid model used was the wall adapting local eddy-viscosity (WALE) model by Nicoud and Ducros[30]. The WALE SGS model was shown by its developers to better resolve laminar to turbulent transition while still not generating such transitional regimes in wall bounded Poiseuille flows. The WALE SGS model for turbulent viscosity μ_t is defined by the length scale Δ, density ρ, the strain rate tensor $\overline{S_{ıȷ}}$, the deformation tensor S_{ij}^d, and a constant C_w=0.544.

$$C_w.\ \mu_t = \rho \nu \tag{29}$$

$$\nu = (\mathrm{C_w}\Delta)^2 \frac{(S_{ij}^d S_{ij}^d)^{3/2}}{(\overline{S_{ıȷ}}\,\overline{S_{ıȷ}})^{5/2} + (S_{ij}^d S_{ij}^d)^{5/4}} \tag{30}$$

The deformation tensor S_{ij}^d is defined by

$$S_{ij}^d = [\nabla \boldsymbol{v} \cdot \nabla \boldsymbol{v} + (\nabla \boldsymbol{v} \cdot \nabla \boldsymbol{v})^T] \tag{31}$$

$$\Delta = \min(\mathrm{C_w V^{1/3}}, \kappa d) \tag{32}$$

The adaptation to the distance from the wall to better scale near wall eddy viscosity is accounted for in the length scale term Δ. This term is defined as shown in equation 32 where V is cell volume, κ=0.41 is the von Karman constant, and d is the distance to the nearest wall. The vortex method was used for turbulence generation at the inlet with 10% turbulence intensity and a length scale of 7% of the inlet pipe diameter.

The numerical schemes compared in this study for handling the convection term are the central-differencing and the second order upwinding schemes. The issue with upwinding is that it kills the turbulence faster than it would otherwise dissipate on the smallest scales due to the use of limited reconstruction gradients in computation of face values. This limitation results in a reduction of extrema in face values and therefore increased computational stability at the consequence of introduction of artificial diffusion in the result. This limited reconstruction method is not used in the central differencing scheme. The result is that the central differencing scheme preserves turbulent kinetic energy in the velocity field, but lacks the stability to be run with anything but a discretized mesh that is structured and has very low skewness angles. The use of unstructured grids, or grids with higher skewness angles, leads to the need to maintain stability though the use of second order upwinding as in the case of the polyhedral grid of the current study. It will be shown in a subsequent section that results obtained with the SOU approach only resolves the larger scales of turbulence and kills the smaller scales. The central differencing scheme applied to the fully hexahedral grid

enables a result with minimal diffusion to be computed and the results are compared using several analysis methods.

3.3.3 Discretization

The sensitivity study[29] of the discretization of the polyhedral grid followed guidelines outlined by Celik *et al*.[31] for applying Richardson's extrapolation on grids falling within the asymptotic range of convergence. The study found the results of the axial velocity to fall below 4.75% from the extrapolated solution locally in the low Reynolds number jet, and below 1% in the high Reynolds number jet. These discretization errors were calculated on local values, a far more strenuous test than global parameters typically used, and were felt to be within acceptable limits as they were less than experimental measurement uncertainty. The seven levels of discretization refinement of the polyhedral meshes tested are outlined in table 13.

The final mesh size in the polyhedral case, 0.3mm, was used as the largest possible cell size in the fully hexahedral mesh, while the jet plume free shear layer was refined to a minimum side length of 2.5μm. The hexahedral grid was refined at the nozzle edges down to 2.5μm or approximately 3.5η, where η is the Kolmogorov length scale. In the polyhedral mesh, wall y+ values had an average value below 2. The average y+ value for the fully hexahedral grid was below 1. Although discretization error bars has not been put on final result plots, Richardson's extrapolation for error

approximation has been performed on local values along the axial velocity line-probe (figure 77) over seven polyhedral mesh refinements following the criterion outlined in the Journal of Fluids Engineering's editorial policy on numerical uncertainty[31]. Figure 78 and figure 79 show horizontal cross sections of the discretized bundle, illustrating levels of jet plume refinement and near wall refinement for each grid.

Table 13 Grid sensitivity study meshes with the most refined polyhedral (PH1) and hexahedral (HH) grids used for LES

Grid Type	**Base Cell Size**	**Number of Cells**
HH	0.002mm - 0.30mm	103 million
PH1	0.30mm	26.5 million
PH2	0.65mm	13.2 million
PH3	0.75mm	10.2 million
PH4	0.90mm	7.7 million
PH5	1.20mm	5.6 million
PH6	2.00mm	4.4 million
PH7	3.00mm	4.2 million

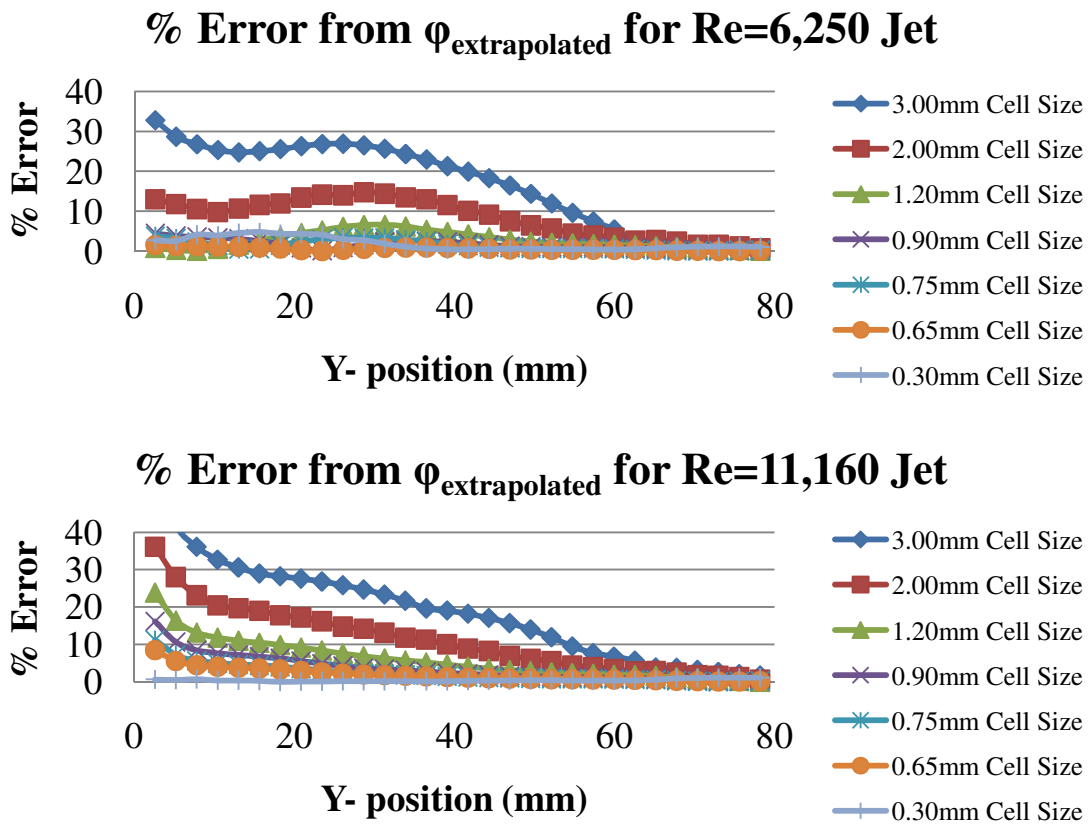

Figure 77 Grid convergence study of polyhedral grids against Richardson's extrapolated solution from grids PH5, PH4, and PH2 to satisfy extrapolation criterion

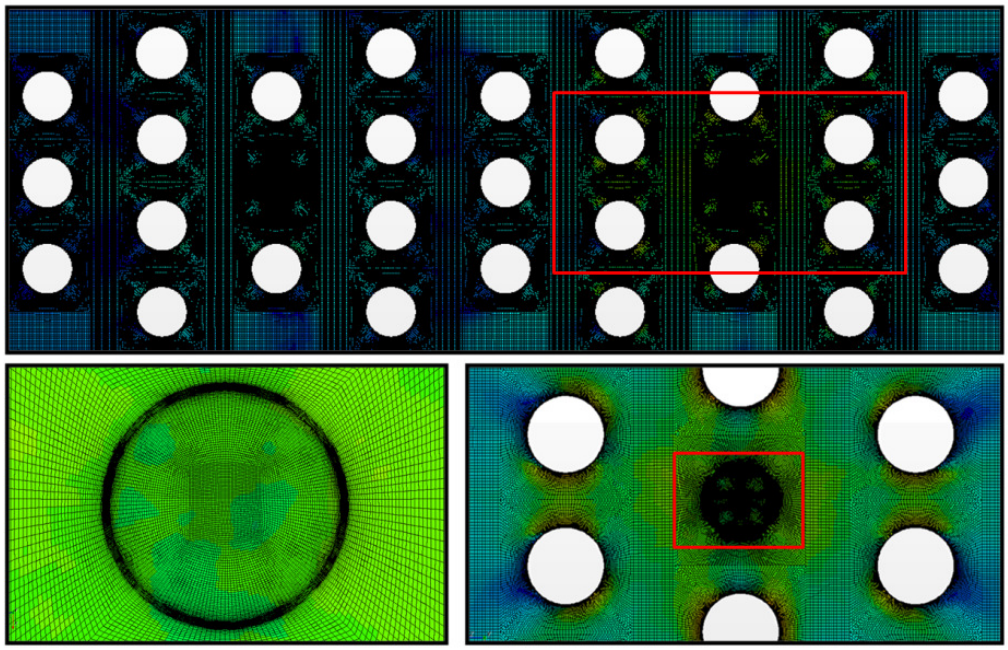

Figure 78 Plots of most refined hexahedral grid showing (*top*) impingement plane cross section at y=2mm, (*bottom right*) zoom on jet impingement site and neighboring rods, and (*bottom left*) zoom of cell refinement in shear layer region around jet plume.

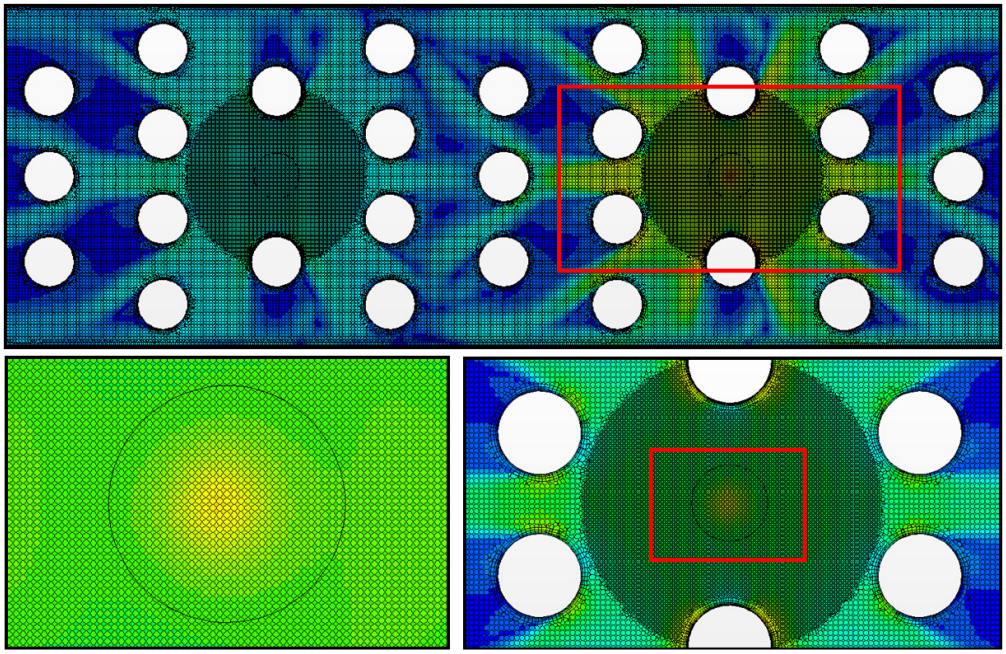

Figure 79 Plots of most refined polyhedral grid showing (*top*) impingement plane cross section at y=2mm, (*bottom right*) zoom on jet impingement site and neighboring rods, and (*bottom left*) zoom of cell refinement in shear layer region around jet plume.

3.3.4 Results and Discussion

Comparison of experimental and CFD results are done on various levels. Qualitative comparisons of velocity fields as well as quantitative comparison of velocity and turbulence quantities are done. These turbulence quantities include v'w' Reynolds stresses across the jet plumes and power spectra comparisons. Jet spreading rates and standard deviation of vw velocity components in the jet axis provide additional measures of comparison.

The contour plots of velocity and vorticity magnitudes of the mid-plane bisecting both jets (figure 80) show instantaneous snapshots of experimental and both LES results using different numerical schemes. Although the instantaneous point in time is not identical for each case, the contour plots illustrate what will be shown via more quantitative means further in this section. A look at the experimental data shows breakup of the core velocity within 1-2 hydraulic diameters of entering the quiescent volume. Small peaks in velocity with sharp gradients are indicators of eddy generation within the flow. This apparent breakup is due to the generation of small eddies as flow is sheared in the viscous super-layer of the jet plume. The eddy generating shear layer is visualized by observing vorticity quantities in the jet plume. The vorticity magnitude contour shows a relatively constant width of the viscous super-layer prior to impingement on the lower plane for the high Reynolds number jet.

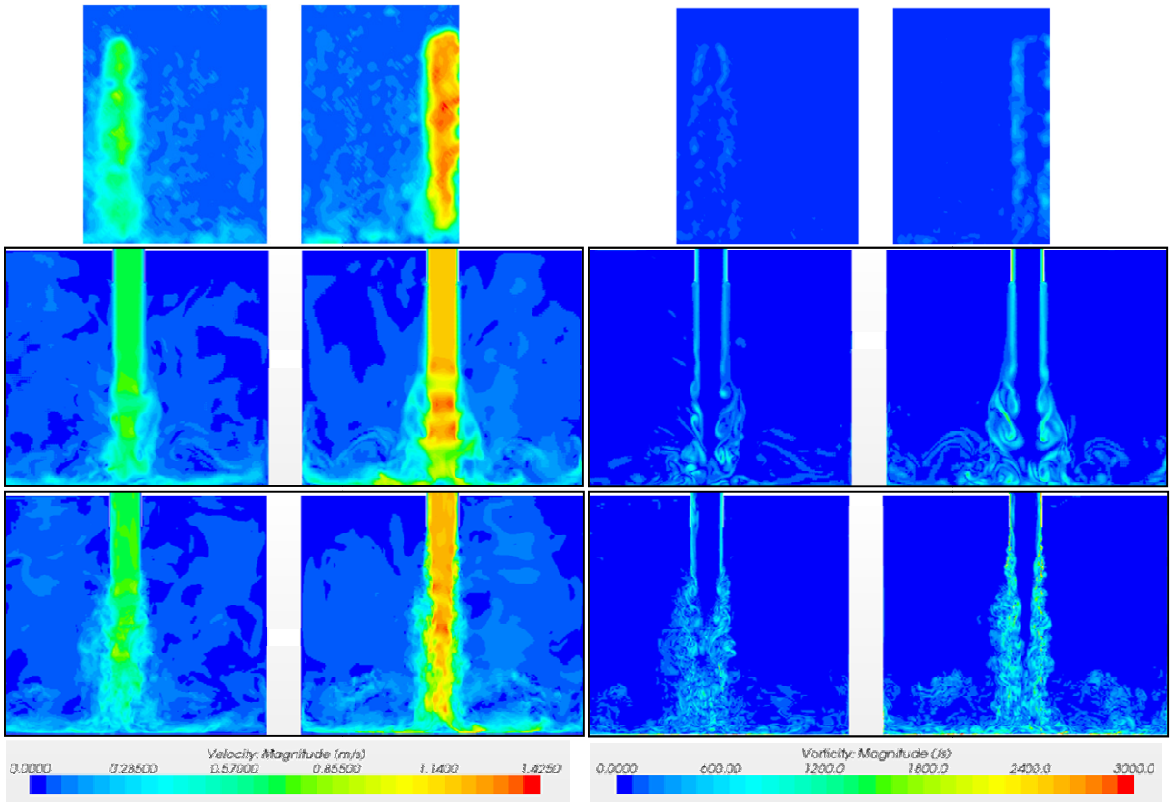

Figure 80 Contour plots of velocity(left) and vorticity(right) magnitudes for experimental data (top), LES results using second order upwinding (middle), and LES results using the central difference scheme (bottom).

Qualitatively comparing jet breakup between the experimental data and the two LES results, it is seen that the SOU scheme produced larger coherent structures due to the smaller scales remaining unresolved whereas the central differencing scheme produced instantaneous velocity results that more closely depict those in the experiment. Although this type of comparison is relatively superficial, it is an important observation to be made. As comparisons cannot be made on instantaneous fields of data, averaging in the time domain of the velocity fields is done and vertical line probes within the jet axis (figure 76) are used for extracting velocity profiles for comparison. The local discretization error in the axis of each jet is plotted for reference in figure 77[29] but is

omitted from the other plots. Experimental uncertainty error determined previously[22] has been included on the plots. The case of the Re=6,250 jet axial line probe (figure 81) shows two cases closely matching the experimental data. The first is the steady state case using the realizable k-ε model with the polyhedral cell mesh. The diffusive nature of both the model and the mesh result in a good agreement with experimental data, but possibly for the wrong reason. When running the same turbulence model with the extremely refined fully hexahedral mesh, the resulting solution has less decay in the axial velocity profile, giving evidence to less discretization driven diffusion in the jet plume. While the polyhedral mesh produced a more diffused result in the steady state solution, the time averaged LES results with the same mesh indicate less energy has been diffused out from the core region of the jet by smaller scale eddies in the viscous super-layer. A comparison of the LES results with the fully hexahedral grid using the central-differencing numerical scheme shows much better agreement with the experimental data and suggests better shear driven diffusion of the jet as it progresses in the domain. In the Re=11,160 jet, the axial line probes show that none of the tested models match very well with the experimental data; however, the LES results with the hexahedral mesh comes closer in the near impingement locations between y=0mm and y=15mm.

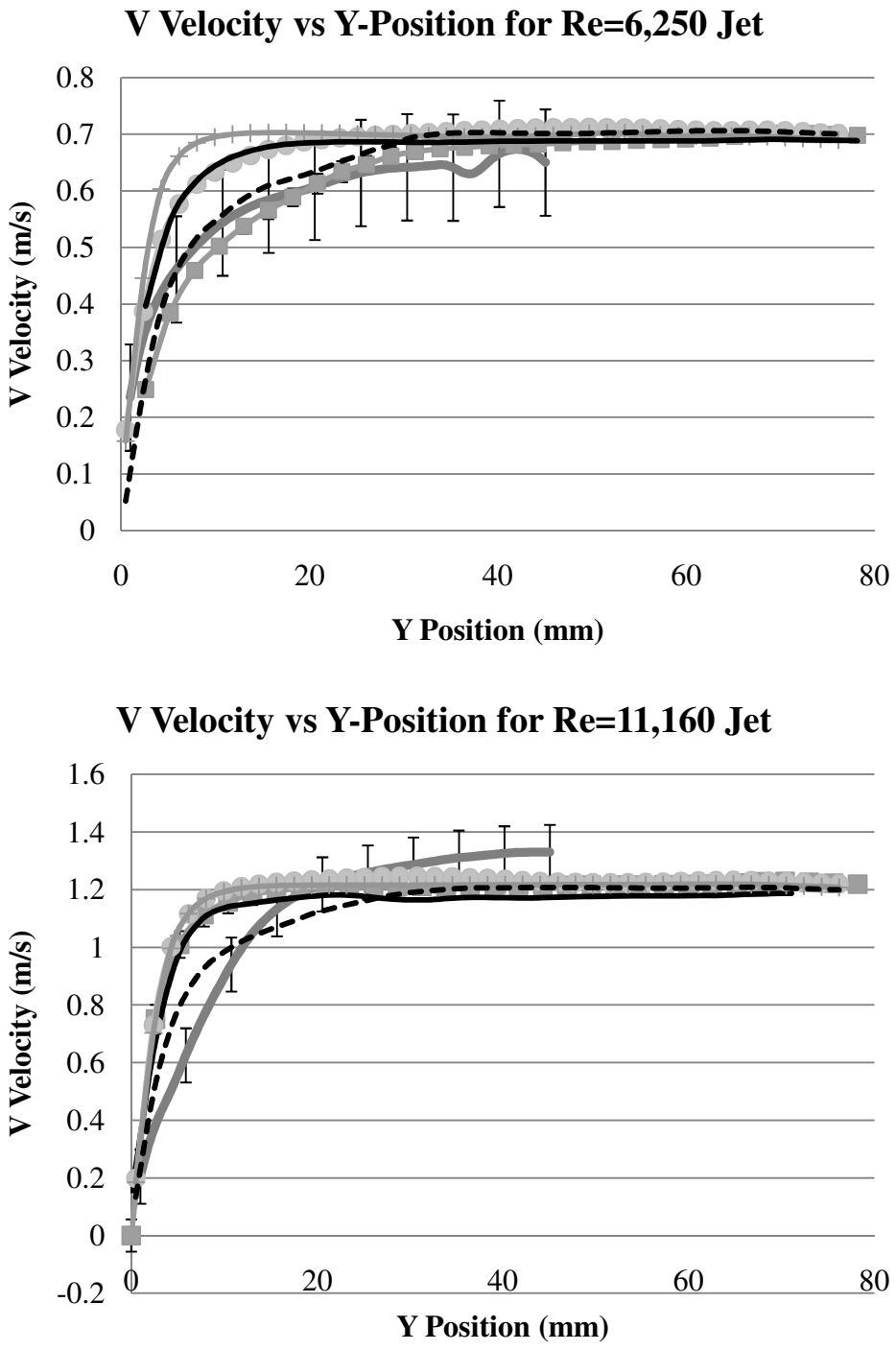

Figure 81 Vertical line probes of v velocity component in jet axis. —Experiment, —■— RKE w/ poly mesh, — LES w/ poly mesh, —●— RKE w/ hex mesh, —+— SST k-ω w/ hex mesh, --- LES w/ hex mesh

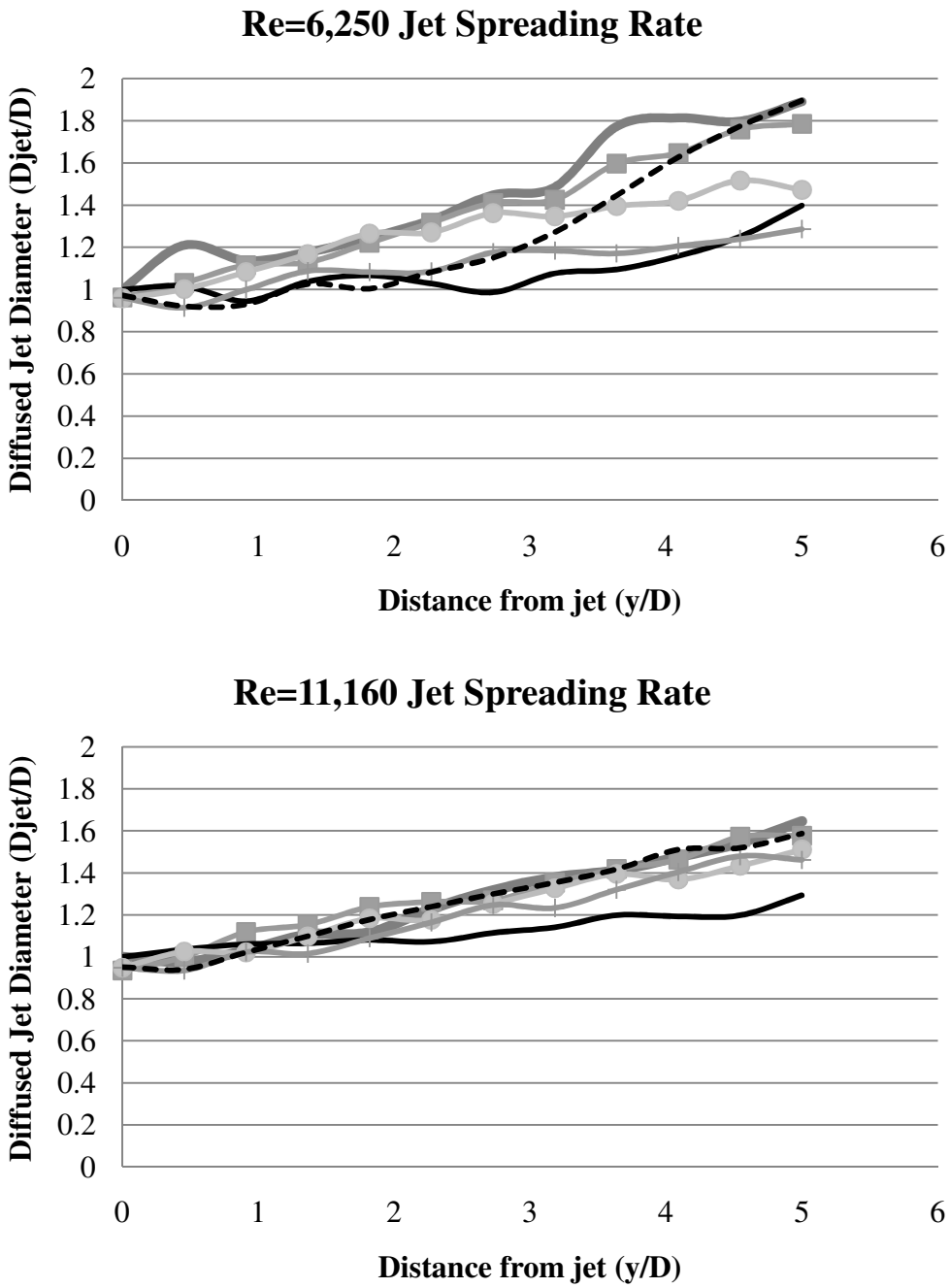

Figure 82 Jet spreading rate in jet axis based on $0.2V_{max}$ edge criterion. —Experiment, —■— RKE w/ poly mesh, — LES w/ poly mesh, —●— RKE w/ hex mesh, —+— SST k-ω w/ hex mesh, --- LES w/ hex mesh

To further investigate this reasoning, jet plume spreading rates are plotted for the experimental data and simulations. Typical jet diffusion studies are performed by taking horizontal line probes at different heights in each jet, and then using a plume edge criterion of $V_{edge}=C*V_{local,max}$ to dictate the location in the radial direction of the jet edge. Typical spreading rate studies use a spreading rate coefficient of C=0.5; however, in the case of the present study, the close proximity of the impingement plane to the jet outlet warranted the use of C=0.2 to allow larger variations in spreading rates to be seen between models. This variation is due to the choice of coefficient forcing the edge of the jet plume to be defined well within the shear layer where smaller scales are the dominant drivers of jet diffusion.

The spreading rates for both jets, shown in figure 82, show far less diffusion of the jet edges for the LES results obtained with the polyhedral grid than observed in the experimental data. The results of the hexahedral grid performed much better in regions y/D=4 to y/D=5 for the Re=6,250 jet, just prior to the impingement layer where small scale turbulent mixing is dominant within the jet. The fully hexahedral grid maintains good jet spreading rate agreement over the entire measured axial direction of the Re=11,160 jet, despite the discrepancy in the axial velocity measurement. Looking at the standard deviation of the planar velocity magnitude along the axis of each jet (figure 83), the degree of measured core fluctuation in the low Reynold's number jet matched up with the fully hexahedral grid LES results between y=0mm and y=25mm before it diverges. Comparison with the mean axial velocity line probes (figure 81) indicates also very good agreement over the same range. For the SOU scheme LES result, agreement

in the standard deviation was seen only around y=10mm. Again looking at the velocity line probes, it is seen that at a value of y=10mm, the rate of change of the mean axial velocity matches between experimental data and LES results with the polyhedral mesh. In the case of the Re=11,160 jet, the standard deviation matches up closely with both LES results; however, the rate of change of the hexahedral grid using the central-difference scheme indicates a closer transition between scales of turbulence as the jet progresses into the domain, but fails when the fluctuations spike as the flow impinges on the lower plane between y=0mm and y=20mm. This divergence was not seen at the lower Reynolds numbers, possibly indicating that at higher Reynolds numbers, there is certain intermittency effects not captured by either LES approaches as the jet breaks up in this highly turbulent region.

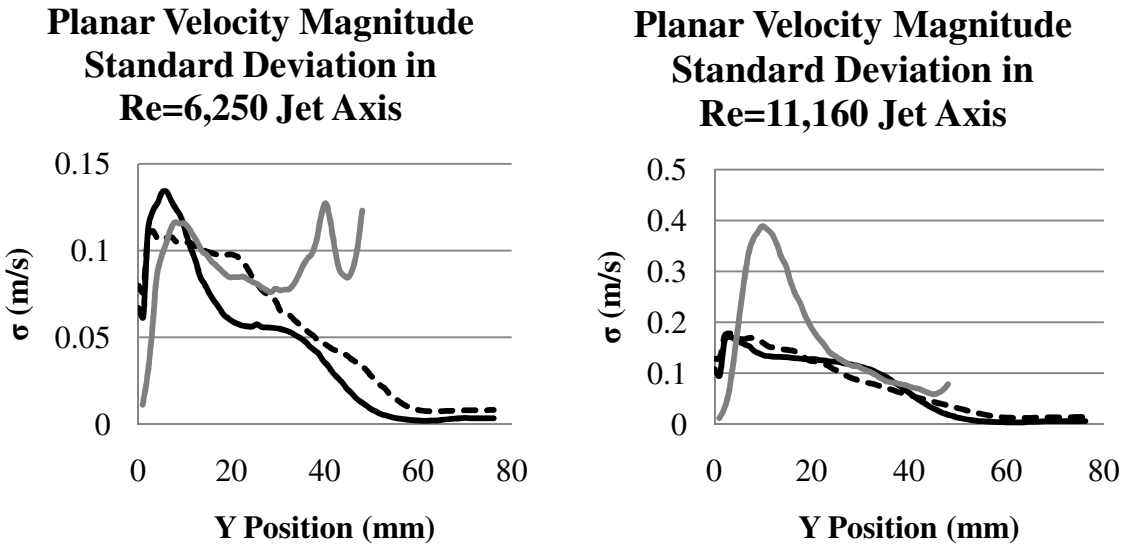

Figure 83 Standard deviation of VW velocity components in jet axis. —Experiment, — LES w/ poly mesh, --- LES w/ hex mesh

The Reynolds stress quantities taken across both jet plumes near the impingement layer at y=20mm (location shown in figure 76) show an over-prediction of Reynolds stresses for both LES results using the two different schemes (figure 84). The closest model to the experimental data was the steady state case using the Reynolds stress models (RSM); however, due to high degrees of instability in the solution the result never converged on a solution, but rather fluctuated in the jet plumes slightly. This instability is generated in the jet plume despite the use of a fully hexahedral grid with low skewness and refinement in the jet nozzle edge down to 3.5η, where η is the Kolmogorov length scale $7x10^{-7}$m. Due to this instability in this problem, the RSM was determined to be unsatisfactory for engineering purposes when the result generated does not settle on a truly converged solution. While the result generates instabilities that are actually similar to those occurring under the flow conditions in the experiment, the RSM results bear no physical meaning due to the numerical scheme not actually time marching.

Another comparison of methods uses the power spectral density of both LES result sets with different numerical schemes, the experimental data, and theory (figure 85 and figure 86). Kolmogorov's renowned derivation dictates that the decay of the turbulent energy spectrum in the inertial range follows a -5/3 power law decay[32]. This decay line has been included for reference against experimental and simulation results. In the cases of the probe locations within each jet, the experimental data closely matches the -5/3 decay as expected.

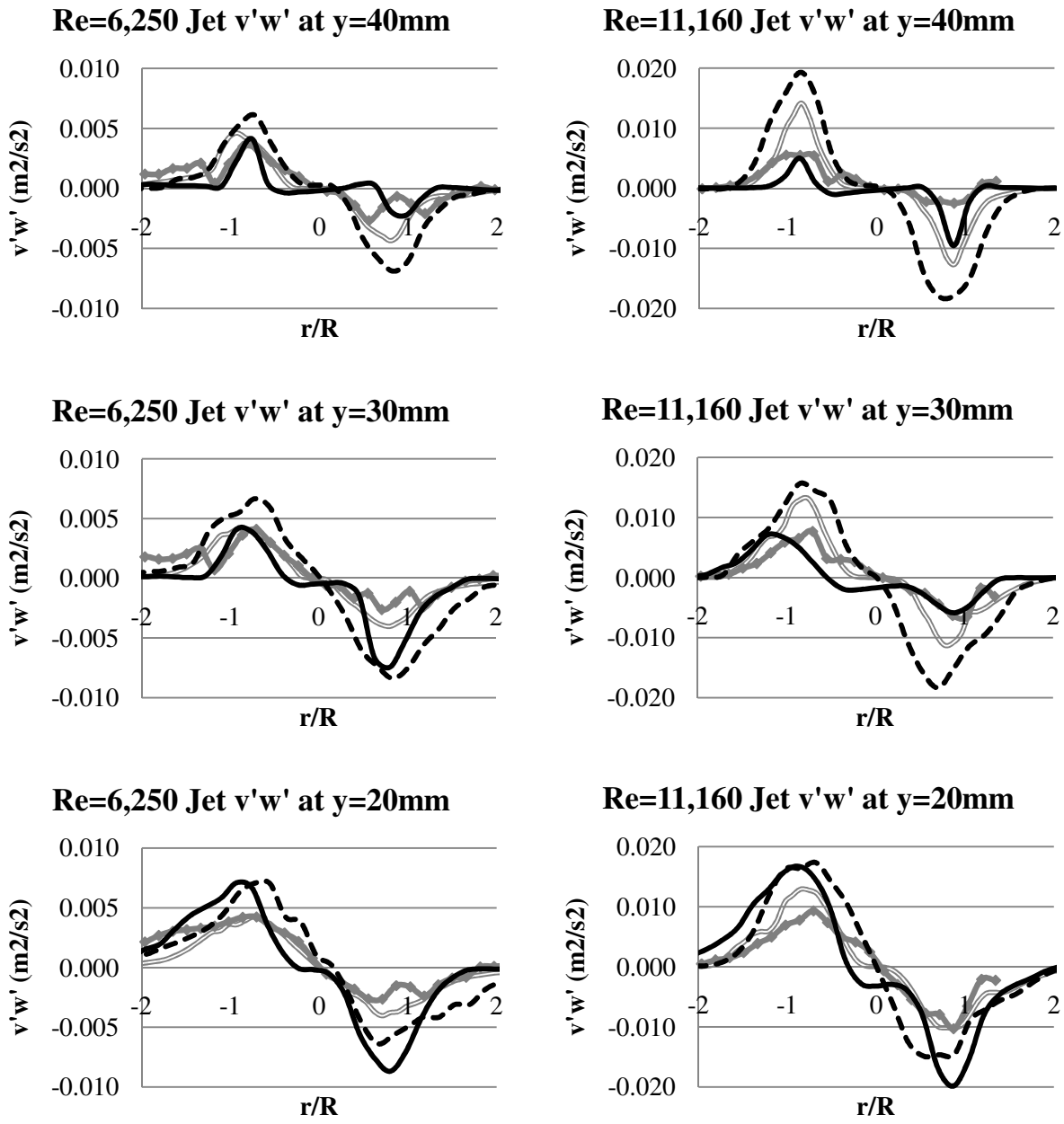

Figure 84 Reynolds stress components across jet plumes at various heights. Experiment, RSM w/ hex mesh, LES w/ poly mesh, ---LES w/ hex mesh

The LES results follow the same decay trend over the inertial range, but the polyhedral grid using the SOU approach drops off at lower frequencies than the fully hexahedral grid. For all measured points within the jet plume, the fully hexahedral grid using the central-differencing scheme resolved more turbulence scales in the inertial range than the polyhedral grid using the SOU approach. This result coincides with the previous observations indicating higher amounts of resolved turbulence with the central-differencing approach with the fully hexahedral grid. In the case of points one and two that neighbor the central rod (indicated in figure 76), the flow feature at these points is a mostly stable vortex that is generated as the impinging jet flow spreads out and then strikes the central rod, redirecting the flow upward forming a large vortex that wraps partway around due to the bulk flow in the region around the rod. The PSD of the signals at the points adjacent to the rod (figure 86) indicate steeper decays in the inertial range than that of the Kolmogorov -5/3 decay of turbulence. It is possible that this is due to intermittency in these locations as vortices at larger scales are generated in the jet plume that then propagate through the impingement layer and into these regions. The experimental PSD in this region has a slope nearly matching that of the numerical results, but at higher frequencies it has little or no slope. This is a consequence of the measurement technique in flows of this type where high gradients in the flow are present and good statistical measurement of both high and low velocity regions becomes extremely difficult. For this reason, the flattened region is disregarded for comparison.

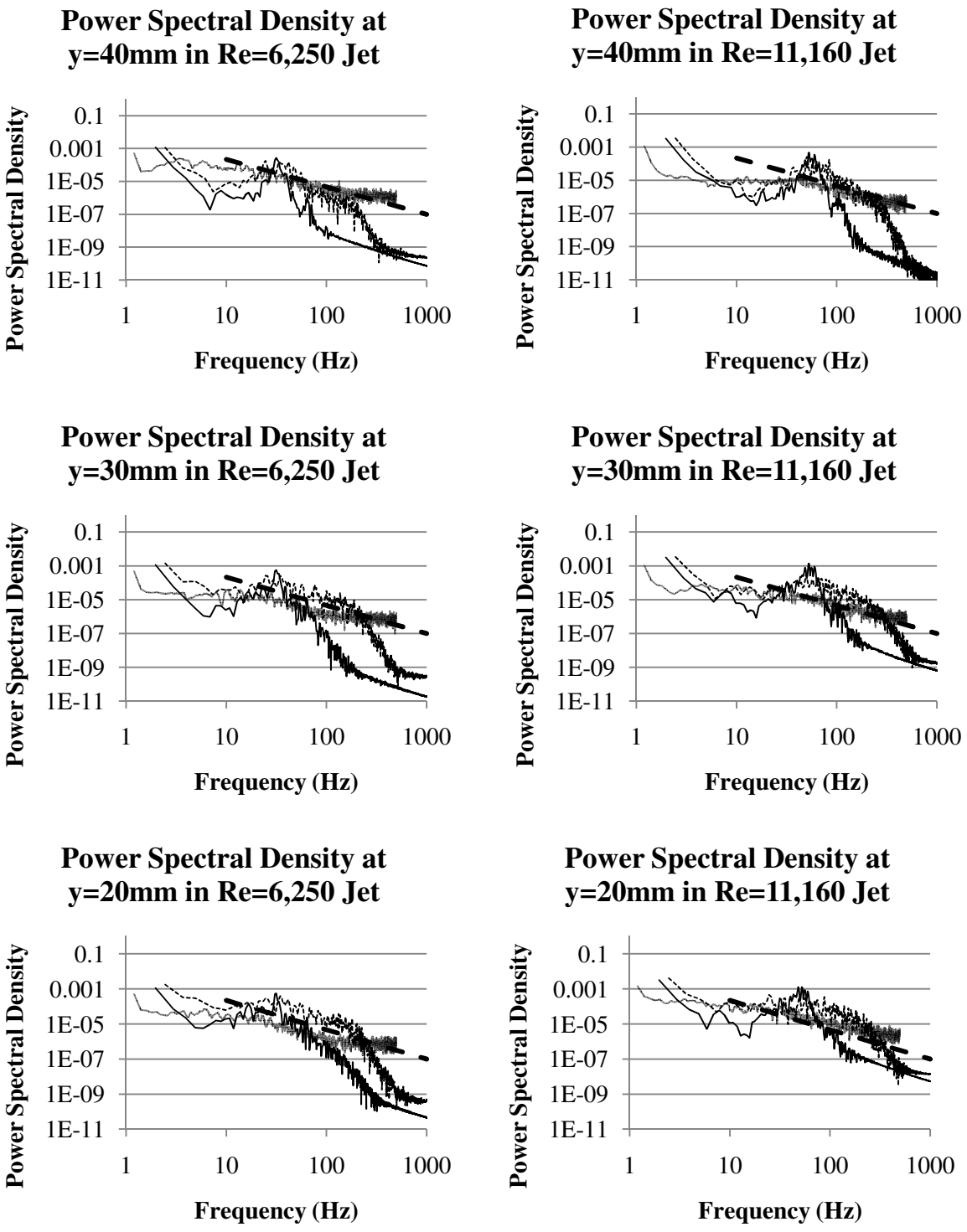

Figure 85 Power spectral densities comparisons at various heights within the jet axis. — Experiment, ▬ LES w/ poly mesh, --- LES w/ hex mesh, – – Kolmogorov's -5/3 Decay

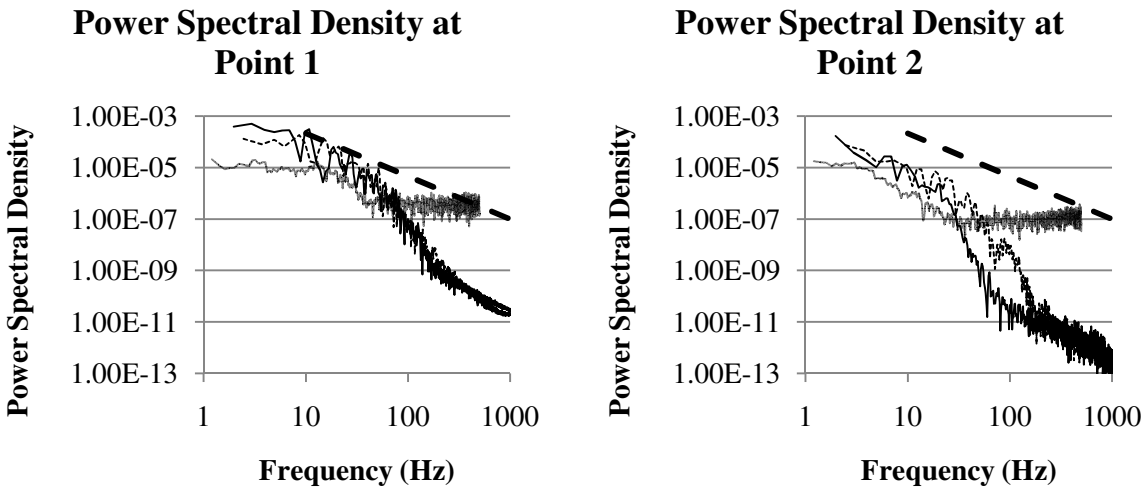

Figure 86 Power spectral densities in locations near center rod recirculation zones. — Experiment, ▬ LES w/ poly mesh, --- LES w/ hex mesh, – – Kolmogorov's -5/3 Decay

Observing CFD results between the two numerical schemes and the experimental data using the proposed spatio-temporal wavelet decomposition yields a telling visualization of resolved scales within the jet plumes. The instantaneous and average correlation coefficients with the method are presented in figure 87 and figure 88 for three different frequencies within each jet plume. It should be noted that due to the limited region of the PIV images, the right-hand side of the Re=11,160 jet is cut off and results rather poor statistics right along the image edge (refer to figure 80 for data acquisition region). The case of the Re=6,250 jet was not cut within the jet plume and does not suffer from the same experimental deficiency.

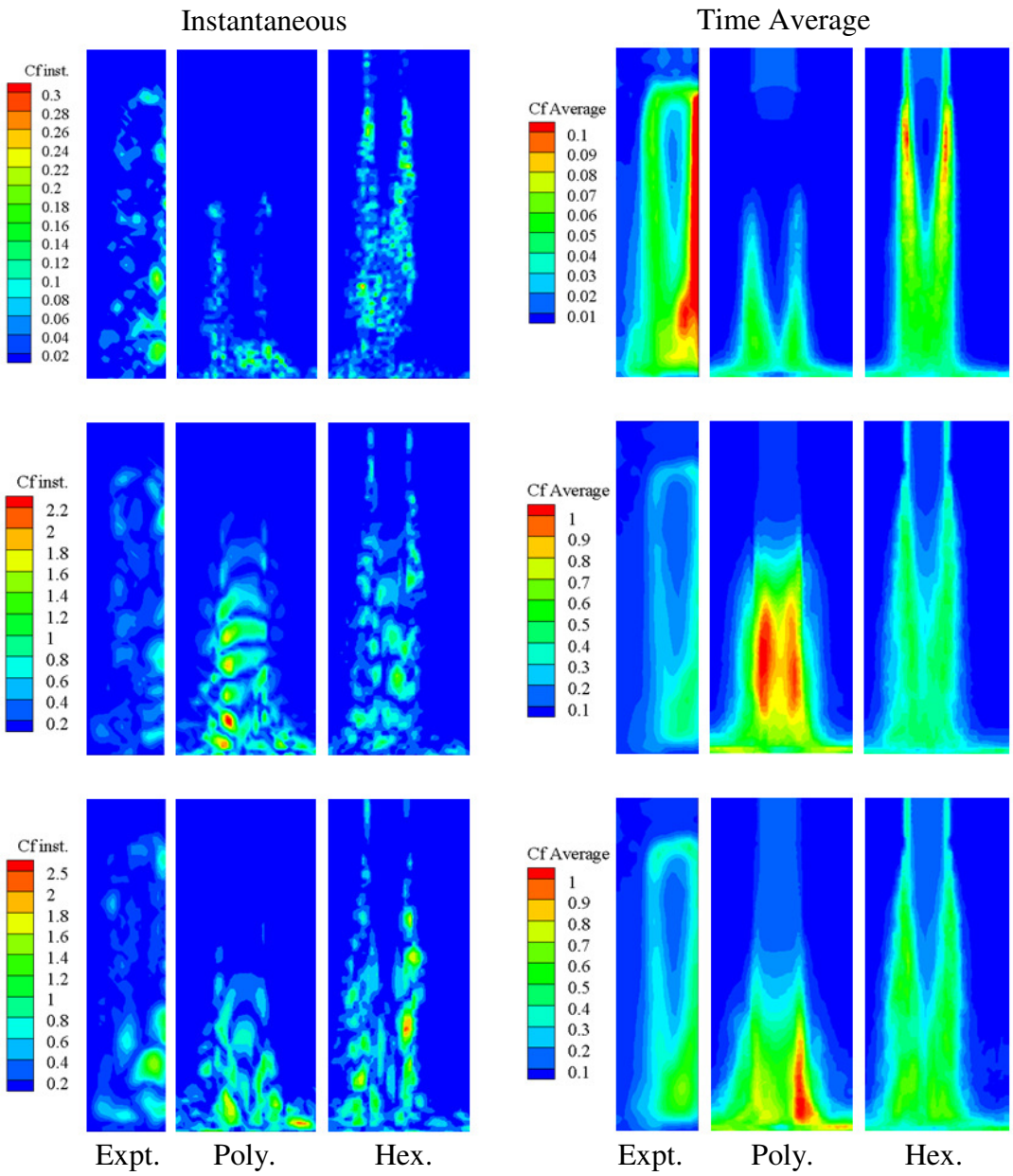

Figure 87 Instantaneous(left) and average(right) wavelet coefficient plots experimental, polyhedral grid, and hexahedral grids at 270.8 Hz(top), 49.2 Hz(middle), 30.7 Hz(bottom) for of the Re=11,160 jet

The power spectral density taken at various heights indicate that the power contained at a frequency scale of 270.8 Hz are better resolved by the hexahedral grid with a central differencing scheme than by the polyhedral grid with the SOU approach. Instantaneous and average spatio-temporal wavelet decompositions of the Re=11,160 jet in figure 87 show that the polyhedral grid failed to capture fluctuations at this frequency within and just outside the jet, despite a wall resolved grid according to the wall y+ criterion discussed in the discretization section. The fully hexahedral grid did capture these scales within the inlet nozzle and into the entry region of the fluid domain. The failure to capture these scales of turbulence by the polyhedral grid extends several diameters into the region and highlights the importance of properly conditioned inlet conditions. In the case of both grids, an inlet length of 10D was used to endure proper development of turbulent structures; however, the polyhedral grid suffered from artificial destruction of turbulence on these scales. The presence of these scales (along the left hand edge) in the experimental plume is observed to be present from the nozzle to the impingement plane and is in good agreement with the hexahedral grid results for both instantaneous and average decompositions. Between the two mesh types in the case of the Re=6,250 jet at 270.8 Hz (figure 88), the hexahedral grid resulted in better agreement with experimental data; however, the average correlation coefficient of the CFD result was under-predicted.

At lower frequencies (49.2 Hz and 30.7 Hz) in both Reynolds number jets, the polyhedral grid produced more coherent frequency structures that resulted in higher magnitude correlation coefficients than in the hexahedral grid case. It is possible that the

coherence of these structures comes as a result of limited breakdown into smaller scales by the numerical scheme causing scales to remain large. The resulting signals at each point are highly periodic at the larger scales and provide a signal with which the Morlet wavelet basis function may closely correlate. The instantaneous structures at the lower frequencies, as well as the magnitude of the average correlation coefficient of the hexahedral grid result are more representative of the experimental data.

3.3.5 Conclusions on Numerical Scheme Selection

The large eddy simulation results obtained using a refined polyhedral grid with a second order upwinding scheme for the convection term results in an artificial dissipation of turbulent kinetic energy and overall poor performance at resolving small scales of turbulence. This deficiency was illustrated qualitatively with instantaneous snapshots of the flow structure and quantitatively through the use of a jet plume spreading rate study, a power spectral density study, and a novel spatio-temporal wavelet decomposition approach. In each of these studies, the fully hexahedral grid using a pure central differencing scheme performed better than the second order upwinding scheme and is therefore recommended as the preferred grid in simulations of the lower plenum of the GT-MHR.

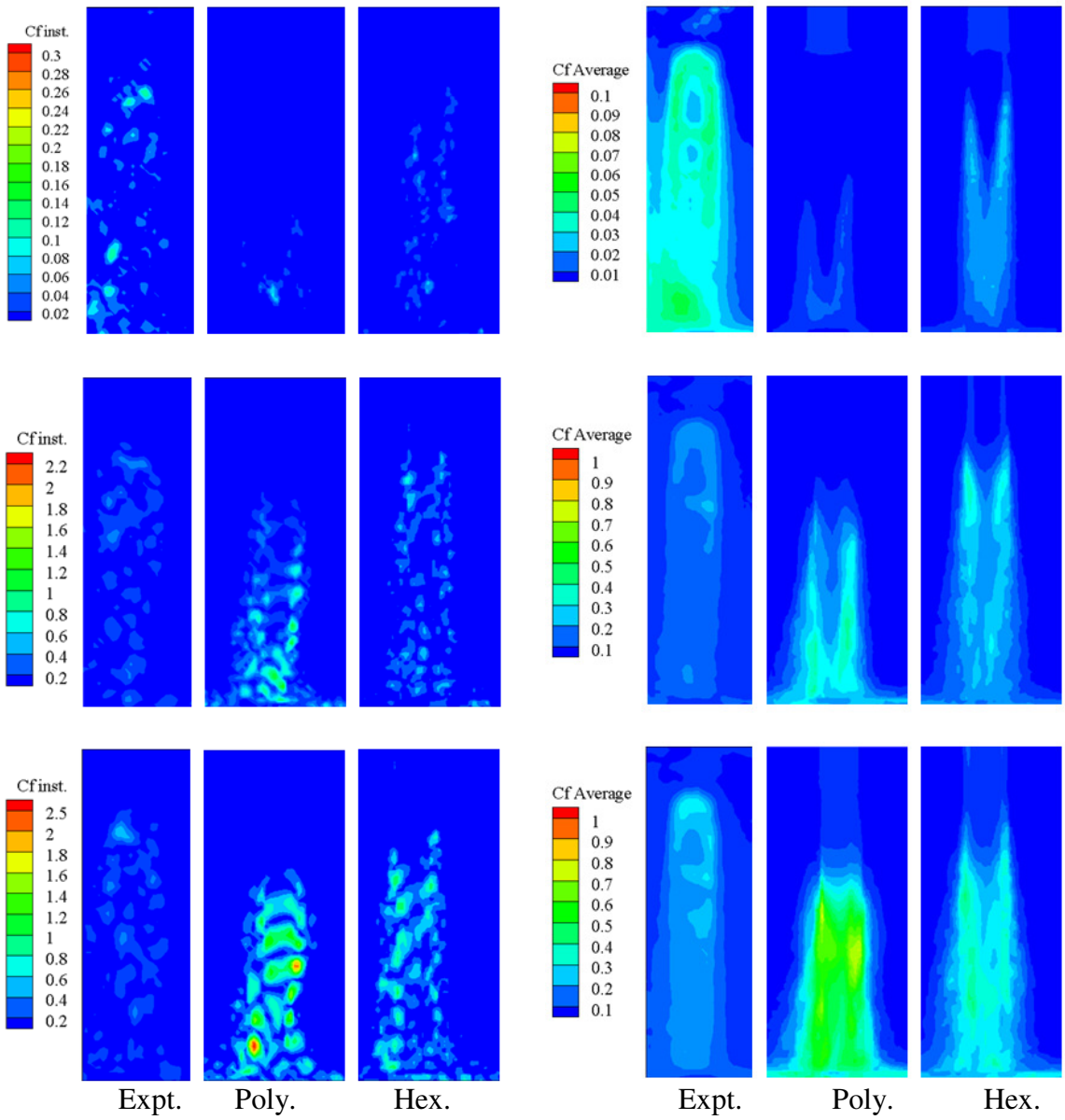

Figure 88 Instantaneous(left) and average(right) wavelet coefficient plots for experimental, polyhedral grid, and hexahedral grids at 270.8 Hz(top), 49.2 Hz(middle), 30.7 Hz(bottom) for of the Re=6,250 jet

4. CONCLUSIONS

Through the use of synthetic data, experimental data, and numerical results, the spatio-temporal 1D wavelet decomposition method developed was shown to be a practical tool for design engineers and research scientists alike to observe coherent flow structures in a variety of formats. The results of the verification study illustrated that very clear signal identification is possible with very low levels of noise in the signal from other frequencies under ideal conditions. The experimental PTV data of the side entry orifice of the GE BWR-6 could not serve as an appropriate set due to the straddling technique providing a discontinuous signal that could not utilize the developed spatio-temporal wavelet method. Although the method could not be tested, the acquired pressure data across the side entry orifice did provide a good test for the 1D wavelet semblance method. The results of this test showed strong correlation across the orifice among low global frequencies in the 2-3 Hz range, and some degree of phase shift in the higher frequencies between 5 Hz and 60 Hz. Through the study, limitation of this method becomes apparent by the lack of spatial knowledge.

The success of the method in extracting large coherent structures from the raw video data of the air ingress scenario of the GT-MHR illustrated the engineering applicability of such a tool for design engineers. Looking forward (pending advances in computing power) it may be possible to foresee handheld devices with the ability to display ‘near’ real-time frequency visualization for diagnostics in a wide range of fields.

The use of the decomposition method in the case of the CFD simulations for

improving current best practices in simulating flows within the lower plenum of the Gas Turbine - Modular Helium Reactor illustrated the applicability of the method. In addition to the conclusion that the use of a polyhedral grid is not appropriate for use with LES for studies in the lower plenum of the GT-MHR, this work introduces, verifies, and demonstrates the applicability of a new visualization technique that is believed to have significant engineering potential that extends beyond use in experimental and computational fluid dynamics.

REFERENCES

[1] Da Vinci, L., 1970, *The Notebooks of Leonardo Da Vinci*, Dover Publications, New York.

[2] Fourier, J. B. J. B., 1822, *Theorie Analytique De La Chaleur*, Paris F. Didot, Paris, France.

[3] Kosambi, D. D., 1943, "Statistics in Function Space," Journal of Indian Mathematics Society, 7(1), pp. 76-88.

[4] Haar, A., 1910, "Zur Theorie Der Orthogonalen Funktionensysteme," Mathematische Annalen, 69(3), pp. 331-371.

[5] Mallat, S. G., 1989, "A Theory for Multiresolution Signal Decomposition: The Wavelet Representation," Pattern Analysis and Machine Intelligence, IEEE Transactions on, 11(7), pp. 674-693.

[6] Johnson, C., Webb, S., Cooper, G., and Frescura, F., 2009, "Wavelet-Based Semblance Analysis Applied to Geophysical Borehole Data," Proceedings of 11th SAGA Biennial Technical Meeting and Exhibition, Swaziland,

[7] Stollnitz, E. J., Derose, T. D., and Salesin, D. H., 1996, *Wavelets for Computer Graphics : Theory and Applications*, Morgan Kaufmann Publishers, San Francisco.

[8] Nahas, A., Calvo, A., and Piva, M., 2010, "Swirling Flow in a Fixed Container: Generation and Attenuation of a Vortex Column," Journal of Fluids Engineering, 132(11), pp. 111204-9.

[9] Watanabe, S., Abe, Y., Kaneko, A., Watanabe, F., and Tezuka, K., 2010, "Study on Pressure Loss Induced by Complicated Flow through Lower Plenum of Bwr," ASME Conference Proceedings, 2010(49323), pp. 569-577.

[10] Yan, J., and Mallner, A., 2009, "Sensitivity Study of Lower Plenum Boron Injection in a Bwr," ASME Conference Proceedings, 2009(43550), pp. 239-247.

[11] Al'tshul, A., and Margolin, M., 1968, "Effect of Vortices on the Discharge Coefficient for Flow of a Liquid through an Orifice," Power Technology and Engineering (formerly Hydrotechnical Construction), 2(6), pp. 507-510.

[12] 2002, *Fuel Support Side Entry Orifice Loss Coefficient in Core Monitoring System Databank*, U.S. Nuclear Regulatory Commission Operations Center,Event Report 02-08NRC.DOC, MFN 02-067, Event No. 39247,

[13] Movafaghian, S., Jaua-Marturet, J. A., Mohan, R. S., Shoham, O., and Kouba, G. E., 2000, "The Effects of Geometry, Fluid Properties and Pressure on the Hydrodynamics of Gas–Liquid Cylindrical Cyclone Separators," International Journal of Multiphase Flow, 26(6), pp. 999-1018.

[14] Estrada-Perez, C. E., and Hassan, Y. A., 2010, "Ptv Experiments of Subcooled Boiling Flow through a Vertical Rectangular Channel," International Journal of Multiphase Flow, 36(9), pp. 691-706.

[15] Kubin, R. F., and Fletcher, A. N., 1983, "Fluorescence Quantum Yields of Some Rhodamine Dyes," Journal of Luminescence, 27(4), pp. 455-462.

[16] Bunnell, L. R., Campbell, T. K., and Tingey, G. L., 1987, *Oxidation of Tsx Graphite over the Temperature Range 450 to 1200c*, PNL,UNI-SA-207, Richland, WA.

[17] Oh, C., Davis, C., Siefken, L., Moore, R., No, H. C., Kim, J., Park, G. C., Lee, J. C., and Martin, W. R., 2006, *Development of Safety Analysis Codes and Experimental Validation for a Very High Temperature Gas-Cooled Reactor Final Report*, Idaho National Laboratory,INL/EXT-06-01362,

[18] Oh, C., Kim, E. S., Schultz, R., Petti, D., and Liou, C. P., 2008, "Implications of Air Ingress Induced by Density-Difference Driven Stratified Flow," Proceedings of ICAPP, Paper 8023, Anaheim, CA, Paper 8023

[19] Gröbelbauer, H. P., Fanneløp, T. K., and Britter, R. E., 1993, "The Propagation of Intrusion Fronts of High Density Ratios," Journal of Fluid Mechanics, 250(pp. 669-687.

[20] Peterson, H., 1970, *The Properties of Helium: Density, Specific Heats, Viscosity, and Thermal Conductivity at Pressures from 1 to 100 Bar and from Room Temperature to About 1800k*, Danish Atomic Energy Commission,Risö Report No. 224,

[21] Hartley, J., 2011, "Double Ended Guillotine Break in a Prismatic Block Vhtr Lower Plenum Air Ingress Scenario," Texas A&M University M.S. Thesis, pp. 1-55.

[22] Amini, N., and Hassan, Y. A., 2009, "Measurements of Jet Flows Impinging into a Channel Containing a Rod Bundle Using Dynamic Piv," International Journal of Heat and Mass Transfer, 52(23–24), pp. 5479-5495.

[23] Shu, F., Plesniak, M. W., and Sojka, P. E., 2005, "Indeterminate-Origin Nozzles to Control Jet Structure and Evolution," Journal of Turbulence, 6(26), pp. 1-18.

[24] Cooper, D., Jackson, D. C., Launder, B. E., and Liao, G. X., 1993, "Impinging Jet Studies for Turbulence Model Assessment—I. Flow-Field Experiments," International Journal of Heat and Mass Transfer, 36(10), pp. 2675-2684.

[25] Craft, T. J., Graham, L. J. W., and Launder, B. E., 1993, "Impinging Jet Studies for Turbulence Model Assessment—Ii. An Examination of the Performance of Four Turbulence Models," International Journal of Heat and Mass Transfer, 36(10), pp. 2685-2697.

[26] Abdel-Fattah, A., 2007, "Numerical and Experimental Study of Turbulent Impinging Twin-Jet Flow," Experimental Thermal and Fluid Science, 31(8), pp. 1061-1072.

[27] Angioletti, M., Nino, E., and Ruocco, G., 2005, "Cfd Turbulent Modelling of Jet Impingement and Its Validation by Particle Image Velocimetry and Mass Transfer Measurements," International Journal of Thermal Sciences, 44(4), pp. 349-356.

[28] Sengupta, A., and Sarkar, P. P., 2008, "Experimental Measurement and Numerical Simulation of an Impinging Jet with Application to Thunderstorm Microburst Winds," Journal of Wind Engineering and Industrial Aerodynamics, 96(3), pp. 345-365.

[29] Salpeter, N., and Hassan, Y., 2011, "Large Eddy Simulations of Jet Flow Interaction within Staggered Rod Bundles," Nuclear Engineering and Design, pp. 1-10.

[30] Nicoud, F., and Ducros, F., 1999, "Subgrid-Scale Stress Modelling Based on the Square of the Velocity Gradient Tensor," Flow, Turbulence and Combustion, 62(3), pp. 183-200.

[31] Celik, I. B., Ghia, U., Roache, P. J., Freitas, C. J., Coleman, H., and Raad, P. E., 2008, "Procedure for Estimation and Reporting of Uncertainty Due to Discretization in Cfd Applications," Journal of Fluids Engineering, 130(7), pp. 078001-4.

[32] Kolmogorov, A. N., 1991, "Dissipation of Energy in the Locally Isotropic Turbulence," Proceedings: Mathematical and Physical Sciences, 434(1890), pp. 15-17.

APPENDIX A

%%Spatio-Temporal 1D Wavelet Decomposition Method Subroutine

%%Software Platform: Matlab r2010b

```
%%%
```

```
%% otherwise interactive mode with all processors
will %%remain open, burning %% your cpu hours!!
```

%% Set measurement frequency, Fs. Length and time labels are calculated

```
Fs=100;
```

%% a) Decide what range of scales (frequencies) you want to decompose by
%%copying and pasting the following code into the interactive window and running.
%%You may change the maxscale (lowest frequency), and the wavelet basis function,
%%wname.

```
maxscale=256;
scales = (1:maxscale);
wname='morl';
for n=1:maxscale
freqlabel(n)=scal2frq(n,wname,1/Fs);
end
```

%% View output freqscale for frequencies for each scale integer

%% 1) Build Data Matrix

%% a) Initialize data matrix and start Loop

```
original=[];
for n=1:9;
```

%% a) Specify filename with counter

```
FileName=sprintf('allfansbl000%d.bmp',n);
```

%% hint: pay attention to how you index your files. If they have 0s
%%preceding them for the lower count files, you may have to implement
%%several loops with different file names with different numbers of 0s. If
%%there are no preceding 0s, then a single loop will suffice.

%% b) Import file

```
test0=importdata(FileName);
```

%% c) Prepare data (make grayscale, or double precision if needed)

```
%%%%%%%     For Image:
                test1=rgb2gray(test0);
```

%% d) (Experimental/CFD) Extract column and concatenate to data matrix

```
original=cat(2,original,test0(:,1));
%%(where *1* is the column of the data you want, but
no %%asterisks)
```

%%%% (Image) Reshape image matrix into a single column and concatenate to %%matrix

```
[l,m]=size(test1);
resh=reshape(test1(:,:),l*m,1);
original=cat(2,original,resh);
```

%% e) Clear temporary arrays

```
test1=[];
test0=[];
resh=[];
%% (only for image cases, but you may leave resh)
```

%% f) Loop back to (a) for as many time-steps as desired

```
end
```

%% 2i) For Coefficient Sp-Temp Wavelet.

%% b) Measure data matrix and set time strings

```
[p,q]=size(original);

start=1;
finish=q;
tl=(finish-start)/Fs;
T=0:1/Fs:tl;
```

%% c) Prepare data matrix if needed (normalize etc)

```
original3=[];
if parallel==0
```

```
                for i=1:p;
                 original3(i,:)=original(i,:)-mean(original(i,:),2);
                end
                end

                if parallel==1
                parfor i=1:p;  %replace for with this for parallel
                 original3(i,:)=original(i,:)-mean(original(i,:),2);
                end
                end
```

```
%%  d)  Set fieldrs variable to data matrix (normalized or non) and
%%clear temp matrices

        fieldrs=double(original3);
            original=[];


                Original3=[];

                for i=1:p;
                %     parfor i=1:p;  %replace for with this for
            parallel
                      original3(i,:)=original(i,:)-
                mean(original(i,:),2);
                end
```

%% d) Set fieldrs variable to data matrix (normalized or non) and clear temp %%matrices

```
                fieldrs=double(original3);
                original=[];
```

%%%%% Compute Wavelet coefficient sum matrix

%% fa) Obtain Coefficient Sum Matrix by running wavelet2Daverage.m %%subroutine

```
                if programtype==0
                for i=1:p
                      % parfor i=1:h   %% for parallel

      [coefsum]=wavelet2Daverage(fieldrs(i,:),wname,scales,Fs);
```

%% ga) Assign coefficients at scale index i to DAWavelet column I and clear %%coefsum.

```
DAWavelet(i,:)=coefsum;
coefsum=[];
```

%% ha) Loop back to (f) for the total number of points (rows) in the fieldrs

```
end
end
```

%%%%% Compute Wavelet coefficient instantaneous matrix

%% fi) Obtain Coefficient Sum Matrix by running wavelet2Dinstant.m %%subroutine

```
if programtype==1

    maxscale=6;
    scales1 = (maxscale:maxscale);
for i=1:p
    % parfor i=1:h   %% for parallel

[coefsum]=wavelet2Dinstant(fieldrs(i,:),wname,scales1,Fs);
```

%% gi) Assign coefficients at scale index i to DAWavelet column I and clear %%coefsum.

```
DAWavelet(i,:)=coefsum;
coefsum=[];
```

%% hi) Loop back to (f) for the total number of points (rows) in the fieldrs

```
end
end
```

%% i1) For **experimental/CFD data**, read location columns and write each file %%for each scale column in the DAWavelet Matrix.

```
if datatype==0
```

%%%%% Output Wavelet coefficient sum matrix

```
if programtype==0
    test0=importdata(FileName);
    positions(i,1)=test0(:,1);
```

```
            positions(i,2)=test0(:,2);
            positions(i,3)=test0(:,3);
            %%replace 1, 2, and 3 with x, y, and z %%column
            %%numbers
                for u=1:g
                    tempW(:,1)=positions(:,1);
                    tempW(:,2)=positions(:,2);
                    tempW(:,3)=positions(:,3);
                    tempW(:,4)=DAWavelet(:,u);
            name2=sprintf('expt-output-at-scale-%d.csv',u);
                    dlmwrite(name2, tempW);
                end
        end
```

%%%%% Output Wavelet coefficient instantaneous matrix

```
        if programtype==1

headers={'Velocity Magnitude (m/s)','U Velocity (m/s)','V Velocity
(m/s)','W Velocity (m/s)','Scale 6','X(m)','Y(m)','Z(m)'};
```

%% In my case, I constructed a data matrix for each velocity %%component, as well as an array for the positions.

```
        %% built the same as 'original'
        FileName=sprintf('velmag.mat');
        velmag=importdata(FileName);

        %% built the same as 'original'
        FileName=sprintf('ivelcomp.mat');
        ivel=importdata(FileName);

        %% built the same as 'original'
        FileName=sprintf('jvelcomp.mat');
        jvel=importdata(FileName);

        %% built the same as 'original'
        FileName=sprintf('kvelcomp.mat');
        kvel=importdata(FileName);

        %% built from just one file (1 column)
        FileName=sprintf('xpos.mat');
        xpos=importdata(FileName);

        %% built from just one file (1 column)
        FileName=sprintf('ypos.mat');
        ypos=importdata(FileName);
```

```
            %% built from just one file (1 column)
            FileName=sprintf('zpos.mat');
            zpos=importdata(FileName);



            for u=start:finish
               output(:,1)=velmag(:,u);
               output(:,2)=ivel(:,u);
               output(:,3)=jvel(:,u);
               output(:,4)=kvel(:,u);
               output(:,5)=DAWavelet1(:,u);

            %%  Add extra outputs here if desired, and adjust
            indexes %and headers.
               output(:,6)=xpos(:,1);
               output(:,7)=ypos(:,1);
               output(:,8)=zpos(:,1);
                    name2=sprintf('velmag_hex_instant-%d.csv',u);
                    csvwrite_with_headers(name2,output,headers);

                    finalfile=[];
             end
            end


            if parallel==1
                  matlabpool close
            end

        end
```

%% i2) For **image data**, read location columns

```
        if datatype==1
```

%% You may normalize each pixel to the highest measured scale if you prefer as
%% done below with the maximum coefsum at each pixel. This should be done
%% only if parallelized as it is expensive!!

```
            if programtype==0

              if parallel==1
                  Coefmax=max(DAWavelet,[],2);
                  parfor i=1:69280
```

```
            DAWavelet2(i,:)=original(i,:)/originalm
            ax(i,1);
            end
        end



        for u=1:g

            tempW=reshape(DAWavelet2(:,u),l,m);
            name2=sprintf('img-output-at-scale-%d.bmp',u);
            imwrite(tempW,name2,'bmp');
        end
    end


    if programtype==1

        for u=1:g

        DAWavelet12(:,u)=DAWavelet1(:,u)/max(maximum(:,1)
        );
            tempW=reshape(DAWavelet12(:,u),l,m);
            name2=sprintf('img-output-scale6-inst-
        %d.bmp',u);
            imwrite(tempW,name2,'bmp');
        end

    end

    if parallel==1
          matlabpool close
    end

end
```

%% wavelet2Daverage.m Put into its own .m file within the same folder

```
function [ coefsum ] = wavelet2Daverage(signal,wname,scales,Fs)

coefs= cwt(signal,scales,wname);
[n,m]=size(coefs);
coefsum(n,1)=0;

for i=1:n
    for j=1:m
coefsum(i,1)=coefsum(i,1)+abs(coefs(i,j));
    end
end

coefsum=transpose(coefsum);

end
```

%% wavelet2Dinstant.m Put into its own .m file within the same folder

```
function [ coefsum ] = wavelet2Dinstant(signal,wname,scales,Fs)

coefs= cwt(signal,scales,wname);
[n,m]=size(coefs);
coefsum(n,m)=0;

coefsum(1,:)=abs(coefs(1,:));

coefsum=transpose(coefsum);

end
```

APPENDIX B

Data type: Raw Pressure Voltage Data
Cases: Test Data Sets 1 and 2 (tables 2 and 3)
Filename: Raw Pressure Data.xlsx

Table format:

91 GPM Re = 138,139				
NI VI Logger				
Created: 10/27/2010 6:13:56.374 PM Central Daylight Time				
Number of scans: 500000				
Scan rate: 0.001 seconds (1kHz)				
		Before SEO	**After SEO**	**At Pump**
Row	**Time**	**Ptrans_00_03 before(Voltage)**	**Ptrans_04 after(Voltage)**	**Ptrans_01 pump(Voltage)**
1	57:58.7	0.00303	0.00152488	0.0037341
…	…	…	…	…

Data Type: 2D PTV Instantaneous Data

The instantaneous particle data is stored in several different files for each time step. Listed below are the main files and appropriate units

Raw Video Files (*.cine)

Filtered vectors (*.fil) in pixels/time-step

Unfiltered vectors (*.dat) in pixels/time-step

Fluctuating Components (*.fluc) in pixels/time-step

Average Velocity Field (*.favg) in pixels/time-step

Data type: Planar velocity data (m/s)
Cases: Re=1.5E5 and Re=1.83E5
Filename: t9_t8_planes.output.xlsx

Table format:

Test # - <flow rate> - Re=<>							
X (m)	Y (m)	Z(m)	U (m/s)	V (m/s)	Velocity Magnitude (m/s)	Z Vorticity	# of vectors
-1.64E-04	3.09E-02	4.83E-03	-3.15E-01	1.71E-01	3.58E-01	-2.88E+02	2.82E+03
…	…	…	…	…	…	…	…

Where the number of vectors indicated in the far right column is the total number of instantaneous vectors averaged at the particular (x,y,z) to obtain the final velocity vector at that point.

Data type: Line probe velocity data (m/s)
Cases: Re=1.5E5 and Re=1.83E5
Filename: t9_t8_lines-output.xlsx

Table format:

Test # - <flow rate> - Re=<>						
X (m)	Y (m)	Z(m)	U (m/s)	V (m/s)	Velocity Magnitude (m/s)	Z Vorticity
1.63E-03	1.41E-01	4.83E-03	1.02E-02	8.04E-01	8.04E-01	6.54E+00
…	…	…	…	…	…	…

VITA

Name:	Nathaniel O. Salpeter
Address:	Texas A&M University Department of Mechanical Engineering 3123 TAMU College Station TX 77843-3123
Email Address:	nsalpeter@gmail.com
Education:	B.S., Mechanical Engineering, University of Florida, 2007 M.S., Mechanical Engineering, Texas A&M University, 2010 Ph.D., Mechanical Engineering, Texas A&M University, 2012